

UNIVERSITY OF CALIFORNIA, SAN DIEGO

Ab initio study of structure and dynamics of bulk, surface  
and the mineral/aqueous fluid interface regions

A dissertation submitted in partial satisfaction of the  
requirements for the degree Doctor of Philosophy

in

Chemistry with specialization in Computational Science

by

Ying Chen

Committee in charge:

Professor John Weare, Chair  
Professor Michael Galperin  
Professor Michael Holst  
Professor Clifford Kubiak  
Professor J. Andrew McCammon

2015

UMI Number: 3688073

All rights reserved

INFORMATION TO ALL USERS

The quality of this reproduction is dependent upon the quality of the copy submitted.

In the unlikely event that the author did not send a complete manuscript and there are missing pages, these will be noted. Also, if material had to be removed, a note will indicate the deletion.



UMI 3688073

Published by ProQuest LLC (2015). Copyright in the Dissertation held by the Author.

Microform Edition © ProQuest LLC.

All rights reserved. This work is protected against unauthorized copying under Title 17, United States Code



ProQuest LLC.  
789 East Eisenhower Parkway  
P.O. Box 1346  
Ann Arbor, MI 48106 - 1346

Copyright

Ying Chen, 2015

All rights reserved

The Dissertation of Ying Chen is approved, and it is acceptable in quality and form for publication on microfilm and electronically:

---

---

---

---

---

Chair

University of California, San Diego

2015

## TABLE OF CONTENTS

SIGNATURE PAGE.....	iii
TABLE OF CONTENTS.....	iv
LIST OF FIGURES.....	vi
LIST OF TABLES.....	ix
ACKNOWLEDGEMENTS.....	x
VITA.....	xii
ABSTRACT OF THE DISSERTATION.....	xiii
 1 INTRODUCTION TO MINERAL SURFACE AND MINERAL FLUID INTERFACE.....	 1
1.1 Progress of Mineral surface and fluid interface studies.....	1
1.2 Overview and Objectives.....	2
 2 FIRST PRINCIPLE METHODS AND ITS APPLICATION.....	 5
2.1 Modeling complexity of Mineral surface and Interface with fluid.....	5
2.2 Introduction of First Principles method.....	5
2.2.1 Introduction to Kohn-Sham equation.....	6
2.2.2 Introduction to Ab-initio Molecular Dynamics.....	7
2.3 Choices affect the accuracy and efficiency of the calculation.....	7
2.3.1 Simulation size and plane-wave basis.....	8
2.3.2 Exchange-correlation potential and pseudopotentials.....	9
 3 ACCURACY OF CALCULATIONS OF OBSERVABLE BULK PROPERTIES...13	
3.1 Bulk Structural Properties.....	13
3.1.1 Structural properties of corundum.....	13
3.1.2 Structural properties of hematite and goethite.....	14
3.2 Bulk electronic structural properties.....	16
3.2.1 Band gaps.....	16
3.2.2 Spin configuration in hematite and goethite.....	17
3.2.3 Projected density of states.....	19
 4 STUDY OF GOETHITE (100) SURFACE AND AQUEOUS INTERFACE.....	 27
4.1 Introduction.....	27
4.2 Details of computational methods.....	29
4.3 Goethite (100) surface.....	30
4.3.1 Surface termination.....	30
4.3.2 One water molecule absorbed on surface.....	31
4.3.3 Two water molecules absorbed on surface.....	33
4.4 Goethite (100) – water interface.....	33

4.4.1	Bonds in interface.....	34
4.4.2	Three types of water molecules.....	36
4.4.3	Dynamical process on the interface.....	39
4.5	Conclusion.....	41
5	STUDY OF HEMATITE (001) AND (012) SURFACES, AQUEOUS INTERFACES AND FE(II) ION ABSORPTION IN INTERFACS.....	51
5.1	Introduction.....	51
5.2	Computational methods and computational cells.....	53
5.2.1	Computational methods.....	53
5.2.2	Computational cells structural details.....	55
5.2.3	Spin configurations of surface slabs.....	56
5.3	The (012) protonation and water absorption of cleaved Surfaces.....	56
5.3.1	Hematite (012) surface protonation models.....	56
5.3.2	Water absorption on hematite (012) cleaved surface.....	57
5.4	Structural properties of interface.....	59
5.4.1	Hematite (001) aqueous interface.....	59
5.4.2	Hematite (012) aqueous interface.....	61
5.4.3	Fe(II) absorption on hematite (001) aqueous interface.....	63
5.4.4	Fe(II) absorption on hematite (012) aqueous interface.....	64
5.5	Electronic structural properties of ion absorption in interface.....	65
5.5.1	Projected density of states analysis.....	65
5.5.2	The mechanism of electron transfer.....	66
6	STUDY OF CORUNDUM (001) SURFACE AND AQUEOUS INTERFACE...79	
6.1	Introduction.....	79
6.2	Computational methods.....	81
6.3	Structure and electronic structure of corundum (001) surface.....	82
6.3.1	Surface relaxations of corundum (001).....	82
6.3.2	PDOS for Al-terminated corundum (001) surface.....	83
6.4	Comparison of AIMD and experiments by electron density profiles.....	83
6.5	Direct comparison of AIMD with experiments.....	84
7	SUMMARY AND FUTURE WORK.....	91
7.1	Summary.....	91
7.2	Future works.....	92
7.2.1	Sampling method in interface simulation.....	92
7.2.2	QM/MM method in interface simulation.....	93
7.2.3	DMFT.....	94
	Appendix.....	95
	References.....	102

## LIST OF FIGURES

Figure 3.1: Cells for bulk Goethite, Hematite and Corundum.....	25
Figure 3.2: Projected Density of state near Fermi level for bulk hematite using different methods.....	26
Figure 4.1: Bulk structure and two types of (100) surface terminations of goethite.....	44
Figure 4.2: Site choices of one water molecule adsorption on goethite (100) surface.....	44
Figure 4.3: Two side-views of different types of H-bonds and water molecules goethite (100) aqueous interface.....	45
Figure 4.4: Surface bonds and Hydrogen bonds of two additional water layers absorbed on goethite (100) surface.....	46
Figure 4.5: Radial distribution function of Fe-O on goethite (100) surface. (Fe: surface Fe atom O: oxygen atom from water).....	46
Figure 4.6: Correlation of surface Fe-OH <sub>2</sub> bond length with Hbond1 (bond length and angle) on goethite (100) surface.....	47
Figure 4.7: (Color) The localized wannier orbitals of three types of water.....	47
Figure 4.8: Wannier orbitals for spin up (left) and spin down (right) lone-pair electron of oxygen atom in water molecule bonded to Fe on surface.....	48
Figure 4.9: Electron density difference before and after water layers absorption on goethite (100).....	48
Figure 4.10: O-O radial distribution functions for oxygen atom (first O in O-O) from different types of waters.....	49
Figure 4.11: Power spectrums of different types of water molecules and OD group on surface.....	49
Figure 4.12: Exchange of Fe bonded water molecule on goethite (100) surface with bulk water .....	50
Figure 4.13: The stage of water molecules competing to be bonded on surface.....	50
Figure 5.1: Hematite (001) and (012) surfaces terminations used in this chapter.....	70
Figure 5.2: Water molecule absorbed on different hydration models for hematite (012) surface. (A) and (B) are side-views of Model 1, (C) and (D) are side-views of Model 2.....	70

Figure 5.3: Structure of Hematite (001)–water interfaces .....	71
Figure 5.4: Structure of Hematite (012) –water interfaces.....	71
Figure 5.5: Electron density profiles for hematite-water interfaces.....	72
Figure 5.6: Radial distribution functions (RDFs) of Fe-O and O-O for hematite (001) and (012) water interfaces.....	73
Figure 5.7: RDF of oxygen atoms on hematite (001) and (012) surfaces in aqueous interfaces (O'-O'': O' and O'' are both surface oxygen atoms).....	74
Figure 5.8: Computed power spectrums of two types of OD groups on hematite (012) surface, water on interfacial region and bulk region.....	75
Figure 5.9: HOMOs of Fe(II) ions absorbed on hematite (001) and (012) surfaces in aqueous interfaces upper: (001), lower: (012).....	76
Figure 5.10: Projected density of states of different atoms in the system which has Fe(II) ion absorbed on hematite (001) in its aqueous interface (Fermi level: 0 eV).....	77
Figure 5.11: Projected density of states of different atoms in the system which has Fe(II) ion absorbed on hematite (012) in its aqueous interface.....	78
Figure 6.1: Two terminations of Al <sub>2</sub> O <sub>3</sub> (001) surfaces.....	87
Figure 6.2: Projected density of states for atoms in surface and bulk region of Al-terminated corundum (001) using DFT.....	88
Figure 6.3: Electron density profiles of three simulations and best XR fit model for corundum (001) aqueous fluid interface. (upper: three simulations comparison; middle: best XR fit model and profile from 2by2_thin_corundum_thin_water full simulation; lower: best XR fit model and water only density from simulation).....	89
Figure 6.4: Comparison of heights of different layers from AIMD to X-Ray (vertical offset chosen to maximize overall agreement).....	90
Figure 6.5: Comparison of different layers' root mean square widths from AIMD to X-Ray.....	90
Figure A.1: Comparison of the pseudowavefunctions (dashed lines) with the full-core atomic valance wavefunctions (solid lines) for Fe <sup>3+</sup> . The lower panel shows the corresponding pseudopotentials.....	101



## LIST OF TABLES

Table 3.1: Lattice parameters of the convention cell of Corundum calculated using LDA, PBE, and PBE0 plane-wave DFT calculations.....	21
Table 3.2: Bonds lengths and atoms center distances of Corundum calculated using LDA, PBE, and PBE0 plane-wave DFT calculations .....	22
Table 3.3: Lattice parameters for Hematite and Goethite calculated using LDA, PBE and PBE+U plane-wave DFT calculations. ....	22
Table 3.4: Bonds lengths and atoms center distances within the unit cell for goethite and hematite calculated using LDA, PBE, PBE+U and PBE0 plane-wave DFT calculations.....	23
Table 3.5: Band gap for corundum, hematite and goethite.....	23
Table 3.6: Local magnetic moment for each Fe site in hematite and goethite.....	23
Table 3.7: Energy difference between spin configurations of the hematite cell by DFT and DFT+U.....	24
Table 4.1: Calculated parameters defined in figure 4.3 (the right column data is from AIMD, other three are from DFT optimization).....	42
Table 4.2: Hydrogen bonds for 3 types of water molecules.....	43
Table 4.3: Wannier orbital center analysis for 3 types of water molecules.....	43
Table 5.1: Energy difference between different magnetic states configurations.....	67
Table 5.2: Interlayer spacing (Å) at the oxygen termination hydrated surface.....	68
Table 5.3: Surface hydrogen bonds statistics on hematite (001) and (012) aqueous interfaces....	69
Table 6.1: Calculated parameters $\chi^2$ of three simulations and model-dependent fit.....	87

## ACKNOWLEDGEMENTS

First of all, I would like to thank my advisor Professor John Weare for providing all the opportunities to do this research, his guidance was the impetus that made this work possible. He is always supportive, not only in academic, also to my life and my career. I am very lucky having him as my Ph.D. advisor.

I would also like to thank Dr. Eric Bylaska in PNNL, he helped me to gain the technical skills required to carry out this work. It was my great pleasure working with him in my trips to PNNL. I am also grateful to my colleagues Teerapong Pirojsirikul, Duo Song, Wasut Pornpatcharapong and Houdong Hu for their helps and inspirations in many ways. I would like to express my thanks to my collaborators Dr. Paul Fenter in ANL and Dr. Jeff Catalano in WUSTL for their valuable discussions. I would like to express the deepest gratitude to my other committee members: Prof. Michael Holst, Prof. J. Andrew McCammon, Prof. Michael Galperin, Prof. Cliff Kubiak for their time and guidance.

I especially thank my family members. Thanks to my parents Mr. Zongli Chen and Mrs. Qilin Chen for their endless love and care from my childhood. Thanks to my wife Danna Qian, marrying her was the best thing I have done. Also thanks to our expecting baby, I am so excited to have you in our lives.

Chapter 1, 2 and 3, in part, are a reprint of the material “1<sup>st</sup> Principle Estimation of Geochemically Important Transition Metal Oxide Properties: Structure and Dynamics of the Bulk, Surface and Mineral/Aqueous Fluid Interface” by Ying Chen, Eric Bylaska, John Weare, to be submitted. The dissertation author is the primary investigator and author.

Chapter 4, in full, is a reprint of the material “Density functional theory study of goethite (100) surface and aqueous interface” by Ying Chen, Eric Bylaska and John Weare, to be submitted. The dissertation author is the primary investigator and author.

Chapter 5, in part, is a reprint of the material “Ab initio study of hematite (001) and (012) surface, aqueous interface and Fe(II) ion absorption in interfaces” by Ying Chen, Eric Bylaska and John Weare, in preparation. The dissertation author is the primary investigator and author.

## VITA

2009	B.S. in Applied Physics	University of Science and Technology of China
2011	M.S. in Chemistry	University of California, San Diego
2015	Ph.D. in Chemistry with specialization in Computational Science	University of California, San Diego

## **ABSTRACT OF THE DISSERTATION**

Ab initio study of structure and dynamics of bulk, surface  
and the mineral/aqueous fluid interface regions

by

Ying Chen

Doctor of Philosophy in Chemistry

with Specialization in Computational Science

University of California, San Diego, 2015

Professor John Weare, Chair

Structures and Dynamics of bulk, surface and the mineral/aqueous fluid interface regions for geochemically important metal oxide/oxihydroxides including goethite, hematite and corundum have been investigated by performing Ab Initio study. In this dissertation, plane-wave based static optimization is used to calculate structural and electronic structural properties of mineral bulk and surface systems. Ab-initio Molecular Dynamics (AIMD) is employed to probe the dynamics properties of mineral/aqueous fluid interfaces.

In the first part, the experimental and computational progress has been introduced in chapter 1. The theoretical backgrounds and applications including first principle methods as well

as AIMD are briefly summarized in chapter 2. In the second part, the properties of mineral bulk materials are calculated and analyzed in chapter 3. The comparison of experimental and computational in structural results provides an overall understanding of the accuracies of various applications and methods in first principle framework. The analysis of electronic structure gives insight about different first principle methods in simulation. In the third part, simulations of different surface and aqueous fluid interfaces of minerals (goethite (100) in chapter 4, hematite (001) and (012) in chapter 5, corundum (001) in chapter 6) are carried out. The interaction of ordered water layers with those mineral surfaces is of great interest for both fundamental science and applications. Different studies including water adsorption process on surface, interfacial hydrogen bond analysis, types of water molecules analysis, projected density of states for interfacial atoms, electron density profiles and etc have been used to investigate the ordered water layers on surfaces.

# **1 INTRODUCTION TO MINERAL SURFACE AND MINERAL FLUID INTERFACE**

## **1.1 Progress of Mineral surface and fluid interface studies**

Reactions in the mineral surface/reservoir fluid interface control many geochemical processes such as the dissolution and growth of minerals (Yanina and Rosso, 2008), heterogeneous oxidation/reduction (Brown, 2001; Hochella, 1990; Hochella et al., 2008; Navrotsky et al., 2008), and inorganic respiration (Newman, 2010). Key minerals involved in these processes are the transition metal oxides and oxihydroxides (e.g., hematite,  $\text{Fe}_2\text{O}_3$ , and goethite,  $\text{FeOOH}$ )(Brown, 2001; Brown et al., 1999; Hochella et al., 2008; Navrotsky et al., 2008). To interpret and predict these processes it is necessary to have a high level of understanding of the interactions between the formations containing these minerals and their reservoir fluids. However, these are complicated chemical events occurring under a wide range of T,P,X conditions and the interpretation is complicated by the highly heterogeneous nature of natural environments (Hochella, 1990; Hochella et al., 2008; Navrotsky et al., 2008) and the electronic and structural complexity of the oxide materials involved(Cox, 1992; Kotliar and Vollhardt, 2004; Navrotsky et al., 2008). In addition, also because of the complexity of the minerals involved and the heterogeneous nature of natural systems the direct observation of these at the atomic level is experimentally extremely difficult. It is now accepted that theoretical simulations will provide important support for analysis of the geochemistry of the mineral surface/fluid region as well as provide essential tools to extrapolate laboratory measurements to the field environment.

Support for atomic level interpretation of the chemical events occurring in the surface and fluid regions has recently been supported by the rapid development of new high-resolution spectroscopic measurements of highly ordered systems (e.g., clean well ordered surfaces with

“best possible” ordered layers) using synchrotron light sources (Catalano et al., 2010a; Catalano et al., 2010b; Fenter et al., 2010a; Fenter et al., 2010b; Fenter and Sturchio, 2004; Fulton et al., 2012; Ghose et al., 2010; Huang et al., 2014a; Lo et al., 2007; Park et al., 2010; Park et al., 2005; Renaud, 1998; Tanwar et al., 2007), high resolution NMR (Anovitz et al., 2010; Anovitz et al., 2009). As well as providing new insights into the surface structure of these complex materials these observations provide a rich and challenging database for quantification of theoretical predictions.

## 1.2 Overview and Objective

The objective of this thesis is to describe some of our efforts to use first principle methods (based on direct solution to the electronic equation (Car and Parrinello, 1985a; Marx and Hutter, 2012; Remler and Madden, 1990)) to analyze and interpret these data (atom and electronic structure) as well as provide a means to extrapolate observations on highly ordered materials to the much more heterogeneous natural environment. The target of our recent calculations has been the structure of the surface interface and the development of methods to simulate this very disordered region. Because of the weak interactions of the species ( $\text{H}_2\text{O}$  molecules, solutes etc.) in the interface at finite temperature they are in constant motion. The measurements those are available (e.g. X ray diffraction (Brown and Sturchio, 2002; Fenter, 2002)) are of the average (equilibrium) structure of these mobile systems. This means that in order to interpret the data a dynamical theory of the atomic motion in the interface region must be used. The need to seamlessly model the transition metal bulk, solid surface, fluid interface and fluid bulk poses a difficult problem for simulation because the changes in bonding character from bulk type ionic and covalent bonding in the solid material, to polarized closed shell/ hydrogen bonding (H-bonding) in the interface region and to closed shell/H-bonding water-water and water solute interaction in the bulk fluid region.



The focus of this article will be dynamical simulations at the 1<sup>st</sup> principle level. These methods avoid the problem of defining empirical force fields by calculating the interactions between atoms on the fly in the three regions (mineral, interface, and solution bulk) directly from various levels of approximation to the electronic Schrödinger equation (herein called *ab-initio* molecular dynamics, AIMD (Car and Parrinello, 1985a; Marx and Hutter, 2012; Remler and Madden, 1990)). There have been a number of efforts to model the dynamical behavior of these systems using conventional molecular dynamics (CMD) based on empirical potentials (force fields) (Kerisit, 2011; Kerisit et al., 2012; Rustad et al., 1996; Shroll and Straatsma, 2003). While these calculations have led to important insights detailed interpretation of data is limited by the difficulty of defining potential parameters (empirical force fields) that reflect changes in bonding character (electronic structure) in the three regions (Kerisit et al., 2012). On the other hand while AIMD methods provide a more reliable description of the changing interactions in the system, the calculation of the forces for these complex systems from 1<sup>st</sup> principle methods is much more demanding in terms of computer time. Therefore, the limitations as to the equilibration of the system and the number of atomic species that can be considered are more restrictive for the AIMD methods than the CMD methods. We believe that the results that we present below are close to the limit of what can be practically calculated with presently available computational platforms. There have been several previous efforts to calculate the properties of transition metal oxides surface properties for geochemical applications using 1<sup>st</sup> principle methods (Becker et al., 1996; Kubicki et al., 2008b; Rosso and Rustad, 2001).

The transition metal oxides and oxihydroxides and their interface behavior are also important to other technological applications such as solar hydrogen production, heterogeneous catalysis, and magnetic materials applications (Renaud, 1998; Valdes et al., 2012). 1<sup>st</sup> principle calculations for these systems have also been reported (Huda et al., 2010; Pozun and Henkelman, 2011; Valdes et al., 2012). The calculations reported here have all been done using the NWChem

software which can be down loaded from <http://www.nwchem-sw.org/index.php/Download>.

These application packages have been designed for implementation on highly parallel computers.

## 2 FIRST PRINCIPLE METHODS AND ITS APPLICATION

### 2.1 Modeling complexity of Mineral surface and Interface with fluid

In order to model interactions of transition metal oxide minerals with solution interfaces it is necessary to have an adequate representation of the bulk/surface region (10-15 Å), the interface water/solute region and the bulk solution region. For the transition metal oxides the computational complexity is greatly increased by the highly correlated nature of these materials and the complexity of the unit cell. The local character of the electrons in the 3d atomic orbitals in these materials leads to local spin ordering within the unit cell. These effects are extremely difficult to capture theoretically and remain a current topic of theoretical research in condensed matter physics (Kotliar and Vollhardt, 2004). As will be discussed in more detail below there are significant problems with the application of density functional methods to these problems. However, at the very least the spin ordering in these systems requires single electron orbital occupation (e.g., the number of orbitals equals the number of electrons, roughly 1000 electrons in the calculations reported below). For surfaces interacting with a loosely bound fluid layer the observed structure (e.g. CTR measurements(Fenter and Sturchio, 2004)) represents the equilibrium average of the positions of the solution species (H<sub>2</sub>O and dissolved solutes). The strength of interaction and the nature of the bonding of the species (e.g., highly polarized and hydrogen bonding for H<sub>2</sub>O) varies with the position of the molecule in the mineral/fluid interface. This effect is incorporated in the AIMD simulation but the number of particles required to capture changes in bonding due to local and long-range interactions greatly affects the time required for simulation. Typically dynamical simulation time scales of 100 or less picoseconds can be practically reached.

### 2.2 Introduction of First Principles method

### 2.2.1 Introduction to Kohn-Sham equation

The calculation of the electronic structure of a highly correlated system is a problem of current interest in condensed matter physics (Kotliar and Vollhardt, 2004). Fortunately there is an approximate approach, the density functional theory of Hohenberg, Kohn and Sham (Hohenberg and Kohn, 1964; Kohn and Sham, 1965b; Parr and Yang, 1995), which provides estimates of many properties at a practical computational cost. Though not expected to provide more than qualitative accuracy for spin dependent properties essentially all AIMD methods implement this approach. To clarify the following discussion it will be useful to briefly outline some of the aspects of this theory that affect the accuracy of the simulations and its application to highly correlated systems.

Hohenberg and Kohn demonstrated that the total electronic energy of a many electron system may be written as a functional of the electron density (Hohenberg and Kohn, 1964; Kohn and Sham, 1965b; Parr and Yang, 1995). That is,

$$E[n(\vec{r}), \vec{R}_\alpha] = \sum_i \left\langle \psi_i^{KS} \right| -\frac{1}{2} \nabla^2 \left| \psi_i^{KS} \right\rangle + \int V_{\text{ext}}(\vec{r}, \vec{R}_\alpha) n(\vec{r}) d\vec{r} + \frac{1}{2} \iint \frac{n(\vec{r})n(\vec{r}')}{|\vec{r} - \vec{r}'|} d\vec{r} d\vec{r}' + E_{\text{ex}}(n(\vec{r})). \quad (2.1)$$

In Eq. (2.1),  $E(n(\vec{r}), \vec{R})$  is the total electronic energy and is a function of the electron density,

$$n(\vec{r}) = \sum_{i \text{ occupied}} \left| \psi_i^{KS}(\vec{r}) \right|^2 \quad (2.2)$$

and the atomic positions  $\vec{R}_\alpha$ .  $E_{\text{ex}}(n(\vec{r}))$  is the exchange correlation energy defined in Hohenberg and Kohn (Hohenberg and Kohn, 1964; Parr and Yang, 1995).

The existence of the functional  $E_{\text{ex}}(n(\vec{r}))$  is demonstrated by the Hohenberg Kohn theorem but the form as a function of density is still a topic of much research (Becke, 2014;

Burke, 2012). In Eq. (2.1),  $\psi_i^{KS}$  are the Kohn Sham (KS) orbital wave functions (Kohn and Sham, 1965b) found from the constrained variation of the total energy as (Parr and Yang, 1995),

$$\left[ -\frac{1}{2}\nabla^2 + V_{ext}(\vec{r}, R_\alpha) + \frac{1}{2} \int d\vec{r}' \frac{n(\vec{r}')}{|\vec{r} - \vec{r}'|} + v_{exc}(n(\vec{r}')) \right] \psi_i^{KS} = \epsilon_i \psi_i^{KS}. \quad (2.3)$$

The orbital KS functions must be constrained to be orthonormal,

$$\langle \psi_i^{KS} | \psi_j^{KS} \rangle = \delta_{ij} \quad (2.4)$$

$v_{exc}(n(\vec{r}))$  is the exchange correlation function defined by functional variation of Eq.(2.1). The many-body wave function for all electrons is formed from the simple product of the KS wave functions as,

$$\Psi = \prod_{i \text{ filled}} \psi_i^{KS}(\vec{r}_i). \quad (2.5)$$

## 2.2.2 Introduction to Ab-initio Molecular Dynamics

Our objective is to calculate the dynamics of the system from the solution to the KS equations, Eq.(2.3). The Hellmann-Feynmann theorem then gives for the atomic forces,

$$\vec{F}_\alpha(\vec{R}_\alpha) = -\langle \Psi | \frac{\partial E}{\partial \vec{R}_\alpha} | \Psi \rangle \quad (2.6)$$

Given the forces we can write Newton's equations of motions as,

$$M_\alpha \ddot{\vec{R}}_\alpha = \vec{F}_\alpha. \quad (2.7)$$

Time integration of Eq. (2.7) provides the 1<sup>st</sup> principle dynamics of the system of particles (AIMD) by the KS equations, Eq. (2.3). Car and Parrinello (CP) (Car and Parrinello, 1985a) have introduced a modification of Eqs. (2.3) to (2.8) that can lead to a more efficient algorithm. These equations are used in most of the dynamical calculations reported below. In this algorithm the

dynamical variables are expanded to include the KS wave functions and fictitious dynamical equations. Lagrange multipliers,  $\epsilon_{ij}$ , maintain orthogonality between the KS orbitals. The dynamical equations for this approach are modified to be,

$$\mu \ddot{\psi}_i^{KS} = \left[ -\frac{1}{2} \nabla^2 + V_{ext}(\vec{r}, R_\alpha) + \frac{1}{2} \int d\vec{r}' \frac{n(\vec{r}')}{|\vec{r} - \vec{r}'|} + v_{exc}(n(\vec{r})) \right] \psi_i^{KS} - \sum_{j \text{ filled}} \epsilon_{ij} \psi_j^{KS}. \quad (2.8)$$

In Eq. (2.8),  $\ddot{\psi}_i^{KS}$  is the fictitious acceleration of the KS wave function. A corresponding fictitious kinetic energy  $K.E._\psi$  of the wave function degree of freedom may also be computed. The magnitude of  $K.E._\psi$  is controlled by the fictitious mass  $\mu$  and must be kept small for realistic dynamics for the real position variables,  $\vec{R}_\alpha(t)$ . This propagation must be carried out with the orthonormality constraints, Eq. (2.4) held tight (Car and Parrinello, 1985a; Marx and Hutter, 2012; Remler and Madden, 1990).

### 2.3 Choices affect the accuracy and efficiency of the calculation

To further define Eq.s (2.1) to (2.8) for application to model systems, choices must be made that affect the accuracy and efficiency of the calculation. In the following we briefly identify these choices. Considerably, more complete discussions of some of the more complex of these are given in the Appendices.

#### 2.3.1 Brillouin zone sampling and plane-wave basis

The first consideration that must be made is the number of atoms (number of electrons,  $N$ ) to be included in the simulation. The numerical work in the calculation scales as  $N^3$ . For the problems we will discuss below the target systems are periodic bulk materials (3d periodicity, test calculations, see below) or perfect surface terminations with disordered fluid interfaces (2d

periodicity). For the bulk phases the periodic unit cell defines the minimum size of the calculation with appropriate Brillouin zone sampling (Ashcroft and Mermin, 1976; Ziman, 1972). (In some cases we use a big unit cell to avoid Brillouin zone sampling (Remler and Madden, 1990; Ziman, 1972). For interface problems we use a slab construction (limited number of bulk layers). For some problems in order to model changes in the surface fluid structure we will use an enlarged surface unit cell. This will be indicated in the calculations discussed in the application chapters below.

To solve Eq. (2.3) and Eq. (2.8) in a numerical way, the KS functions must be expanded in a basis. Two common choices are local functions (atomic like typically used in molecular calculations)(Szabo and Ostlund, 1996) and plane waves (typically used in condensed matter calculations) (Ashcroft and Mermin, 1976; Car and Parrinello, 1985a; Marx and Hutter, 2012). To achieve the efficiency necessary for dynamical simulations the calculations that we report here utilize plane waves. (However, there are efficient local basis dynamical methods.(Marx and Hutter, 2012) In either choice the basis must be large enough so that the solutions to the KS PDEs (e.g., Eq. (2.8) or (2.3)) are close to the intrinsic accuracy of the DFT approximations.

### 2.3.2 Exchange-correlation potential and pseudopotentials

The partial differential equations Eq.s (2.3) or (2.8) are not defined until the external potential,  $V(n(\vec{r}), \vec{R})$ , exchange correlation function,  $v_{exc}(n(\vec{r}))$  and the fictitious mass,  $\mu$  are defined.  $\mu$  is a parameter that controls how tightly the KS DFT equation constraint, Eq.(2.8), is maintained. As  $\mu = 0$  the usually KS equation is closely constrained, but the fictitious dynamics of the wave functions is very fast implying that either the time integration step must be kept very short or the system will not stay close to the Born-Oppenheimer surface defined by the KS solution to Eq.(2.3). Also as  $\mu$  increases there is larger transfer of energy into the fictitious

kinetic energy of the electronic degrees of freedom (Remler and Madden, 1990), i.e., the total energy in real structural coordinates will not be conserved. Generally a compromise must be made between efficiency of the CP algorithm and the retention of the K.E. in the particle degrees of freedom ( $K.E._\psi$  kept small).

The exchange-correlation potential,  $\nu_{exc}$ , is an unknown function and must be considered as part of the phenomenology of DFT. There have been many efforts to develop functions that will represent accurately a large number of systems (Becke, 2014; Burke, 2012; Luo et al., 2014; Zhao and Truhlar, 2008). These include purely local functions (LDA) (Kohn and Sham, 1965b), semi-local functions (e.g., PBE96 (Perdew et al., 1997)) and many others (Zhao and Truhlar, 2008)). In highly correlated systems exchange is particularly important and exact exchange corrected functionals (hybrid functionals) are frequently used. In these functionals the performance of semilocal functionals (e.g., PBE96) may be improved by the addition of Hartree Fock exchange (Szabo and Ostlund, 1996), again there are several choices (Becke, 2014). Below we will present computational results that evaluate the use of several of the most popular versions of exchange correlation (e.g., PBE96 (Perdew et al., 1997), PBE0(Adamo and Barone, 1999) for calculation applicable to the transition metal oxide fluid interface.

The external potential,  $V(n(\vec{r}), \vec{R})$ , representing the attractive interaction between the electrons and the atomic nuclei centers is the remaining function in Eq.s (2.3) and (2.8) that must be specified before calculation. In an all electron calculation this potential is easily defined in terms of the nuclear charge and position,  $Z_\alpha$  and  $\vec{R}_\alpha$ . The core electrons and other valence electron self consistently screen these potentials. However, the effective atom-electron potentials experienced by the valence electrons even with this screening are fast varying near the nuclear centers. In addition the orthogonality of the valence solutions to the core atomic like states in heavy atoms creates nodes in the valence orbital functions also resulting in their fast variation. To



expand these rapid changes in plane waves would require an impractically large basis. (There are similar problems even when local basis functions are used). In addition the magnitude of the computational problem is a function of the number of KS orbital functions retained in the calculation (leading to an approximately  $N^3$  scaling). With the expectation that bond formation between atoms in a condensed system is accounted for by the valence electrons (wave functions), it is common to develop potentials (pseudopotentials) that operate only on the valence wave functions. The idea behind these potentials is that a much smoother potential may be developed for the valence electrons that can still provide accurate bond energies and wave function variations in the bonding region and the introduction of these potentials removed the need to include core orbitals. There is an extensive literature in this area (for example Pickett (Pickett, 1989)). The general theory is discussed in more detail in Appendix A.1.

It is important to point that pseudo potentials are developed from atom calculations done at the same level as proposed for the full many atom condensed phase calculation. Therefore, the use of pseudopotentials does not represent a parameterization of the target condensed phase problem. However, there are issues that must be addressed that affect the transferability of the pseudopotentials from the atomic problem to the condensed matter problem (these are discussed more thoroughly in Appendix A.1). Possibly the most important decision that has to be made is how many valence orbitals on a particular atom will contribute to the structure of the valence band. As we have mentioned the time to solution for the algorithm increases dramatically as the number of valence orbitals increases. So the number of orbitals retained in the calculation is a critical decision (see Appendix A.1). For the 2<sup>nd</sup> row elements (see the corundum calculations below) this is fairly straightforward. The  $n_p=1$  ( $n_p$  is the principle quantum number) 1s orbital function in the core is well separated from the  $n_p=2$  2s and 2p orbital functions. On the other hand for 3<sup>rd</sup> row elements the separation between the 3s and the 3p functions in the  $n_p=3$  shell is not sufficient (even on the right hand side of the periodic table) to suppress hybridization in

condensed materials(Kawai and Weare, 1990). So for these materials the 2s and 2p orbital pseudopotentials are needed.

For the 3<sup>rd</sup> and higher periods this decision is tricky. For example for the 3d iron atom (an important component of the transition metals of interest to this work) the 3s, 3p, 3d and 4s are all candidates for hybridization. For efficiency the five 3d orbitals and the fact that there may be high spin and low spin configurations already creates a difficult problem. But for these atoms we have found that the 3s and 3p orbitals that are filled in the isolated atom may play a role in the bulk bonding problem (Fulton et al., 2010). Including these orbitals is straightforward (see Appendix A.1) but does increase the cost of the calculation. In the next section we will discuss this issue by direct comparison of calculated results to observed bulk properties. These calculations will illustrate the level of DFT theory that is necessary to describe (even qualitatively) transition metal oxide minerals and also set the stage for the discussion of the affects of adding a fluid interface in the chapters following.

### 3 ACCURACY OF CALCULATIONS OF OBSERVABLE BULK PROPERTIES

#### 3.1 Bulk Structural Properties

A first consideration in the development of an atomic level model is to establish the expected accuracy of the methods of calculation that you intend to use (or can practically use). In this chapter I will evaluate the accuracy of the application of the approaches that we have discussed when used to calculate bulk properties (a relatively inexpensive calculation). Similar calculations and comparisons to solution properties may be found in our recent efforts to simulate X-ray structures of aqueous solutions (Fulton et al., 2010). In the following chapters, I will discuss the application to surface and mineral/fluid interface problems.

As test systems we use two transition metal oxide minerals that are directly involved in the geochemical applications that are important to our research program. These are the transition metal oxide hematite ( $\text{Fe}_2\text{O}_3$ ) and the oxihydroxide goethite ( $\text{FeOOH}$ ). The structures of the unit cells of these solids are given Fig. 3.1. Because of the d electron occupation of these materials the development of an appropriate model for their electronic structure leads to some uncertainty (difficult choices) in the development of pseudopotentials and in the level of exchange used. In order to compare the accuracy of these calculations to a very well determined mineral we include similar calculations of corundum ( $\text{Al}_2\text{O}_3$ ). This mineral has a structure similar to hematite but the pseudopotential is more straightforward to develop and the electronic structure calculation is relatively easy because it is closed shell.

Table 3.1 and 3.3, summarize our calculations of the bulk unit cell structures given in Fig. 3.1 using the various levels of approximation discussed in Section 2 and the Appendix. The estimates of the bond lengths illustrated in Fig. 3.1 are given Table 3.2 and 3.4.

##### 3.1.1 Structural properties of corundum

The unit cell structural parameters for this mineral are reported at various levels of electronic structure calculation (LDA exchange+ correlation calculated from local density, PBE96 local density type exchange + correlation with density gradient corrections and the considerably more computationally expensive PBE0 GGA + exact exchange calculation) are summarized in Table 3.1. The relatively simple LDA calculations provide reasonable results comparing to experiments, with the difference around 2.0%. However, using this level of approximation of DFT the bonds are usually shorter than experimental observations. The semi local GGA calculation (PBE96), which can be done for roughly the same computational cost as LDA are much better, within about 0.2%. We note that for this mineral the higher level electronic structure calculation, PBE0, provides slightly less accuracy 1.6%, PBE0 is about the highest level calculation that can practically be done for these minerals. This is a bit discouraging. However, the excellent results from the more efficient GGA calculations are quite positive. Problems of this sort are common in DFT structural calculations. There will be much more support for the PBE0 type calculations in the electronic structure calculations for the spin ordered systems hematite and goethite which are the real interest of our program. The bond lengths for corundum given in Table 3.3 show the same trends. Again the LDA calculations are short. GGA calculations provide predictions that are in better agreement with the structural data and PBE0 calculations not quite as good as the GGA calculations. While changes can be made to the functional (Pozun and Henkelman, 2011) or other functionalities (Zhao and Truhlar, 2008)) we believe that this is the best level of agreement that can be obtained.

### 3.1.2 Structural properties of hematite and goethite

In Table 3.3 and 3.4 structure calculations at the various levels are reported for Hematite and goethite. Consistent with this the LDA results are significantly worse than the PBE96 results. The average agreement for unit cell parameters is  $\sim 0.1 \text{ \AA}$  ( $\sim 1.5\%$ ) for the PBE96 and PBE0,

whereas the LDA result is  $\sim 0.3 \text{ \AA}$  ( $\sim 3.0\%$ ). Due to the strongly correlated nature of d electrons for these systems, GGA calculations are expected to be less accurate than the hybrid calculations (Luo et al., 2014). From Table 3.4, the bond length (Fe-O bond) difference within the unit cell is less than  $0.02 \text{ \AA}$  ( $\sim 1\%$ ) for the hybrid calculation (PBE0) which is more accurate than the  $0.05 \text{ \AA}$  ( $\sim 2\%$ ).

Note on the accuracy and consistency of XRD measurements: Considering the dispersion of an x-ray source and the error of the aligned the instrument, the expected precision of lattice parameters and bond lengths in a single observation can be up to  $0.00001 \text{ \AA}$  to  $0.0001 \text{ \AA}$ . (Herbstein, 2000). However there are issues with the reproducibility of reported structures from similar experimental setups. For example, the difference of hematite lattice parameter between Blake's measurement (Blake RL, 1966) and Finger's (Finger and Hazen, 1980) work is  $\sim 0.03 \text{ \AA}$ . These differences between intrinsic error and reported differences could be due to disorder of crystal samples, thermal and other effects.

An additional problem is the accuracy of the pseudopotential representation of the atomic potential. If the  $\text{Fe}^{3+}$  3s and 3p play a role in the hybridization of the d band they need to be included in the pseudopotential of the valence band (see Appendix). While the atomic energies of these orbitals are well below the 3ds (around 30 e.V. below bottom of d bands in DFT) we have found in prior aqueous solution simulations that their inclusion improves the M-O bond lengths in the solution phase (Fulton et al., 2010). Results including the 3s and 3p in the valence structure are included in Table 3.3. In these applications we found that the results generated from the two pseudopotentials have similar accuracy. This suggests that without losing much accuracy in goethite and hematite surfaces simulations, we can use an Fe pseudopotential which puts the 3s 3p orbitals in the core leading to a more efficient calculation.

The full hybrid exchange calculation is very expensive for dynamical simulation. To add some correlation in the calculation for these highly correlated minerals we implemented a

DFT+GGA +U type calculation (see Appendix)(Anisimov et al., 1993; Dudarev et al., 1998; Liechtenstein et al., 1995; Rollmann et al., 2004; Zhou et al., 2004). By providing an approximate exact exchange correction this kind of calculation provides some improvement over GGA at very small computational cost. The data in Table 3.3 and 3.4 shows that the DFT+U calculation still gives very good ~2% for bond lengths. DFT+U framework has been discussed in Appendix. DFT+U parameter U and J for Fe atoms are set to be 4 eV and 1 eV respectively which has been widely accepted and proven to be the most appropriate constant values for Fe in hematite and goethite (Rollman 2004, Tunega 2002). In addition the results in the next section show that this model also provides a reasonable estimation of the electronic structure properties of these materials.

## 3.2 Bulk electronic structural properties

### 3.2.1 Band gaps

The calculated band gaps defined in these calculations to be the energy difference between the highest filled and the lowest unfilled state for the three minerals are reported in Table 3.5. For corundum, the band gap calculated using DFT+GGA (PBE96) is 7.0 eV, while hybrid functional PBE0 gives 9.33 eV which is in better agreement with the experimental value of 8.8-10.8 eV (Perevalov et al., 2007; Tews and Gründler, 1982). For the transition metal oxide and oxihydride the band gap is very sensitive to level of calculation showing large differences as illustrated in the Table 3.5. It is well known that DFT+GGA gives band gaps that are far too small. It is also well know that HF gives band gap estimates that are very large. This is consistent with the results in Table 3.5. We note that DFT+U and PBE0 give similar and estimates. Both are much better than produced by DFT+GGA. DFT + U produces best results but it is parameterized via the U and J value. To some extent, this excellent agreement is questionable since this U value (U=4 eV) is chosen by comparing the DFT+U calculated properties using different U values

(band gap, local spin moment, unit cell volume and etc.) with experimental results (Rollmann et al., 2004). However, as discussed in the Appendix the DFT+U level of the theory is computationally much more efficient (roughly similar to the DFT calculation). This supports the use of this level of theory in the much larger surface + interface problems reported below. The general conclusion is that some level of correlation (hybrid DFT, DFT+U) must be included in order to have any agreement with observations when calculating electronic structures of transition metal oxide or oxihydride. Similar conclusions are derived from the local spin estimation and projected density of states in the following subsection.

### 3.2.2 Spin configuration in hematite and goethite

As a result of the strongly local behavior of the 3d wave functions (near 3d orbital functions) near, the  $\text{Fe}^{3+}$  centers is qualitatively described as a high spin transition metal ion. (Cox, 1992) In a ionic lattice model of a solid (Cox, 1992) each ion would have a spin of  $5/2 \mu_B$ . Goethite and hematite are antiferromagnetic materials with a total unit cell spin of 0. However, since there are several  $\text{Fe}^{3+}$  in the unit cell of these minerals (4  $\text{Fe}^{3+}$  in goethite 16 atoms cell and 12  $\text{Fe}^{3+}$  in hematite 30 atoms-hexagonal representation) there may be several possible arrangements of the localized spin within the unit cell. This alignment of the local spins in the unit cell will affect the energy. We can use the theory we implement to predict the lowest energy ordering for such systems.

Because of electron delocalization, the electron spin localized on a single atom in a bulk system may be quite different from that of the isolated ion. In the delocalized electron picture we are using the minimum energy of the unit cell which will depend both on the level of calculation we use and the distribution of spins in the unit cell. To allow spin order in the bulk unit cell each electron occupies a single spin orbital. Consistent with the antiferromagnetic property of the minerals the total spin of the unit cell is held to be zero by equal occupation of spin up and spin

down orbitals. Even though the total spin in the unit cell is constrained to be zero, the local spin projection on various Fe ions may be different because of the breaking of translational symmetry of the 3d band states within the unit cell. In order to quantify the localized spin a localized representation of the d band atomic occupation must be projected out of the d calculated band. In the calculations reported here local projectors are constructed from the localized atomic functions used to produce the iron pseudopotentials (see Appendix A.1).

Briefly to generate a minimum energy spin ordered state we first equally fill the up and down orbital states. This insures that the system will reach an antiferromagnetic state in the unit cell. Despite the great flexibility we have in the basis set (many plane waves) DFT solvers have a difficult time finding spatially localized states. To help them out we begin the calculation by generating a spin ordered state in the unit cell by giving weight (via a spin penalty function also based on the atomic projectors, see Appendix A1) to the pseudo potential on ion sites. Spin localization (breaking the symmetry) will lead to a more stable energy and break the local symmetry of the unit cell. This will create spin localization with the penalty potential turned on. If the ordered spin state is stable, the spin structure will be retained on further optimization after the constraint is removed. That is how we will produce locally stationary states. We then use this procedure to generate spin trial localized states with different orderings. With further optimization these states have different energies and we can select the lowest state as the potential ground state.

The ordering and magnitude of the local spin could vary with level of calculation (e.g., DFT, DFT+U, or PBE0). Results for the local spin moments (the calculated number difference between spin-up and spin-down electrons on each Fe center) for hematite and goethite using different levels of calculation are included in Table 3.6. Again some level of exact exchange must be included in order to approach agreement with observations. Similar to band gap, results from DFT+U and hybrid DFT agree better with experiments especially for goethite. For hematite, the



values from those two methods are lower than experiments, but still much closer comparing to pure DFT result.

In Table 3.7, we report calculated energy differences between possible local spin orderings for Fe atoms in each layer in hematite using DFT, DFT+U. As mentioned above, hematite is antiferromagnetic, so the sum of local spin moment is 0 in one unit cell. We calculated the energies for three possible spin ordering  $(+--)(++--)(+--)$  along  $[0001]$  in the hexagonal cell. (Fig 3.1.b left) The calculated energy ordering of DFT and DFT+U for different spin configurations is same. We noticed that system in  $(+--)$  spin ordering has the lowest energy. The lowest spin ordering configuration is also  $(+--)$  along  $[111]$  in the rhombohedral primitive cell. (Fig. 3.1) For comparison, the fully aligned ferromagnetic state  $(++++)$  is also calculated and the energy is higher than all three antiferromagnetic configurations. Table 3.6 and Table 3.7 emphasize that electronic structure calculations for these highly correlated materials is still pretty uncertain. In general it is expected that the PBE96 (LDA + GGA) results tend to be too delocalized (low spin moments). Adding exact exchange as in DFT+U and PBE0 produces larger spin moments. Hartree Fock (HF) tends to over localize and the spin moments for this theory are too large as compared to observations. However, consistent with the band gap calculations the conclusion is that it is necessary to include some level of exact exchange to achieve reasonable agreement with the electronic structure data.

### 3.2.3 Projected Densities of States (PDOS)

The distribution of states as a function of energy (density of states, DOS) is a property important to the prediction of conduction, bonding and spectroscopic properties of materials (Ashcroft and Mermin, 1976; Ziman, 1972). To provide more detail about the electronic structure in the unit cell here we project out of the DOS the local variation around individual

atoms which is called projected density of states (PDOS). PDOS used in our work is defined in Appendix.

Corundum is an insulator the band gap is near 7.0 e.V using DFT (PBE96) as seen in the projected density of states, Figure 6.2.A. The densities of valence bands near Fermi level are mostly from O-2p part of the band, but also contain a small Al-3s and Al-3p component. Lower energy valence bands (left peak) contain Al-3s, Al-3p and O-2s component. The peak of conduction band originates from the local Al-3s and Al-3p interaction. We have observed 3s 3p hybridization of Al atom from the projected density of states.

Projected Density of state near Fermi level for bulk hematite using different methods has been plotted in Figure 3.2. It shows DFT's difficulty in predicting band gap as we discussed above. The valence (occupied) states (left than Fermi level) have Fe-d component and O-p component. Conduction bands above the band gap are corresponding to the minority spin on the  $\text{Fe}^{3+}$  ion. (In Figure 3.2, y axis  $>0$  means spin up, it's clear that Fe-d component in valence bands are mostly spin down, and the Fe-d component in conduction bands are mostly spin up). The most important difference between the various levels of calculations is that in the DFT+U and the hybrid DFT (PBE0) calculation the occupied d band is much narrower and moved to lower energy reflecting the expected localization in a more correlated theory. This means that the states just below the band gap are mostly O sp states in these two theories. It indicates that these materials are O2p-Fe3d charge transfer insulators which are consistent with X-ray absorption and emission spectra measurements (Ciccacci et al., 1991; Dräger et al., 1992; Fujimori et al., 1986; Lad and Henrich, 1989). When using DFT functional (PBE96), more Fe-d and O-2p hybridization has been observed and it leads to states at the top of the band in hematite having the d-d character. This is another electronic structure problem by using DFT to transition metal oxides (hematite). The widths of the oxygen sp bands in all the calculations are almost the same. In all, the hybrid PBE0 and DFT +U calculations are qualitatively similar. These calculations again show that

some level of exchange beyond DFT+GGA (PBE96) is necessary to provide a reasonable interpretation for these minerals. However, in the surface and interface calculations that we report in the following section the PBE0 calculation is extremely expensive, so we do most of these calculations at the DFT+U level.

Table 3.1: Lattice parameters of the convention cell of Corundum ( $\text{\AA}$  for  $a, b, c$ ,  $^\circ$  for  $\alpha, \beta, \gamma$ ) calculated using LDA, PBE, and PBE0 plane-wave DFT calculations. 100 Ry and 200 Ry were used for the wave function and density cutoff energies. The Corundum conventional cell contains 12 Al and 18 O atoms.

<b>Lattice Parameters</b>	<b>LDA</b>	<b>PBE</b>	<b>PBE0</b>	<b>Exp.<sup>a</sup></b>
Supercell	1x1x1	1x1x1	1x1x1	
MP	2x2x1	2x2x1	1x1x1	
a	4.675	4.767	4.681	4.757
B	4.675	4.767	4.681	4.757
c	12.736	12.999	12.909	12.988
$\alpha$	90.0	90.0	90.0	90
$\beta$	90.0	90.0	90.0	90
$\gamma$	120.0	120.0	119.9	120

<sup>a</sup>Ref. (Kirkel and Eichhorn, 1990)

Table 3.2: Bonds lengths and atoms center distances (in Å) of Corundum calculated using LDA, PBE, and PBE0 plane-wave DFT calculations (100 Ry and 200 Ry were used for the wave function and density cutoff energies)

Distances	LDA	PBE	PBE0	Exp. <sup>a</sup>
Supercell	1x1x1	1x1x1	1x1x1	
MP	2x2x1	2x2x1	1x1x1	
Al-Al-a	2.611	2.666	2.638	2.654
Al-Al-b	3.757	3.833	3.816	3.840
Al-O1	1.817	1.853	1.818	1.854
Al-O2	1.941	1.980	1.962	1.971

<sup>a</sup>Ref. (Kirkel and Eichhorn, 1990)

Table 3.3: Lattice parameters for the conventional cells of Hematite and Goethite (Å for a, b, c, ° for  $\alpha$ ,  $\beta$ ,  $\gamma$ ) calculated using LDA, PBE and PBE0 plane-wave DFT calculations. 100 Ry and 200 Ry were used for the wave function and density cutoff energies. The Hematite conventional cell contains 12 Fe and 18 O atoms, and the Goethite conventional cell contains 4 Fe, 8 O and 4 H atoms. U=4 e.V. for all PBE+U calculations in this paper. The PSP1 and PSP2 pseudopotentials for Fe atom have [Ar] 3s3p and [Ar] as core.

Lattice Parameter	LDA PSP1	LDA PSP2	PBE PSP1	PBE PSP2	PBE0 PSP1	Exp.
Supercell	1x1x1	1x1x1	1x1x1	1x1x1	1x1x1	
MP	2x2x1	2x2x1	2x2x1	2x2x1	1x1x1	
A	4.683	4.498	5.154	4.947	5.122	5.036 <sup>a</sup>
B	4.681	4.499	5.155	4.947	5.122	5.036 <sup>a</sup>
C	13.515	13.228	13.820	13.602	13.63	13.747 <sup>a</sup>
$\alpha$	90.68	90.65	89.98	89.93	87.84	90 <sup>a</sup>
$\beta$	89.27	89.37	90.02	90.07	92.16	90 <sup>a</sup>
$\gamma$	119.1	119.3	119.9	120.0	119.6	120 <sup>a</sup>
Supercell	1x1x1	1x1x1	1x1x1	1x1x1	1x1x1	
MP	1x3x2	1x3x2	1x3x2	1x3x2	1x1x1	
a	9.662	9.285	10.107	9.858	9.812	9.951-9.956 <sup>b</sup>
B	2.586	2.644	3.024	2.976	3.168	3.018-3.025 <sup>b</sup>
C	4.383	4.220	4.611	4.515	4.240	4.598-4.616 <sup>b</sup>
$\alpha$	90.0	90.1	90.0	90.0	90.0	90 <sup>b</sup>
$\beta$	90.0	90.0	90.0	90.0	90.0	90 <sup>b</sup>
$\gamma$	90.0	89.9	90.0	90.0	90.0	90 <sup>b</sup>

<sup>a</sup>Ref. (Maslen et al., 1994)

<sup>b</sup>Ref.(Alvarez et al., 2008)

Table 3.4: Bonds lengths and atoms center distances (in Å) of Hematite and Goethite calculated using LDA, PBE, PBE+U, and PBE0 plane-wave DFT calculations. 100Ry and 200Ry were used for the wave function and density cutoff energies.

Distances	LDA PSP1	LDA PSP2	PBE PSP1	PBE PSP2	PBE+U PSP1	PBE0 PSP1	Exp.
Hematite							
Supercell	1x1x1	1x1x1	1x1x1	1x1x1	1x3x2	1x1x1	
MP	2x2x1	2x2x1	2x2x1	2x2x1	1x1x1	1x1x1	
Fe-O1	1.878	1.795	1.994	1.887	1.996	1.964	1.946 <sup>a</sup>
Fe-O2	1.971	1.930	2.132	2.122	2.187	2.137	2.116 <sup>a</sup>
Fe-Fe-a	2.646	2.595	2.906	2.933	2.922	2.904	2.900 <sup>a</sup>
Fe-Fe-b							
Goethite							
Supercell	1x1x1	1x1x1	1x1x1	1x1x1	2x2x1	1x1x1	
MP	1x3x2	1x3x2	1x3x2	1x3x2	1x1x1	1x1x1	
O1-H	1.093	1.094	0.973	0.968	0.982	0.963	
O2-H	1.302	1.306	1.743	1.808	1.651	1.637	
Fe-O1	1.915	1.867	2.134	2.100	2.123	2.079	2.077-2.103 <sup>b</sup>
Fe-O2	1.906	1.846	1.973	1.911	1.992	1.949	1.937-1.954 <sup>b</sup>
Fe-Fe-a	2.890	2.802	3.363	3.317	3.323	3.245	3.283-3.311 <sup>b</sup>
Fe-Fe-b	3.415	3.316	3.456	3.352	3.493	3.381	3.432-3.465 <sup>b</sup>

<sup>a</sup>Ref. (Maslen et al., 1994)

<sup>b</sup>Ref.(Alvarez et al., 2008)

Table 3.5: Band gap for corundum, hematite and Goethite

	DFT(pbe96)	DFT(pbe96)+U (U=4eV)	DFT+exchange (pbe0)	HF	Exp. <sup>a,b,c,d</sup>
Corundum E(e.V.)	7.00		9.33	24.52	8.8-10.8
Hematite E(e.V.)	0.20	1.63	5.80	15.58 (ref)	2.0
Goethite E(e.V.)	0.48	1.84	4.13	17.32	2.1-2.5

<sup>a</sup>Ref.(Perevalov et al., 2007)

<sup>b</sup>Ref.(Tews and Gründler, 1982)

<sup>c</sup>Ref.(Mochizuki, 1977)

<sup>d</sup>Ref.(Cornell, 2003)

Table 3.6: Local magnetic moment for each Fe site in hematite and Goethite

	DFT(pbe96)	DFT(pbe96)+U (U=4eV)	DFT+exchange (pbe0)	HF	Exp. <sup>a,b</sup>
hematite μ[μB/Fe atom]	3.60	4.10	4.39	4.60	4.64
Goethite μ[μB/Fe atom]	3.54	3.75	3.90	4.56	3.8

<sup>a</sup>Ref.(Coey and Sawatzky, 1971)

<sup>b</sup>Ref.(Bocquet and Kennedy, 1992)

Table 3.7: Energy difference between spin configurations of the hematite cell by DFT and DFT+U

(There are two types of Fe atoms pair in (001) and [111] directions. There are two types of Fe-Fe pairs, one pair has long distance, the other has short distance. +--+ground state means, in both directions, Fe atoms in short distance pair have same spin while Fe atoms in long distance pair have different spin. Spin up (+) and spin down (-) has been marked to the atoms in the Fig. 3.1)

	+--+	+--+	++--	++++
DFT (meV/Fe atom)	0	228.0	278.6	704.9
DFT+U(meV/Fe atom)	0	192.6	192.8	433.1

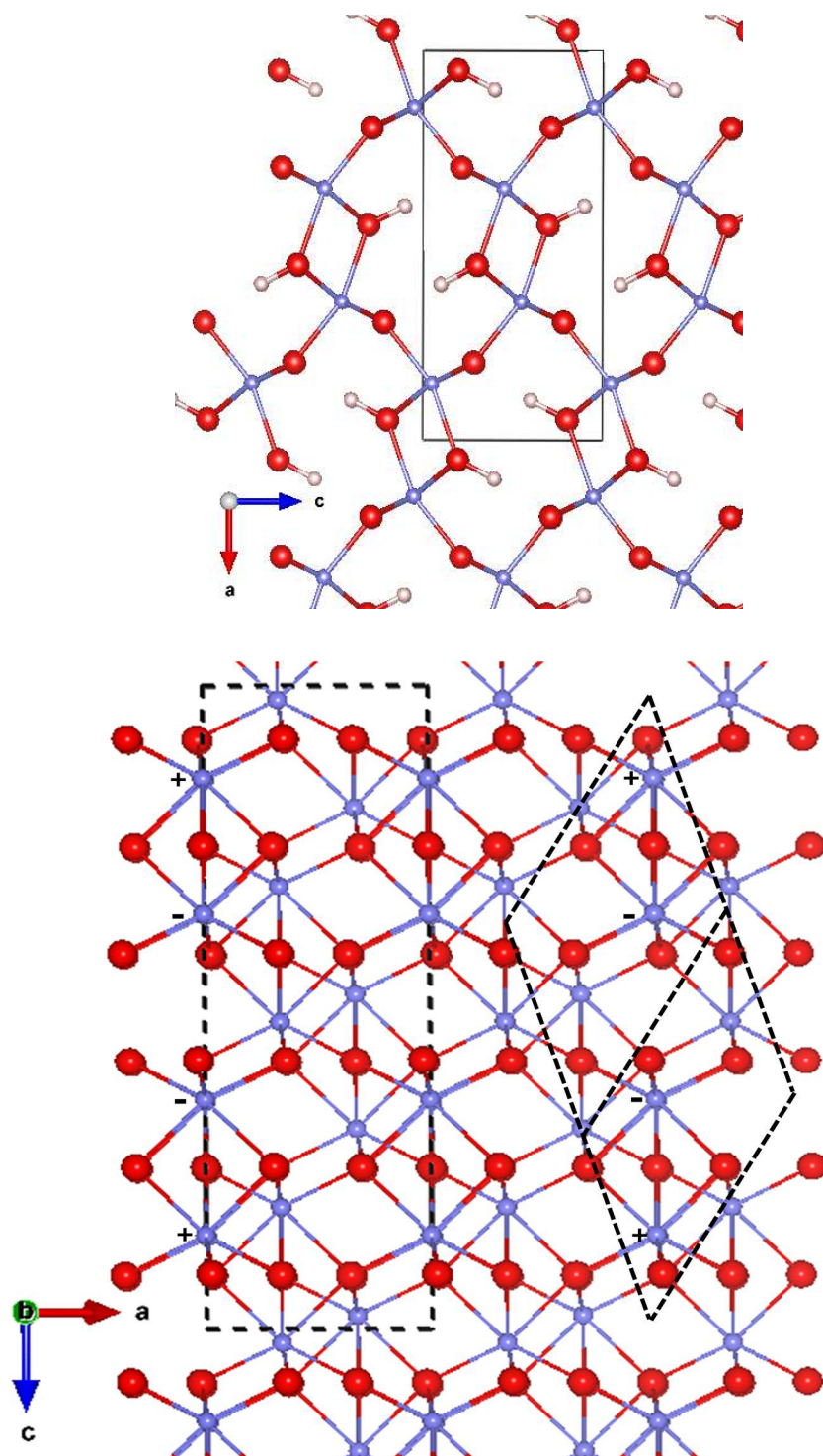


Figure 3.1: Cells for bulk Goethite, Hematite and Corundum. Hematite and Corundum have same crystal structure. Upper: goethite, Lower: hematite and corundum

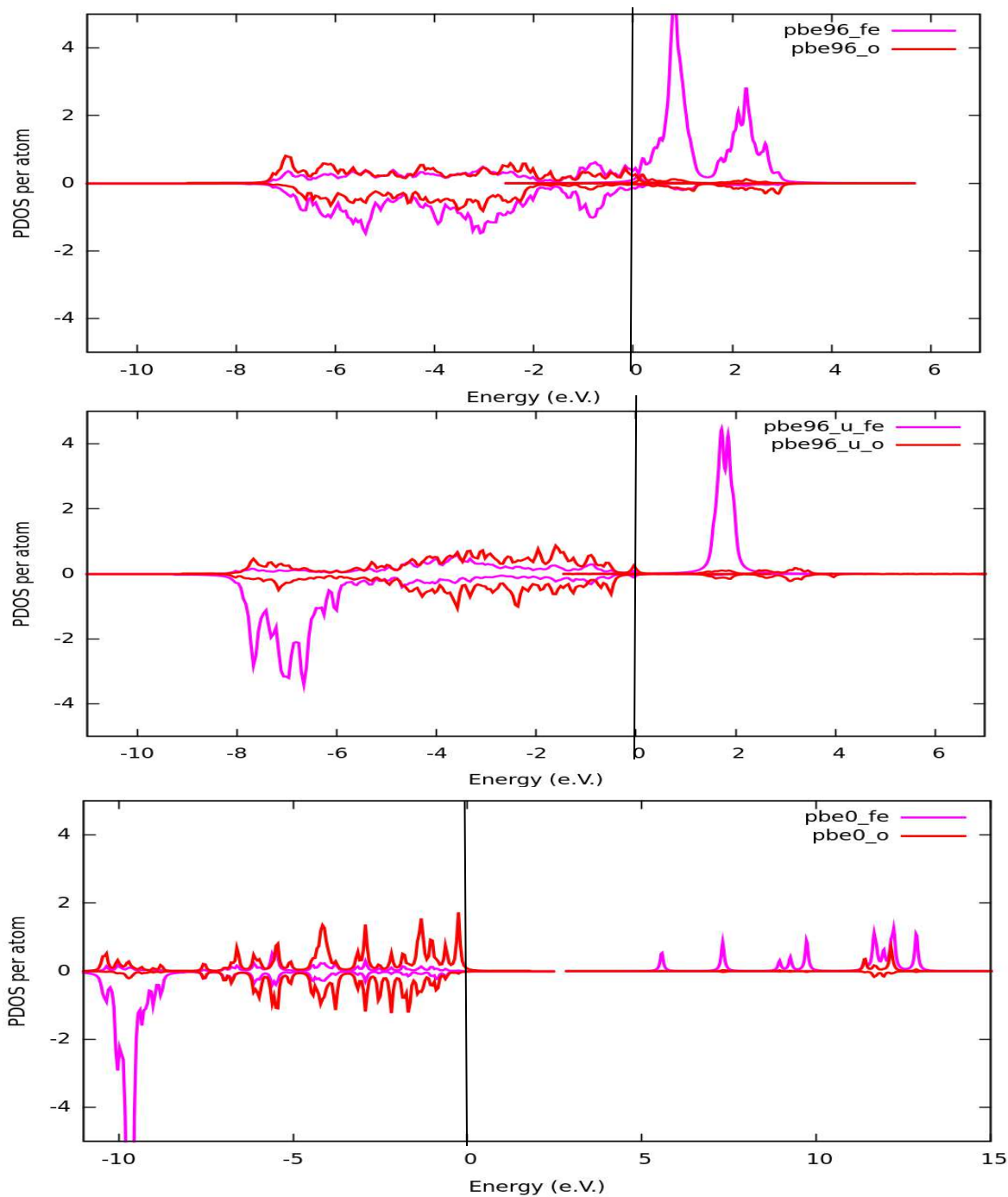


Figure 3.2: Projected Density of state near Fermi level for bulk hematite using different methods: Blue line represents PDOS for Fe atom, and red line represents PDOS for O atom. The line above the middle line ( $y=0$ ) is spin up density line, and below  $y=0$  is spin down density line. The upper, middle and lower figures are from DFT, DFT+U and hybrid DFT respectively.



## 4 STUDY OF GOETHITE (100) SURFACE AND AQUEOUS INTERFACE

### 4.1 Introduction

Goethite is a highly reactive mineral in water and soil (Cornell and Schwertmann, 2006; van der Zee et al., 2003). In goethite and water interface, many chemical processes (.ie. absorption, dissolution) happen (Brown, 2001; Brown et al., 1999; Hochella et al., 2008; Yanina and Rosso, 2008). These processes are crucial to mineral growth, bacterial living, pollution and etc. Knowledge of the goethite water interface plays an important role in understanding these reactions. (Aquino et al., 2006; Ghose et al., 2010; Shroll and Straatsma, 2003)

Although (100) is not the main crystal growth surface, it is a common surface and perfect cleavage affords experimental surface. Experimental work has been done investigating goethite (100) water interface. Recently, Ghose (Ghose et al., 2010) proposed an ordered water layers structure on goethite (010) surface after analysis Crystal Truncation Rod (CTR) result (Eng et al., 2000). Other than goethite, ordering water layers has also been found on other mineral water interface (Cheng et al., 2001; Fitts et al., 2005). The main reason forming ordered water layers is the dangling bond of atoms on the surface. Surface atoms can be saturated by forming ligand bond and hydrogen bond with the water on the surface which lead ordered water layers structure on surface.

While light atoms(.ie. Hydrogen atom) are hard to be directly measured from experiments, theoretical simulation can be useful in fully understanding the interface structure by providing direct information. MUSIC model is proven to be powerful in understanding interface structures of some systems (Fitts et al., 2005; Hiemstra and Van Riemsdijk, 1996). Classical molecular dynamics are also successful in predicting surface properties to some extent. (Boily, 2012; Fenter et al., 2013; Kerisit, 2011; Kerisit and Rosso, 2006; Kohanoff, 1994; Rustad et al., 2003; Shroll and Straatsma, 2003) Nevertheless, classical model can't account for many-body

effect which is important especially in transition metal oxides. And the transferability is another problem for most classical models. It is useful to introduce free empirical parameters first principle method (.ie. density functional theory) to describe this system. The advantage of density functional theory has been proven in huge amount of works in predicting system structures.

With first principle plane wave based methods, pure theoretical optimization can be used to study ordered system, like solid and surface, or few molecules absorbed on surface(Aquino et al., 2006; de Leeuw and Cooper, 2007; Kubicki et al., 2008a; Rustad et al., 1996; Tunega, 2012). This method is very efficient and widely used in solid state community which can predict promising low energy structures by doing small amount calculation. But if we want to include more water molecules to simulate the interface, no optimization algorithm can work effectively in global searching due to exponential increase of the degree of freedoms. To effectively sampling this system and investigating dynamic properties, ab-initio Molecular dynamics needs to be employed(Bogatko et al., 2010; Bylaska et al., 2007; Car and Parrinello, 1985b; Wang et al., 2014). Modeling mineral (goethite) and water interface needs a comparably larger cell than the cell in previous ab-initio molecular dynamics study, but with the development of supercomputers and highly parallel ab-initio Molecular Dynamics algorithm, this work becomes realistic using hundreds to thousands cpu by a reasonable computation time(Valiev et al., 2010).

In this paper, we combined plane wave based optimization and ab-initio molecular dynamics method to study goethite (100) surface, water absorption on surface and goethite water interface. Pure optimization method has been used to study dry goethite (010) surface, one and two water absorption on surface. On the other hand, we performed large scale ab-initio molecular dynamics to study water structure and surface bonding condition in goethite (010) and water interface. We did analysis to interface bonding condition and ordered water structure. Our results evidence the existence of ordered water on goethite (100) surface.

## 4.2 Details of computational methods

Plane wave density functional theory (open shell) (Kohn and Sham, 1965a) optimization is performed with NWChem software package, using PBE96 exchange correlation functional (Perdew et al., 1997). A Monkhorst-pack scheme (Monkhorst and Pack, 1976) of  $1 \times 3 \times 2$  grid point is used in calculations to electronic wavefunctions sampling. A Teter's style norm-conserving pseudopotential (Teter, 1993) with semi core was used to Fe atom in which 3s and 3p are included as core electrons. Softened Hamann pseudopotentials (Hamann, 1989) were used to oxygen and hydrogen atoms. Plane wave energy cutoff 50 Hartree for the wavefunction and 100 Hartree for the density were used. The computational cell used here is  $(20.0 \text{ \AA} \times 3.002 \text{ \AA} \times 4.581 \text{ \AA})$  which contains a  $(1 \times 1)$  (100) surface slab and a near  $10 \text{ \AA}$  vacuum slab with periodic boundary condition. The thickness of the goethite surface slab is  $9.4 \text{ \AA}$  (distance in a direction between two oxygen atoms on surface), which has four Fe layers totally. In test, other than first O and first Fe layers, inner layers atoms showed bulk structure. To simulate water absorption on surface, we added water molecules on the surface. To set up the anti-ferromagnetic configuration, a spin-penalty scheme has been used to produce the initial wavefunctions then released. (Ying Chen, 2015)

A 16ps AIMD simulation was performed within the framework of open shell DFT in NWChem software package. (Valiev et al., 2010) The system was propagated in time using Car-Parrinello Molecular dynamics (CPMD) scheme. (Car and Parrinello, 1985b) Plane wave basis and T point sampling were used to expand electronic wavefunctions. Same pseudopotential, exchange functional, wavefunction and density cutoff with plane-wave optimization part were used in this AIMD simulation. Equation of motions in CPMD were integrated using Verlet algorithm, with a time step  $0.12 \text{ fs}$  and fictitious orbital mass  $600.0 \text{ au}$ . All hydrogen atoms have been replaced by deuterium to facilitate the integration. The canonical ensemble was chosen for

this simulation, Nose-Hoover thermostat (Nose, 1984) was used to control the temperature for ions (300 K) and electrons (1200 K).

The size of the interface simulation MD cell was (9.1612 Å \* 9.006 Å \* 30.0707 Å) which had 291 atoms with zero net charge. The goethite surface part was a (3\*2) (100) surface slab which contains 24 Fe iron, 48 O and 60 H. In order to properly describe the dynamics in the interface, 65 waters (including 12 waters from goethite surface) were included in this cell. Water density was near to 1.0 g/cm<sup>3</sup>. This calculation includes 1024 electrons totally with 512 spin up electrons and 512 spin down electrons. In the initial configuration, 53 water molecules were pointed away from hydrated goethite surface, so a 1.5 ps equilibration was performed after which trajectory has been collected.

#### 4.3 Goethite (100) surface

The crystal structure of goethite is orthorhombic (space group Pbnm, Z = 4). Every Unit cell contains 4 Fe atoms, 8 Oxygen atoms and 4 Hydrogen atoms. In a direction, it has a periodic model as -Fe-OH-OH-Fe-O-O-Fe-OH-OH-Fe-O-O-(Fig. 4.1). The computation of relaxing the unit cell predicts the lattice parameter (9.952 Å, 3.002 Å, 4.581 Å) which is in consistent with experiments results.(Ghose et al., 2010; Rochester and Topham, 1979) Goethite is antiferromagnetic under the room temperature and standard pressure. DFT predicts a local spin  $S=3.5/2$  comparing to  $S=3.8/2$  very Fe site in experiment. (Tunega, 2012) For the spin configuration, calculations shows the lowest energy configuration for Fe sites is (+ - + -) in a axis (+ means spin up, - means spin down). And in each layer, Fe has the same local magnetism.

##### 4.3.1 Surface termination

In the bulk goethite, every Fe<sup>3+</sup> cation coordinates with three O<sup>2-</sup> anion and three OH<sup>-</sup> in a distorted octahedral configuration. To keep six-coordination of Fe atoms on surface for

stabilizing the surface structure, there are two possible terminations models for goethite (100) surface in Fig. 4.1. Termination I model has O<sup>2-</sup> anion layer on the surface and Termination II has OH<sup>-</sup> layer on the surface. We protonated surface oxygen atoms in both models to saturate them and keep two models neutralized in charge. Two models have same species, 4 Fe atoms, 8 H atoms and 10 O atoms. We defined

$$E(\text{surface}) = (E(\text{models}) - k * E(\text{cell}) - E(\text{extra species})) / 2A$$

Here  $k=1$ , and the extra species here are 4H and 2O, which can be counted as two water molecules. A is surface area.

After optimization, Termination I surface energy is 156.7 meV/ Å<sup>2</sup>, and surface II surface energy is 130.5 meV/Å<sup>2</sup>. This predicts surface II is more stable which is verified by experiments. (data to be updated) We use Termination II model in the whole paper.

#### 4.3.2 One water molecule absorbed on surface

We investigated the possible surface sites to attract additional water molecules. Due to the complexity of potential surface for this system and the fact searching algorithm normally works only for local minimal, we started searching by proposal three candidate sites (in Fig. 4.2). In site1, (yellow), water molecule bridges with surface oxygen by H-Bond as a donor. The protonated surface already has bonded water, water molecules in site2 (purple) and site3 (green) can form hydrogen bond with this bonded water as donor and acceptor respectively. After optimizing all three structures separately, we find site2 structure is not stable, the additional water goes away from surface. Water in site 1 and site 3 could be bonded, while site 1 structure is 3.32 KJ/mol lower than site 3 structure. So site 1 is preferred in our calculation. This could be illustrated qualitatively by the different number of hydrogen bonds water can form with the surface. When the water molecule is in site 1, there are two hydrogen bonds being created, while

only one hydrogen bond can be created if it stays in site 3. Site 2 is not a preferred structure because the oxygen of the water on the surface is already over saturated.

*Surface bond length after absorbing water molecules:*

No intense surface reconstruction had been observed in this simulation and other works for goethite (100) surface. But the bond lengths (Fe-OI, Fe-OII, Fe-OIII) on surface were distinct from bulk. (Fig. 4.3) Interestingly, the bond lengths are noticeably changed after water molecules absorption on surface. The bond length information was listed in table 4.1. Comparing dry hydrated surface with bulk, Fe-O(I) had been lengthen intensely, Fe-O(II) and Fe-O(III) had been shorten slightly. After absorbed water molecules, Fe-O(I) had been shorten dramatically, Fe-O(II) and Fe-O(III) had been lengthen slightly. Bond valance theory can help us understating these changes qualitatively.

The basic idea of the theory (Brown, 1987) is the valence  $V$  of an atom which is the sum of the individual bond valences  $v_i$  surrounding the atom should be equal to oxidation stats of atoms.

$$V = \sum(v_i)$$

The individual bond valences can be calculated from the equation below. Generally, longer bond contributes less bond valance to atoms.  $R_i$  is bond length and  $R_0$  is a parameter which keeps same for one compound. ( $b$  is 0.37)

$$v_i = \exp\left(\frac{R_0 - R_i}{b}\right)$$

In goethite, oxygen oxidation state is 2 and iron oxidation state is 3. So oxygen  $V$  value is 2, Iron  $V$  value is 3. O(I)H was protonated on surface formed, the extra H contribute valance to oxygen, so Fe-O(I) bond became longer to keep oxygen valance sum constant. Meanwhile, Fe-

O(I) bond contributed less bond valance to Fe, so Fe-O(II) and Fe-O(III) were shorten to provide more bond valance to Fe. When water absorbed on surface, the hydrogen bond between O(II) with the absorbed water provided valance to O(II), in which case Fe-O(II) contribution needed to be smaller to keep valance sum for O(II), it leads an increase of Fe-O(II) bond length. At the same time, Fe-O(II) contributes less valance to Fe, which resulted a shorter Fe-O(I) bond which can provide more valance to keep Fe valance sum. O(III) was in the same chemical environment with O(II), so Fe-O(III) bond length change followed the same explanation.

We also noticed that the intense of change for Fe-O(I) and Fe-O(II) bond length were quite different. By absorbing water, Fe-O(I) was shorten by 6.3% , Fe-O(II) was increased only by 1.2%. In bond valance framework, this can be explained qualitatively by the equation format calculating the individual bond valance stated above.  $R_0$  was 1.765 for Fe, both Fe-O(I) and Fe-O(II) length were longer than  $R_0$ . Fe-O(I) was father away from  $R_i$ , according to the properties of exponential curve, to provide same magnitude change in bond valance, the change of  $R_i$  for Fe-O(I) should be larger than Fe-O(II).

#### 4.3.3 Two water molecules absorbed on surface

Two extra water molecules absorption model also had been built and investigated. Shown in Fig. 4.4, the first extra water molecule was determined to be absorbed in the same way with one water molecule absorption. Hydrogen bond 1 and 2 were formed. The second water molecules coordinated with the first water molecule by two hydrogen bonds (3 and 4). The O---H bond length for those four hydrogen bonds are 2.096 Å, 1.922 Å, 1.823 Å, 1.817 Å respectively. This two layers structure is in qualitatively agreement with experimental result (but not quantitatively, for example bond length Fe-O(I)).

#### 4.4 Goethite (100) – water interface

Different from ligands bonds in octahedron water shell structure of Fe(III) ion in water, surface Fe atom bonds with Oxygen and OH group with more valence components. Net +3 Charge disperses which indicates a weak bond with surface water. Ghose experimental work has shown O(I) has a Debye-Waller Factor 2.6(4) Å. O(L1) which has a DWF 4(1) Å in the first additional Layer bridges with surface oxygen atom with hydrogen bond. These two weak bonds result in ordered water layers which have been observed in our molecular dynamics simulation.

Strictly, the OH<sub>2</sub> group bonded with surface Fe should be defined as part of Surface. In our AIMD study, Fe- OH<sub>2</sub> bond was found broken and reformed frequently and water exchanges happened on surface. So we called “OH<sub>2</sub> groups” water molecules and being classified as type 1 water. (Fig. 4.3) The existence of water molecules which formed H-bond with oxygen atom on surface is observed in our AIMD trajectory, we classified that as type 2 water. All other water molecules in this simulation were classified as type 3 water. These three types of water molecules showed different properties, this can be regarded as an evidence of the ordered water structure on goethite surface. The detailed properties differences would be discussed in later section.

#### 4.4.1 Bonds in interface

Three bonds in the interfacial region played important roles in constructing ordered water structure, Fe-OH<sub>2</sub> bond, the H-bond connected type 2 water (donor) with surface oxygen (acceptor) which we called H-bond1, and H-bond connected type 1 water (donor) and type 2 water (acceptor) which we called H-bond2. Bond lengths, H-Bond angles information were listed in table 4.2. It is noteworthy that Fe-O had different value of bond length in different definitions. As discussed before, this bond was weak, if we changed bond cutoff from 2.8 Å to 3.2 Å, the average bond length would change from 2.306 Å to 2.400 Å. The peak position in g(r) of Fe(surface)-O(water) is 2.275 Å, in our viewpoint, this is reasonable definition of bond length. The average bond lengths for H-bond 1 and H-bond2 were 2.821 Å and 2.809 Å, the angles are



155.9° and 156.5°, these suggesting slightly stronger H-bond formation comparing to bulk water(2.83 Å).

Fe-O radial distribution function plotted in Fig. 4.5 was employed to investigate the water structure on surface. Here, only Fe atoms on surface were in consideration, Oxygen was defined as the oxygen atom in water molecules. Both Fe and O atom inside the crystal slab were not included. The first peak of Fe(surface)-O(water) was in the range of 2.0 Å - 2.8 Å for type 1 water on surface. The center of peak was 2.275 Å. This peak was occurred to Fe- OH<sub>2</sub> bond on surface. The second peak was in the range of 3.5 Å to 4.5 Å. There were two sources of water molecules for the second peak. The first source was type 2 water. Another was the water which was approaching or escaping from Fe atom when Fe-OH<sub>2</sub> surface bond was broken. Sometimes, the escaping water and approaching water co-existed at the same time for one site, which may involve a water exchange process or competing stage which would be discussed later in this paper.

We calculated the possibility of forming Fe- OH<sub>2</sub> for every surface Fe atom and H-bond 1 for every surface oxygen atom. The possibility for forming Fe- OH<sub>2</sub> bond for every Fe was 0.558 for if we set the cutoff length 2.8 Å, it increased to 0.552 if we relaxed the cutoff to 3.2 Å. The possibility of forming H-bond 1 is 0.591. (The criterion  $d(O-O) < 3.2\text{Å}$ , and angle  $OH...O > 135^\circ$ ). The conditional possibility for existence of Fe- OH<sub>2</sub> when type 2 water bonded to oxygen atom on surface which connected to this Fe is 0.834. This high possibility indicated type 2 water bonded to surface oxygen atom would help type 1 water bonded to Fe.

Fig. 4.6 tried to express the relations of H-bond 1 with Fe- OH<sub>2</sub> bond if Fe and type2 water coordinate with the same O on surface. We plotted the average H bond lengths and angles change with Fe- OH<sub>2</sub> bond length. It was found if Fe- OH<sub>2</sub> bond is longer, H-Bond 1 nearby was obviously weaker. When Fe- OH<sub>2</sub> is 2.10 Å, the average H bond is near 2.70 Å, 162.5°. If Fe- OH<sub>2</sub> is 2.50 Å, H-bond lengthened to 2.76 Å, the angle decreased to 156.0°. These changes were

noticeable. This agreed well with our expectation from Bond valance theory. When Fe- OH<sub>2</sub> is longer, it contribute less valance to Fe on surface, it leaded a shorter Fe-O(II) bond (Fig. 4.3) which would contributed more valance for both Fe (to keep valance sum)and O(II). Then O(II) needed less valance from H-bond1. That was the reason of weaker H bond 1.

#### 4.4.2 Three types of water molecules

As discussed in previous section, there are three types of water molecules in the computational cell. (Fig. 4.3) Wannier orbitals (Marzari et al., 2012)of spin up and spin down lone-pair electrons for Type 1 water has been plotted in Fig. 4.8(Bogatko et al., 2010). Compare to the spin up lone pair electron, it is clear that the wannier orbital for spin down lone pair electron has been attracted a lot to Fe ion on surface who has localized spin up moments. This is caused by spin localization of the d electrons in Fe site, the empty spin down d orbital hybrids with the oxygen lone-pair orbital so the spin down lone pair electron of oxygen moves toward Fe site.

From table 4.3, both the spin up and spin down electrons in oxygen from type 3 water show similar value of do-wfc and  $\Theta$  wfc-o-wfc with bulk water result. Those numbers for type 2 water are also very close to bulk water value. For type 1 water, do-wfc for spin down LPO has been lengthened by  $\sim 0.02$  Å which agrees with our analysis to Fig. H. do-wfc for spin up LPO hasn't been changed comparing to bulk water. A decrease of  $8^\circ$  and  $3.4^\circ$  has been observed for  $\Theta$  wfc-o-wfc spin down and spin up LPO, separately. The BOs have also been influenced by the polarization of LPO. It is found  $\Theta$  wfc-o-wfc for BO has been increased slightly and the do-wfc increased has been shorten.

Fig. 4.9 shows the electrons polarization which has been leads by the surface bonds. To visualize the difference before and after forming of those bonds, the spin electron density distribution of goethite (100) surface without Type1 and Type2 water has been calculated first.

Then we optimized the electron densities for type 1 and type2 water separately without the surface slab. After that, we calculate the electron density distribution of the whole interface which contains the surface and two types of water molecules, and then subtracts the separate surface electron density and water electron density. The result is plotted in Fig. 4.9. It is observed that the d orbital for minority spin in Fe site has a bit densities difference before and after interaction. Additionally, type I water show very evident spin polarization to the surface. Interestingly, O(II) atom which form H-bond with type 2 water also has spin density difference in lone pair orbital. The lone pair electrons in the direction of Fe-O(II) bond should be spin polarized due to the similar reason of lone pair electrons in type 1 water. But this spin polarization exists in both interface and pure surface calculation, so it's been canceled out and not shown in this picture. But this also leads a spin polarization of the other LPO for O(II) atom which is towards the type 2 water, and when this LPO interacts with empty H ion in type 2 water, the spin polarization has been “infected” to type 2 water (the closed-shell can be damaged) through the Hydrogen bond, this is the reason both type 2 water and O(II) atom have different spin electron density distributions before and after surface interaction .

By decomposing the total H-bond information in terms of acceptor bonds and donor bond originating from there types of water respectively, it is possible to identify the structure difference between different types, this can be used to characterize ordered water structure on surface. In Fig. 4.10, the O-O radial distribution functions for oxygen from different types of water molecular were plotted separately. Only one peak has been observed for all three types of water molecular. Peak is in the range of 2.5 Å to 3.2 Å which is consistent to H-bond O-O distance. The type3 curve shows the properties of bulk water considering the peak position and attitude. Type 3 water has the highest peak, while type 1 peak is the lowest. Basic bond information and H-bond condition were listed in table 4.1. Average Bond length and angles of water molecules were all close to bulk water. There were no differences between those three types. However, water

molecules showed difference in forming H-bond. Comparing to type 3 water, Type1 water had a smaller number of H-bonds as donor, had very small number of H-bonds as acceptor. Type2 water had a slight larger number of H-bond as donor, and a smaller number of H-bond and acceptor.

The difference can be explained by polarization and bonding condition of type 1 and type2 water. As shown in Fig. 4.7, type1 “faced” to the surface, Fe- OH<sub>2</sub> draw the electron density of oxygen. Then the ability of forming H-bond as acceptor has been intensely limited. Since type 1 and type2 water molecules connected with surface, there was only one direction they could “see” other water molecules. This could be responsible for the fact type1 water has slightly small number H-bond as donor and type2 water has slightly small number of H bond as acceptor. This also explained type 1 and type2 water molecules’ rdf curves were below type 3. Type 2 water had a large number of H-bond as donor. That was caused by our definition of type2 water which ruled type2 water bridged with surface O with H-bond as donor, this guaranteed each type2 water molecule had one H-bond as donor at least.

#### *The power spectrum of three types of water*

Power spectrums of three types of water molecules and OH (OD) group on surface could be calculated by taking fourier transform of the velocity autocorrelation functions, the velocity of hydrogen atoms are used. (Kohanoff, 1994; Thomas et al., 2013; Wang et al., 2014) The results are shown in Fig. 4.11.

$$P(\omega) = m \int \langle \dot{r}(\tau) \dot{r}(t + \tau) \rangle_{\tau} e^{-i\omega\tau} d\tau$$

The peaks located in the range from 0-800 ( $cm^{-1}$ ) for Fig. 4.11 are corresopnding to the intermolecular librational and translational motion which are hard to interperet. The peaks located in the range from 1000-1300 ( $cm^{-1}$ ) are the contribution of bending motion mode of water

molecule, so this peak does not exist in the spectrum of OD group on the surface. This peak for bulk water (type 3) is  $1200\text{ (cm}^{-1}\text{)}$  which agrees with experimental value  $1209\text{ (cm}^{-1}\text{)}$  in liquid water (Huang et al., 2014b). Bending peak for type 1 water is redshifted to  $1168\text{ (cm}^{-1}\text{)}$ , and this peak has been split to two peaks  $1102\text{ (cm}^{-1}\text{)}$  and  $1241\text{ (cm}^{-1}\text{)}$  for type 2 water. The peaks in the range from  $1800\text{--}2500\text{ (cm}^{-1}\text{)}$  are from stretching motion modes. This peak for bulk water (type 3) is  $2220\text{ (cm}^{-1}\text{)}$  which is slightly smaller than experimental value  $2260\text{ (cm}^{-1}\text{)}$ . This peak is blueshifted to  $2320\text{ (cm}^{-1}\text{)}$  for type 1 water and  $2350\text{ (cm}^{-1}\text{)}$  for type 2 water. This may indicate water molecules in interfacial region have stronger hydrogen bonds comparing to bulk water. OD group have three peaks from stretching motions, one is  $2210\text{ (cm}^{-1}\text{)}$  and other two are around  $2340\text{ (cm}^{-1}\text{)}$ .

The surface attraction is weak comparing to highly charged bare ion. Water molecules bonded with Fe and oxygen on surface formed ordered water layers on goethite surface. We don't observe very clear second additional water layer which proposed in experimental work. This can be caused by different reasons. One important aspect in our study is the interface which includes a lot of free waters while the experiments were taken in Ar environment with only few water layers absorbed. The kinetic energy and attractions between water molecules could damage the second layer structure. This is the reason why we get similar extra two water layers structure in plane-wave optimization but not in this AIMD simulation.

#### 4.4.3 Dynamical process on the interface

##### *Water exchange:*

In our total 15 ps simulation (including 1.5 ps equilibrium time), no proton transfer had been observed. 4 exchanges with bulk water molecules happen to the Fe-OH<sub>2</sub> on surface while there are 12 surface Fe atoms in total. So the estimated exchange rate for one Fe-OH<sub>2</sub> bond on surface is 0.025 times/ps although there were not enough exchanges to get accurate rate. The

ligand exchange mechanism has been widely studied for ion in solutions systems (Bylaska et al., 2007). Two main reaction mechanisms can be summarized as dissociative (which begins with a water leaving water shell first, analogous to  $S_N2$  reactions) and associative (which begins with a water entering the water shell, analogous to  $S_N1$  reactions) mechanism. In our observation, the exchange of surface water mechanism is analogous to dissociative mechanism. The process can be described as Fe-  $OH_2$  bond on the surface breaks first, then bulk water approaches to Fe atom on surface. Different from water exchanges happens in the first water shell of ion, surface water exchange process takes longer time from the initial configuration to final configuration. In Fig. 4.12, starting from 4ps, Fe11- O11 bond becomes unstable, then from 5.5ps -6.5ps, O28 approaches to Fe11 and O11 escapes in a slow velocity. After 6.5ps, O28 bonded to Fe11 and O11 escaped. This exchange process takes 2.5 ps totally.

*Competing stage when Fe-  $OH_2$  bond broke:*

Except water exchange, there was another interesting process we observed from our AIMD simulation involved surface bond broke. When Fe didn't have bonded water, there was competing stages sometimes for free water molecules to become bonded. In Fig. 4.13, from 1.5ps to 4ps, O38 and O12 were competing to be bonded to Fe. In the time range of 4ps to 6.5 ps, O38 was bonded. After that, another water (O28) molecule approached to the surface. Then, Fe-O38 bond broke, O38 and O28 were competing again. This competing stage can last as long as 4 ps which was still on at the end of this simulation. When water molecules were in this stage, the distance to Fe was around 3.5 Å to 4.5 Å, so we concluded this might be one reason for the second peak in  $g(r)$  for Fe-O. (Fig. 4.5)

#### 4.5 Conclusion:

First principle study of goethite (100) water interface has been reported. Plane-wave optimization simulations have been used to investigate absorption of water molecules on goethite surface. 16ps AIMD simulation which contained a (3\*2) surface slab and 65 water molecules (near 1g/cm<sup>3</sup>) have been performed, this simulation carried out at temperature near 300 K. This AIMD calculation was extremely demanding due to a very large model was needed to describe the chemical events in the interface.

Plane-wave optimization simulations predict the goethite (100) surface termination, surface site attracts water molecules and a two additional water layers structure which comparable to experimental result. After analysis bonding condition and of different types of water from AIMD simulation, we find water molecules which coordinated with surface Fe are oriented to surface, water molecules coordinated with surface oxygen also polarized due to H-bond, there two types of water molecules form ordered water layers on surface. Fe- OH<sub>2</sub> ligand bond and H-bond on surface are not as strong as ligand bonds between highly charged ion with first shell water molecules. Water exchanges process last in a relatively long time period. And a special process in which two water competed to be bonded on surface has been observed in this simulation.

Table 4.1: Calculated parameters defined in figure 4.3 (the right column data is from AIMD, other three are from DFT optimization) (length unit: Å, angle unit: °)

	Structure Parameters	Dry surface (hydrated)	One additional water	Two additional waters	AIMD
Fe-O bond on surface	R <sub>Fe-O(I)</sub>	2.486	2.330	2.377	2.399(cutoff 2.8) 2.307(cutoff 2.5) 2.275(from rdf.)
	$\sigma$ <sub>Fe-O(I)</sub>				0.18(cutoff 2.8) 0.11(cutoff 2.5)
	R <sub>Fe-O(II)</sub>	2.073	2.098	2.099	2.094
	$\sigma$ <sub>Fe-O(II)</sub>				0.094
	R <sub>Fe-O(III)</sub>	2.072	2.111	2.105	2.105
	$\sigma$ <sub>Fe-O(III)</sub>				0.099
	$\angle$ O(I)-Fe-O(II)	87.10	82.91	80.64	81.06
	$\sigma$ $\angle$ O(I)-Fe-O(II)				6.73
	$\angle$ O(I)-Fe-O(III)	78.44	81.67	81.94	79.29
	$\sigma$ $\angle$ O(I)-Fe-O(III)				6.86
	$\angle$ O(II)-Fe-O(III)	92.32	90.94	91.43	93.98
	$\sigma$ $\angle$ O(II)-Fe-O(III)				5.26
Type 1 water	R <sub>O(I)-H</sub>	0.958	0.961	0.959	0.965
	$\sigma$ <sub>O(I)-H</sub>				0.0204
	$\angle$ H-O(I)-H	104.39	105.00	105.59	106.00
	$\sigma$ $\angle$ H-O(I)-H				4.93
Type 2 water	R <sub>O(A)-H</sub>		0.961	0.964	0.967
	$\sigma$ <sub>O(A)-H</sub>				0.197
	$\angle$ H-O(A)-H		103.61	105.63	106.12
	$\sigma$ $\angle$ H-O(A)-H				4.72
Type 3 water	R <sub>O(B)-H</sub>			0.962	0.965
	$\sigma$ <sub>O(B)-H</sub>				0.190
	$\angle$ H-O(B)-H			104.7	105.53
	$\sigma$ $\angle$ H-O(B)-H				4.22
Hydrogen bond 1	R <sub>O(II)-O(A)</sub>		2.775	2.895	2.789
	$\sigma$ <sub>O(II)-O(A)</sub>				0.178
	$\angle$ O(II)-H-O(A)		161.28	140.00	155.59
	$\sigma$ $\angle$ O(II)-H-O(A)				11.20
Hydrogen bond 2	R <sub>O(I)-O(A)</sub>		2.775	2.878	2.814
	$\sigma$ <sub>O(I)-O(A)</sub>				0.176
	$\angle$ O(I)-H-O(A)		159.77	173.92	154.20
	$\sigma$ $\angle$ O(I)-H-O(A)				10.85
Other Hydrogen Bonds				2.790	2.799
				174.37	159.5



Table 4.2: Hydrogen bonds for 3 types of water molecules  
(length unit: Å, angle unit: °)

	Water I	Water II	Water III	Bulk water
O-H length	0.965	0.967	0.965	0.97
Deviation	0.02	0.02	0.02	0.03
H-O-H angle	106.08	106.06	105.56	105.45
Deviation	4.93	4.72	4.22	5.19
As donor				
Ave. number	1.553	1.771	1.723	
Ave. O-O length	2.809	2.801	2.799	
Ave. H-O-H angles	156.08	158.31	159.51	
As acceptor				
Ave. number	0.354	1.637	1.735	
Ave. O-O length	2.839	2.807	2.799	
Ave. H-O-H angles	155.70	159.18	159.50	

Table 4.3: Wannier orbital center analysis for 3 types of water molecules  
(d<sub>o-wfc</sub> unit: Å, Θ<sub>wfc-o-wfc</sub> unit: °)

	Type 1 water				Type 2 water				Type 3 water			
	do-wfc		Θ wfc-o-wfc		do-wfc		Θ wfc-o-wfc		do-wfc		Θ wfc-o-wfc	
	BO	LPO	BO	LPO	BO	LPO	BO	LPO	BO	LPO	BO	LPO
Interface water α	0.493	0.332	104.0	115.6	0.496	0.326	102.6	119.3	0.496	0.327	103.3	118.4
Interface water β	0.492	0.352	105.0	111.0	0.496	0.326	102.6	119.2	0.496	0.327	103.3	118.4
	First hydration shell				Second hydration shell				Bulk			
	do-wfc		Θ wfc-o-wfc		do-wfc		Θ wfc-o-wfc		do-wfc		Θ wfc-o-wfc	
	BO	LPO	BO	LPO	BO	LPO	BO	LPO	BO	LPO	BO	LPO
Fe3+64 water α	0.48	0.32	106	112	0.50	0.33	104	118	0.50	0.33	103	119
Fe3+64 water β	0.48	0.38	110	92	0.50	0.33	104	118	0.50	0.33	103	119
Al3+-64water	0.48	0.34	106	110	0.50	0.33	103	117	0.50	0.32	103	119
64H <sub>2</sub> O									0.50	0.33	106	115

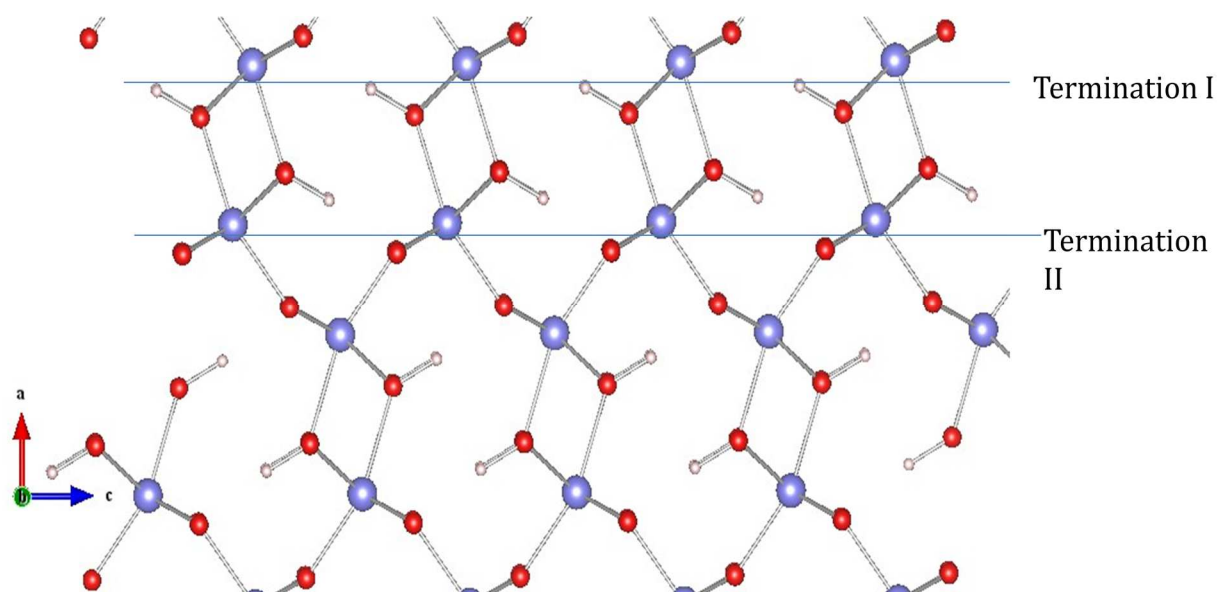


Figure 4.1: Bulk structure and two types of (100) surface terminations of goethite

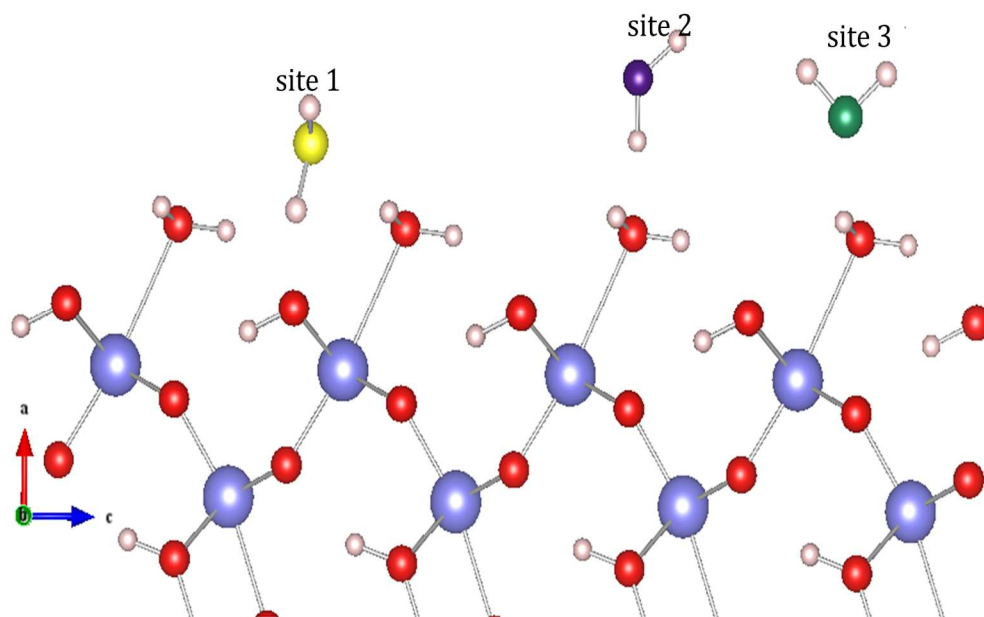


Figure 4.2: Site choices of one water molecule adsorption on goethite (100) surface

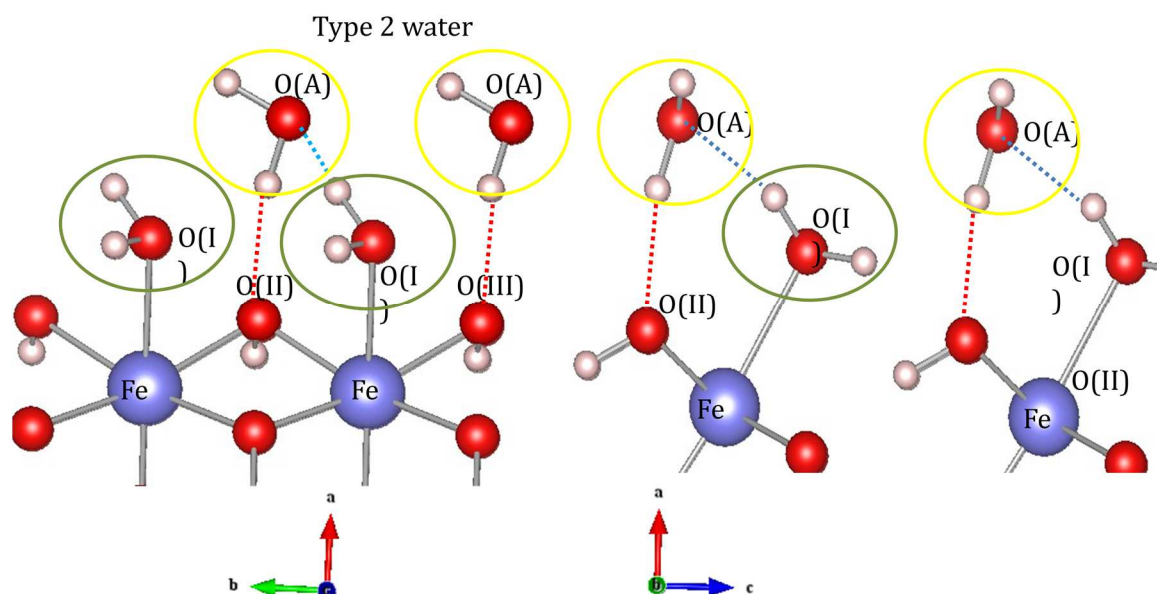


Figure 4.3: Two side-views of different types of H-bonds and water molecules goethite (100) aqueous interface

Type 1 water: green cycle, H<sub>2</sub>O(I)

Type 2 water: yellow cycle, H<sub>2</sub>O(A)

Type 3 water: other water in simulation

H-bond1: O(A)-H-O(II)

H-bond2: O(I)-H-O(A)

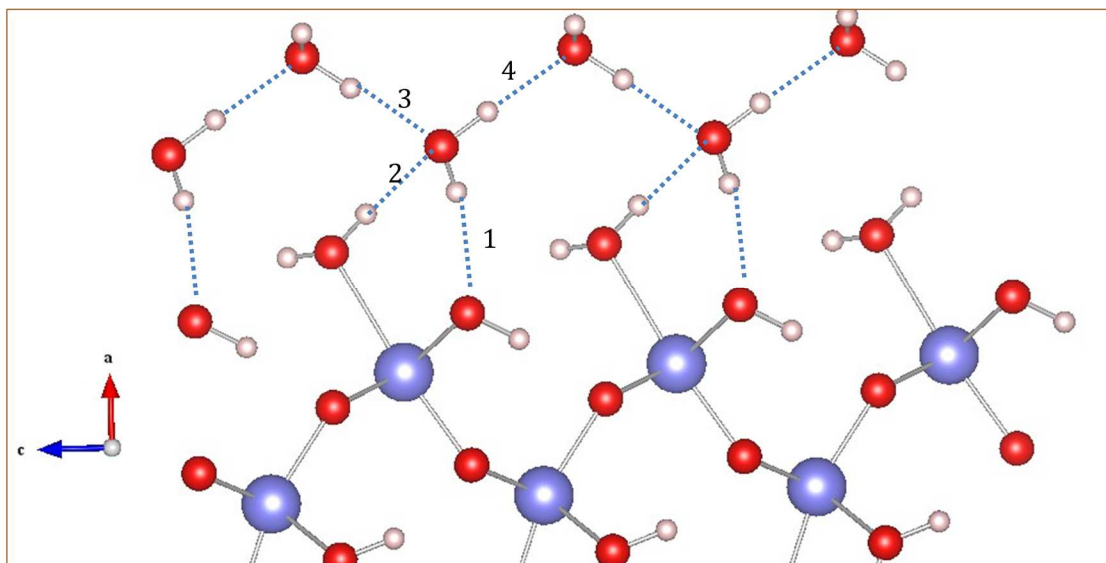


Figure 4.4: Surface bonds and Hydrogen bonds of two additional water layers absorbed on goethite (100) surface

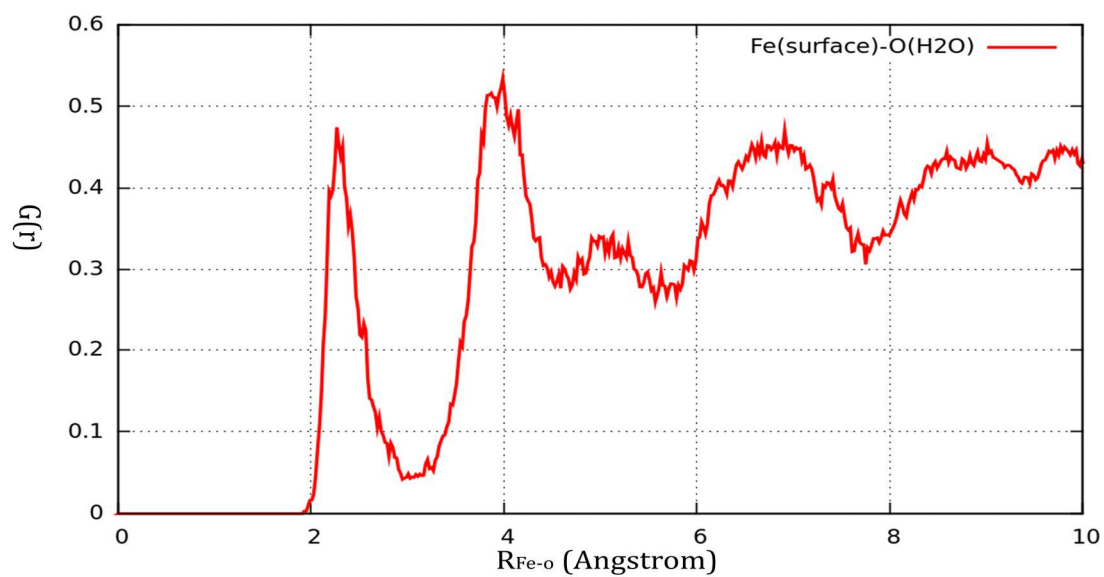


Figure 4.5: Radial distribution function of Fe-O on goethite (100) surface. (Fe: surface Fe atom  
O: oxygen atom from water)

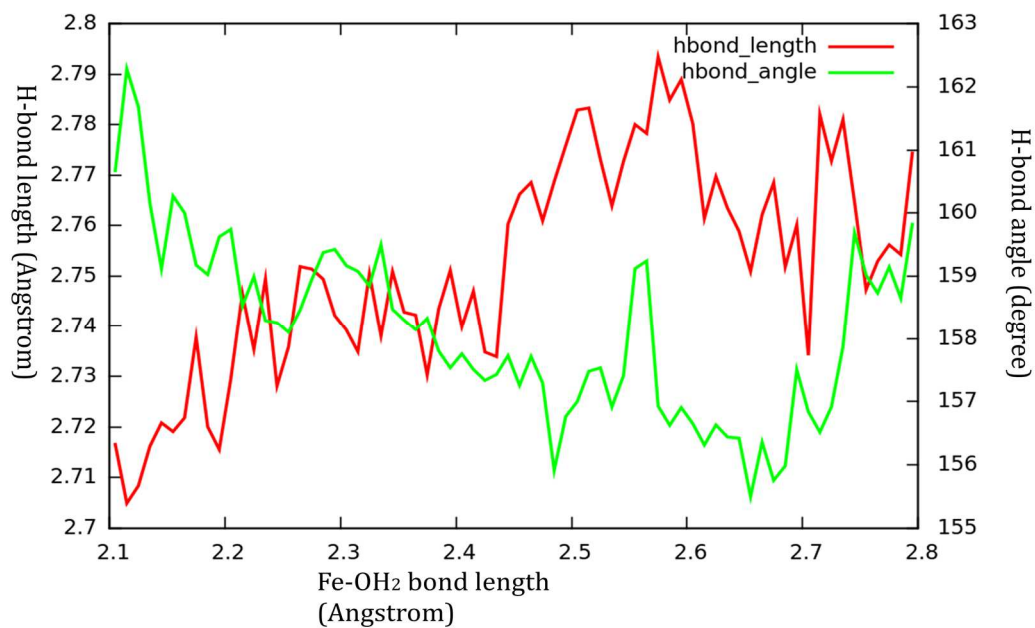


Figure 4.6: Correlation of surface Fe-OH<sub>2</sub> bond length with Hbond1 (bond length and angle) on goethite (100) surface

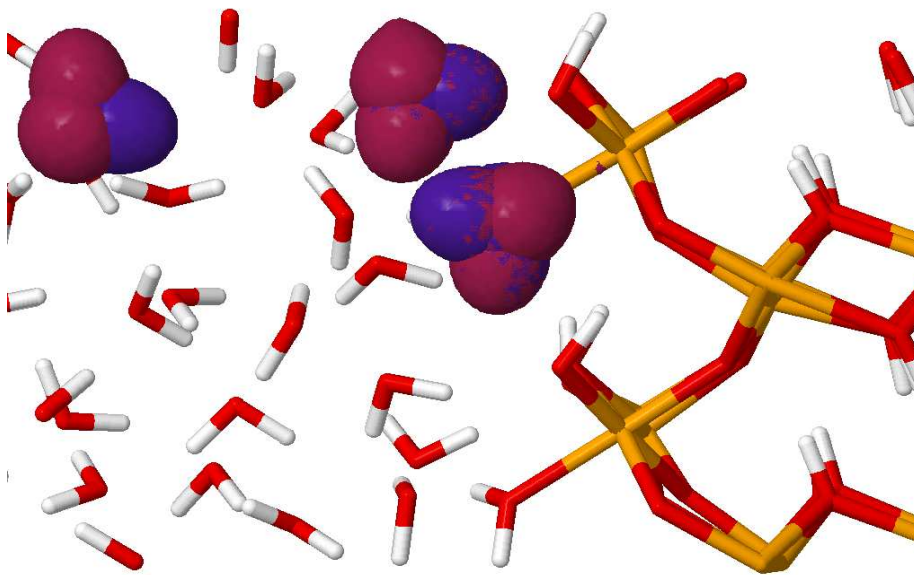


Figure 4.7: (Color) The localized wannier orbitals of three types of water

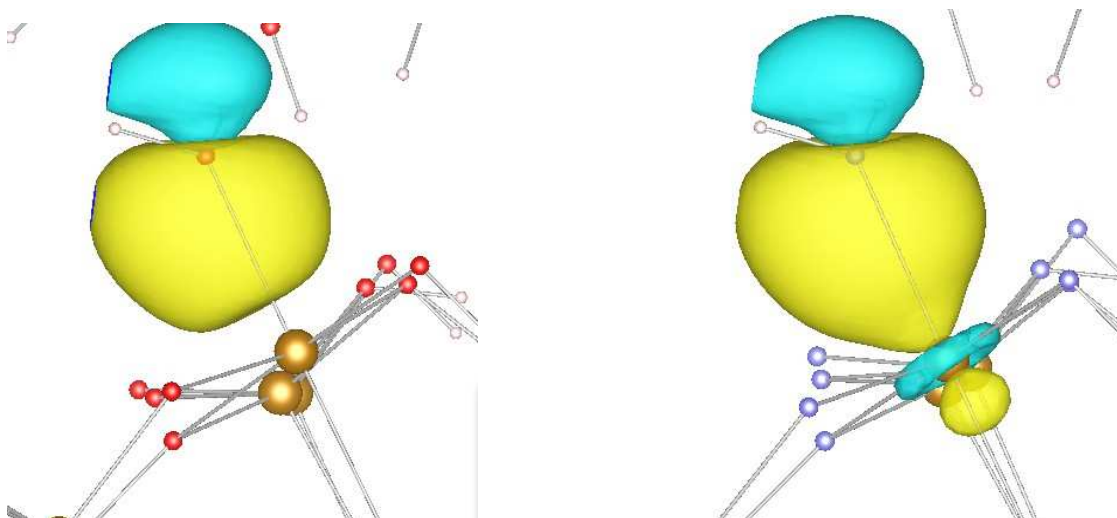


Figure 4.8: Wannier orbitals for spin up (left) and spin down (right) lone-pair electron of oxygen atom in water molecule bonded to Fe on surface

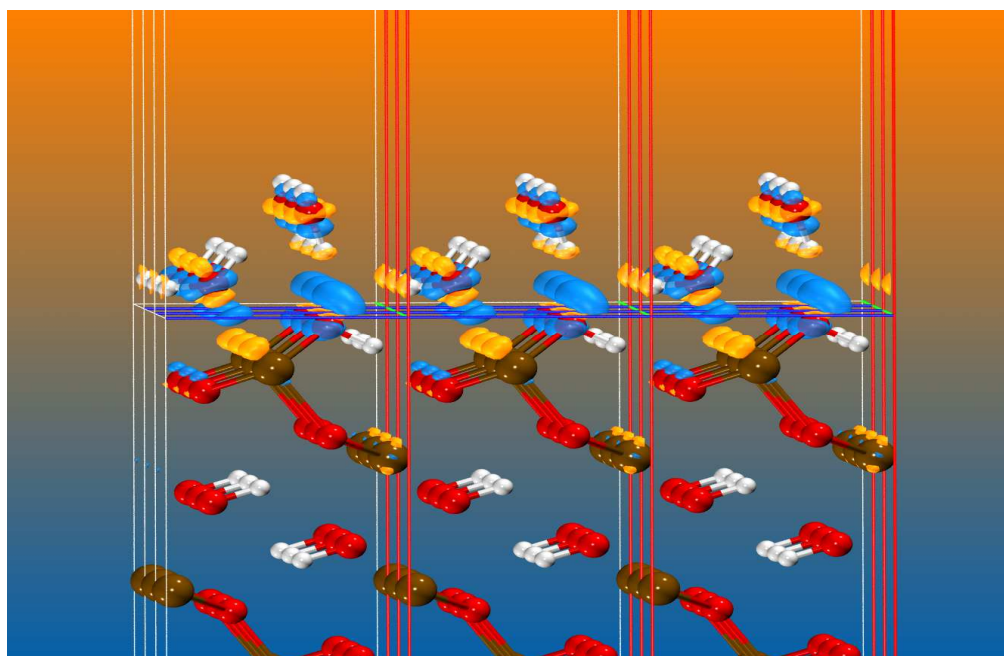


Figure 4.9: Electron density difference before and after water layers absorption on goethite (100) surface

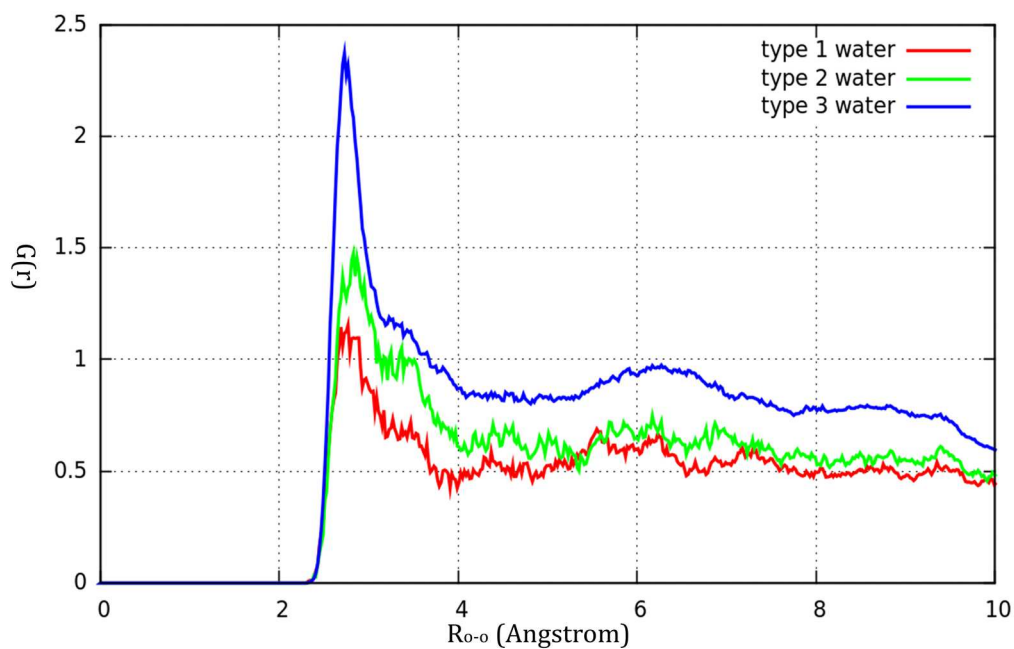


Figure 4.10: O-O radial distribution functions for oxygen atom (first O in O-O) from different types of waters.

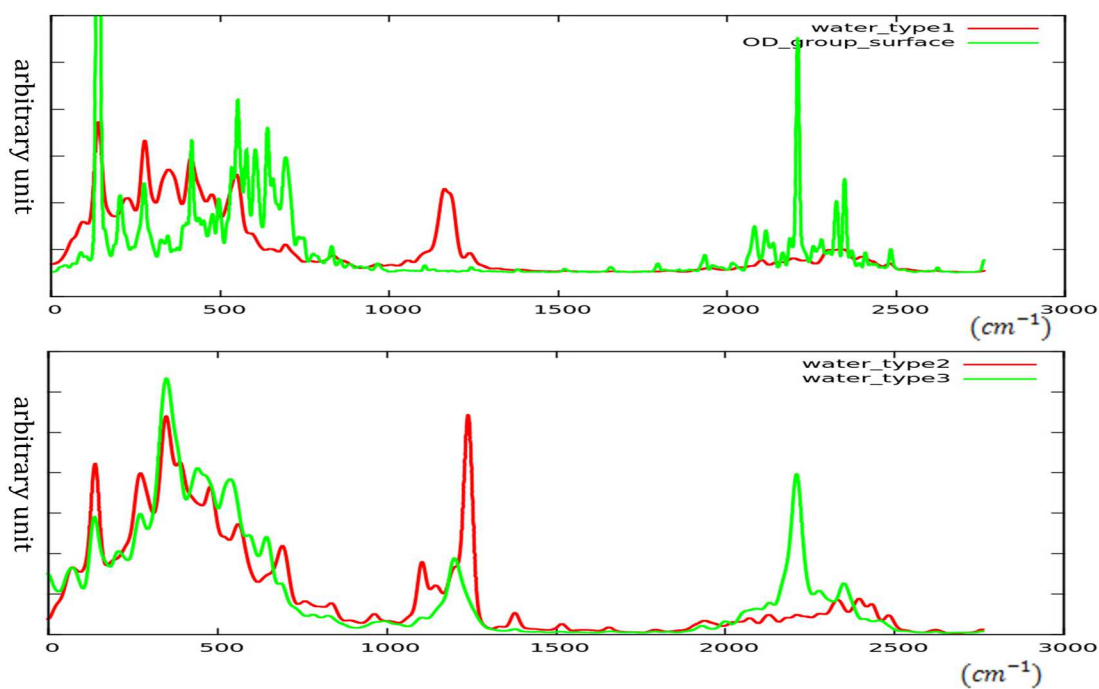


Figure 4.11: Power spectrums of different types of water molecules and OD group on surface



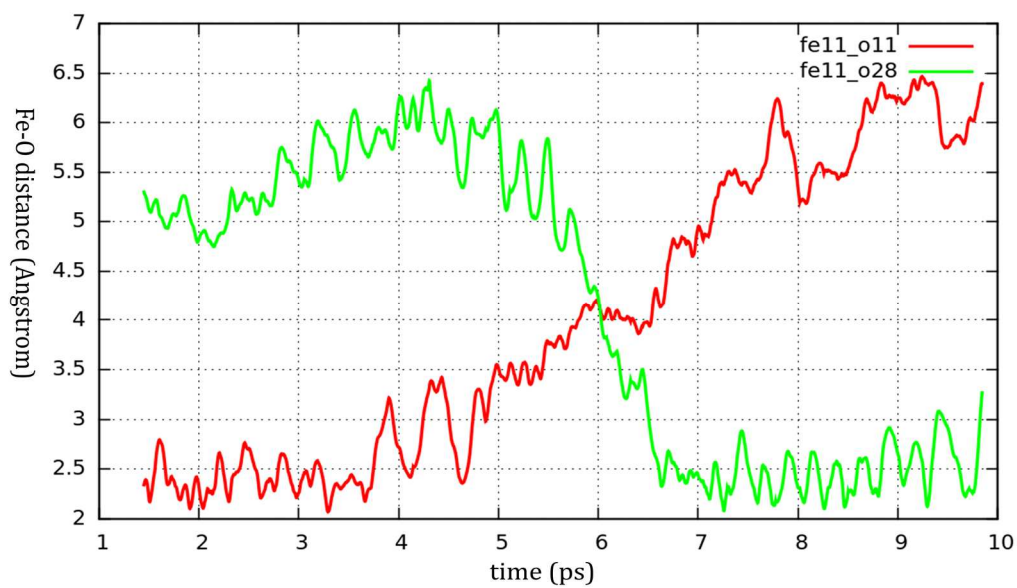


Figure 4.12: Exchange of Fe bonded water molecule on goethite (100) surface with bulk water

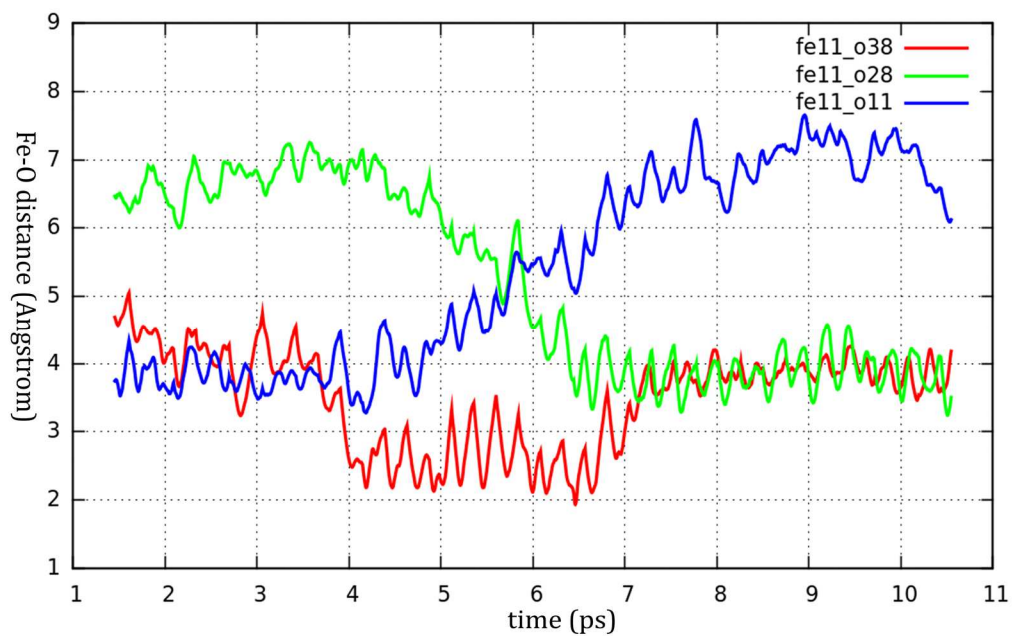


Figure 4.13: The stage of water molecules competing to be bonded on surface



## 5 STUDY OF HEMATITE (001) AND (012) SURFACES, AQUEOUS INTERFACES AND FE(II) ION ABSORPTION IN INTERFACES

### 5.1 Introduction

As one abundant and important mineral in the Earth, the interfaces of  $\alpha$ -Fe<sub>2</sub>O<sub>3</sub> (hematite) (Cornell, 2003) and aqueous solutions where many important geochemical, biological (Kappler and Newman, 2004; Roden, 2006; Stumm and Sulzberger, 1992; Weber et al., 2006) and environmental reactions occur are of great interest. The knowledge of atomic-level surface, layered water structures and ion adsorptions on the hematite-water interface is essential and fundamental information for understanding those reactions. (Brown et al., 1998)

(001) and (012) surfaces are two most dominant growth surfaces in hematite nature crystals. (Condon et al., 1998) The hematite-water interfaces for those two surfaces have been extensively studied. In recent years, X-ray scattering is the widely used technique to these interfaces, scattering theory and fitting techniques are used to create atomic structure models. (Fenter and Sturchio, 2004; Liu et al., 1998) Calculated scattering intensity can be compared with the data from X-ray reflectivity and crystal truncation rod (CTR) in which way better model can be chosen and optimized. Various studies have been done including layers water structures on hematite (001) (Catalano, 2011; Tanwar et al., 2009; Trainor et al., 2004), Fe(II) ion adsorption on hematite (001) (Catalano et al., 2010a; Tanwar et al., 2008, 2009), water structures on hematite (012) (Catalano et al., 2007; Tanwar et al., 2007), Fe(II) adsorption on hematite (012) (Catalano et al., 2010a; Tanwar et al., 2008, 2009). Other than structure measurement, the electron transfer on hematite surface and bulk mechanism has also been studied (Kerisit and Rosso, 2006; Yanina and Rosso, 2008).

Different from modeling analysis in experiments, simulation can be useful in fully understanding the interface structure by providing direct information. Computationally, plane

wave density functional theory based methods has been used in studying hematite surfaces atomic structure, adsorption (Cr(VI) complex and electronic structure. (Liao et al., 2012; Rohrbach et al., 2004; Yin and Ellis, 2008, 2009; Yin et al., 2007) These structures calculations are normally searching structures at 0K in a very limited phase space, the optimization only provide one promising structure which is highly depends on initial structures. Ab-initio thermodynamics (Lo et al., 2007) has been taken into account which considers more structure candidates and temperature influence on simulation, it calculates the free energies of the different hematite surfaces in chemical equilibrium in a function of temperature and pressure. However it's still a static searching algorithm. Recently, classical Molecular Dynamics (MD) is used to hematite-water interface, and it shows advantage in revealing the dynamics of the system which is a powerful way in molecular modeling (Jones et al., 2000; Kerisit, 2011; Kerisit and Rosso, 2006). Although classical MD is computationally cheap and it allows us to calculate very big system (~1000 atoms), its potential models of atoms are usually very sensitive to systems. They are normally two or three bodies potential which have transferring difficulties even for similar conditions, especially for transition metal oxides (.ie. hematite) in which many body effect play an important role.

In this work, Ab-initio MD is used to simulate the hematite –water interfaces process. All the potentials and forces used here are calculated directly from Schrodinger equation using DFT+U methods which will be discussed later. The limit of Ab-initio MD is it's very time and cpu consuming for big systems. But as the development of supercomputers and parallel algorithms for Ab-initio methods, molecule modeling by ab-initio MD becomes plausible. In this paper, the simulated systems include ~300 atoms, ~1000 electrons. Four ab-initio MD simulations have been taken, hydrated “oxygen-terminated” hematite –water interfaces for (001) and (012) surfaces (Fig. 5.1) respectively, and also one extra ferrous ion absorbed on those

surfaces in aqueous solutions. Structures analysis of water layers on surfaces and ion adsorption on surface is based on trajectories from the four simulations.

Meanwhile, we also investigate the electronic structures for Fe(II) ion adsorption on hematite surfaces in aqueous solutions. This is a difficult electronic structure problem since their properties are heavily dependent on the properties of the strongly localized d electrons, complex hydration processes, disorder of the surface/solution interface, the interaction of the solution phase with the highly charged mineral surface, etc. To some extent, our study will build direct understanding to some structure properties and also electron transfer process which may happen on the interfaces.

## 5.2 Computational methods and computational cells

### 5.2.1 Computational methods

Plane wave calculation using density functional theory (DFT) has been used widely in predicting the structure properties mineral bulk and mineral surface. Those works provide good understandings to the lattice parameters, clean surface models, water layer structures and ion adsorptions. It is well known that DFT can't completely cancel out the orbital self interaction energy which sometimes can introduce very big error, especially to materials which contain localized electrons (.ie. d electron in transition metals). On-site column repulsion between the localized electrons in different spins plays an important role in materials. Shown in the chapter 3 table, for bulk hematite, the band gap and local magnetic moments calculating from pure GGA (DFT) have huge difference from experiments.

In Hartree-Fock (HF) approximation, the orbital self interaction energy has been canceled out completely by calculating exact exchange energy, but HF approximation always overestimates the band gap for materials. In practice, hybrid functional which combines exact exchange and DFT functional (Bylaska et al., 2011) has been proven to be a good way to describe

the electronic structure of transition metal oxides. However, this method is extremely expensive in computation. For the big scale mineral water interface simulation in this work (~1000 electrons, ~300 atoms), DFT+U (Dudarev et al., 1998; Rohrbach et al., 2004; Rollmann et al., 2004; Shick et al., 1999; Wang et al., 2006) includes the correlation effect approximately, also doesn't increase the computation work too much comparing to DFT. Proven in chapter 3, for hematite the results of band gap and local magnetic moment from DFT+U calculation are very close to the results from hybrid functional in accuracy. In DFT+U method, the d and f electron correlations are added by calculating Hubbard term approximately. Then a double counting term which describes those correlations in DFT needs to be deduced.

The system was propagated in time using Car-Parrinello Molecular dynamics (CPMD) (Car and Parrinello, 1985b) scheme. In CPMD framework, two terms have been added separately in two motion equations due to the added U term. In this work, U and J are set to be 4 eV and 1 eV (Rollmann et al., 2004) respectively which has been widely accepted and proven to be the most appropriate constant values for Fe in hematite. PBE96 (GGA) exchange correlation functional is also employed. A Teter's style norm-conserving pseudopotential (Teter, 1993) with semi core was used to Fe atom in which 3s and 3p are included as core electrons and softened Hamann pseudopotentials (Hamann, 1989) were used to oxygen and hydrogen atoms. Plane wave energy cutoff 50 Hartree for the wavefunction and 100 Hartree for the density were used. Equation of motions in CPMD were integrated using Verlet algorithm, with a time step 0.12 fs and fictitious orbital mass 600.0 au. All hydrogen atoms have been replaced by deuterium to facilitate the integration. The canonical ensemble was chosen for this simulation, Nose-Hoover thermostat was used to control the temperature for ions (300 K) and electrons (1200 K). CPMD simulations have been performed 15 ps for each system, 1 ps equilibration was performed after which trajectory has been collected. All the calculations are performed with NWChem package.

### 5.2.2 Computational cells structural details

The 30-atom hexagonal representation of the hematite unit cell has been studied in previous work. Here we use lattice constant  $a = b = 5.04 \text{ \AA}$ ,  $c = 13.86 \text{ \AA}$ . To create surface (001) surface slab, we expand the cell in  $a$  and  $b$  direction which made a (2\*2) surface ( $a = b = 10.08 \text{ \AA}$ ). Previous studies have shown the uppermost hematite (001) surface termination is “O-termination”. Our “O-termination” (001) surface slab contains 8 Fe layers which can be represented by O3-Fe-Fe-O3-Fe-Fe-O3-Fe-Fe-O3-Fe-Fe-O3 (Catalano, 2011). The hydration of O-termination (001) surface has also been investigated (de Leeuw and Cooper, 2007). Each surface oxygen which is doubly bonded to Fe atoms has been hydrated form a hydroxyl group. These hydroxyl groups are regarded located in its former oxygen vacancies. We expand the cell in  $c$  direction ( $c = 24.27 \text{ \AA}$ ) between two surfaces in the slab, and add 42 water molecules whose density is  $1.0 \text{ g/cm}^3$ . The total simulated cell is electrically neutral which has 976 valance electrons and 242 atoms which include 32 Fe, 102 Oxygen and 108 H.

To create (012) surface slab, we use Euler transformation to get the new cell which has lattice parameters as  $a' = 5.006 \text{ \AA}$ ,  $b' = 5.448 \text{ \AA}$ ,  $c' = 7.399 \text{ \AA}$ ,  $a = 83.4^\circ$ ,  $b = c = 90^\circ$ . To better simulate the dynamics on the surface, we expand the cell in  $a'$  and  $b'$  directions which made a 2\*2 surface. ( $a' = 10.012 \text{ \AA}$ ,  $b' = 10.896 \text{ \AA}$ ). Surface diffraction of hematite (012) surface show this surface differs from an ideal stoichiometric termination due to the vacancies of the near surface bulk Fe sites. The Ab-initio thermodynamics study also predicts this type of termination is most stable. We include 4 Fe layers in our slab, which can be represented by O2-X-O2-Fe2-O2-Fe2-O2-O2-Fe2-O2-Fe2-O2-X-O2 in  $c$  axis. In this surface model, there are two types of surface oxygen, O1 and O2. Similar to Yin's work (Yin and Ellis, 2009), each surface oxygen has been hydrated which leads a singly boned hydroxyl (Fe-O-H) and a triply coordinated hydroxyl (O3-H). This protonation model has been proven in the section 5.3. Between two surfaces of the slab in the cell, we add 54 water molecules ( $c = 25.0 \text{ \AA}$ ), and the density of water is set to  $1.0 \text{ g/cm}^3$ .

The total simulated cell is electrically neutral, it has 1104 valance electrons and 290 atoms which include 32 Fe, 118 Oxygen and 140 Hydrogen.

### 5.2.3 Spin configurations of surface slabs

Hematite is antiferromagenetic in room temperature and pressure, each Fe<sup>3+</sup>ion in hematite is a high-spin d<sup>5</sup> center which we can be found from experimental local magnetic moment. To investigate the ground magnetic states for the surface slabs we create, different magnetic states were considered and their energies are computed. For (012) surface, the energies for system in three antiferromagnetic states (AF +--+ , AF ++--, AF +---) and one ferromagnetic state (FM +++) have been calculated. AF+--+ is found to be most stable state. For (001) surface, four antiferromagnetic states (AF+++++--, AF++----+, AF+--+---+, AF+--+--+ ) and one ferromagnetic state (FM++++++) are taken into account. AF+++++--is the ground magnetic state. The energies differences are shown in the table 5.1. The ground magnetic states for both (001) and (012) surfaces are in consistent with magnetic ordering in bulk hematite which shows AF +---+ both along [001] and [111] with opposing magnetic moments places on Fe-Fe centers separated by short length. This agreement is expected since bonding conditions and chemical environments for Fe atoms in the surface slab haven't been changed too much comparing to bulk hematite (Rollmann et al., 2004).

## 5.3 The (012) protonation and water absorption of cleaved Surfaces

### 5.3.1 Hematite (012) surface protonation models

The protonation (termination) of the bonds on the surfaces that become unsaturated on cleavage is an important part of surface chemical environment which can affect both the local electronic structure and the structure of the absorbed water layers structure. In O-O-Fe-O-Fe-O-O-Fe-R cleavage of hematite (012) surface, there are two possible hydrated models which lead to

a neutral surface, (OH)-(OH)-Fe-O-Fe-O-O-Fe-R (Yin and Ellis, 2009) and (OH<sub>2</sub>)-O-Fe-O-Fe-O-O-R. In both models, there are two types of oxygen sites including singly Fe-coordinated Oxygen and triply Fe-coordinated Oxygen. Triply Fe-coordinated Oxygen ( $O^{II}$ ) is more into the slab than Singly Fe-coordinated Oxygen ( $O^I$ ) which is on the top of surface. (Fig.5.2. A) Oxygen atoms are quadruply bonded to Fe atoms in bulk.

Following Ab-initio Thermodynamis approach, to determine the best protonation model, we optimized the structures of these two (2\*2) hydrated surface models using DFT+U method. The Hydrated model (OH)-(OH)-Fe-O-Fe-O-O-Fe-R (model 1 in Fig. 5.2 A and B) is found to be 11.7 meV/ Å<sup>2</sup> lower in surface energy than the other model. In this hydrated model, ( $O^I$ ) and ( $O^{II}$ ) are both hydrated forming two OH groups. After structural optimization, ( $O^{II}H$ ) group bridges to ( $O^IH$ ) group forming a hydrogen bond (2.73 Å, 154.6°) (Fig. 5.2.A, H-bond 1) This Hydrogen bond reduces the bond valence of ( $O^{II}$ ) which might be over-saturated. From another aspect, it also contributes bond valence to ( $O^I$ ) oxygen considering possible under-saturation situation of ( $O^I$ ) which is only singly Fe-coordinated. Hence, this Hydrogen bond stabilizes the surface configuration effectively.

### 5.3.2 Water absorption on hematite (012) cleaved surface

Caused by cleavage and protonation, atoms on surface region are normally over-saturated or under-saturated. This is an important reason water molecules absorbed on surface. Hydrogen bonds which bridge water molecules to surface layers and Hydrogen bonds between surface atoms can stabilize the surface region. They also play significant roles in determining the water structure on surface. Recently major advances have been made in the observation of water layer structures on the surface region using synchrotron generated X ray diffraction. Ghose (Ghose et al., 2010) employed crystal truncation rod (CTR) techniques to study three dimensional structural of water layers on goethite (100) surface. Tanwar (Tanwar et al., 2007) also used this techniques

to investigate water adsorption on hematite (012) surface. These works proposed many structural models which can help us understanding the interfacial structure.

In computational side, single or several water molecules adsorptions process can be investigated by structural optimization tool employing Ab-initio (DFT or DFT+U) methods. Kubicki (Kubicki et al., 2008) studied water layers structure on goethite (100) surface. Lo (Lo et al., 2007) concluded the surface water can stabilize surface structure by hydrogen bonding when studying water adsorption on hematite (012) surface.

As starting point for adsorption optimizations of the interface structure on hematite, we studied the single water adsorption process on the protonated hematite (012) surface by placing one water molecule in contact with the (2\*2) surface of the optimized models (model 1 and model 2 in section IV.1 respectively, Fig. 5.2). The adsorption energy for one water molecule on both protonated models can be calculated as:

$$E_{adsorption} = E_{water} + E_{surface} - E_{water-surface}$$

The water adsorption energy for model 1 is 6.70 Kcal/mol which is slightly greater than the adsorption energy 5.53 Kcal/mol for model 2. In model 1, the absorbed water forms a hydrogen bond with an ( $O^I$ ) atom as a donor (2.71 Å, 160.4°, H-bond A in Fig 5.2. B) and a Hydrogen bond with another ( $O^I$ ) atom as an acceptor (2.70 Å, 168.9°, H-bond B in Fig 5.2. B). In model 2, the ( $O^{II}$ ) might be under-saturated. The absorbed water forms a hydrogen bond with ( $O^{II}$ ) as donor. (2.90 Å, 166.0°, H-bond b in Fig. 5.2 C) It also forms a hydrogen bond with an ( $O^I$ ) atom as acceptor. (2.75 Å, 146.4°, H-bond a Fig 5.2 C) The side views of water adsorption, hydrated models and hydrogen bonds are shown in Fig. 5.2.

Combining the result from surface protonation section, for those two hydrated charge neutral surface models, Model 1 has been shown better energetically, it also has slightly greater water adsorption energy when one water molecule absorbed on the (2\*2) surface. However, the



energy gap between Model 1 and Model 2 is small, so the co-existence of Model 1 and Model 2 is possible. In Catalano's experimental work to this surface (Catalano et al., 2007), a closer water layer which is regarded forming hydrogen bonds with ( $O^{II}$ ) atoms has been observed which agrees more with Model 2. In our Model 1, ( $O^{II}H$ ) is over-saturated and forms Hydrogen-bonded with ( $O^I$ ) as a donor (Fig. 5.2 A), it doesn't have any capability to attract extra water molecules. While in Model 2,  $O^{II}$  atoms are under-saturated, and it is possible to attract water molecules which can form a closer water layer.

## 5.4 Structural properties of interface

### 5.4.1 Hematite (001) aqueous interface

In previous experimental studies, hydrated hematite (001) surface contains several different domains. CTR data has been analyzed using different domains models. Tanwar (Tanwar et al., 2008) proposed both single domain and double domain models in which double domain models improves in fitting. Several other studies also prove the relative proportion of distinct domains depends on the preparation conditions. However, the uppermost hematite 0001 surface is believed to be O-termination domain. Considering the size limit of our simulation cell, we use single O-termination domain in our work. This hydrated O-termination domain has a structure model as  $O3-Fe-Fe-R$ . The upper surface OH functional group layer has been doubly bonded to surface Fe atoms. These OH functional groups formed hydrogen bonds with water molecules, (can act both as acceptor and donor) which produced absorbed water layer on the hematite 001 surface.

From the x-ray scattering experiments data, the electron density profile has been calculated. Here, from the geometry we generate from CPMD simulation, we also calculate and average the electron density for every frame of the trajectory. Boarding has been applied by using Gaussian distribution in the direction perpendicular to the surface. Each atom type has

different Gaussian variance to reflect the atom size. The normal Gaussian distribution has been multiplied by the atomic number. We then compare our electron density profile with experiments.

In the table 5.2, we list out the interlayer spacing from the calculations with the comparison with previous experiments and calculations study. In classical molecular dynamics, results are very sensitive to the choices of models (model 1 and model4 show difference). Our ab-initio molecular dynamics result is in very good agreement with experiments. Also agreed with the experiments, only one distinct absorbed water layer has been observed in this picture. The occupancy of water defines as the number of water per (1\*1) surface. Our calculation shows the occupancy of the water layer is 2.4, this is in the range of experimental result which is  $2.7 \pm 0.3$  and  $3.0 \pm 1.0$ . However the height of the first layer water from the surface oxygen in this work is 2.5 Å, this is a little smaller than classical MD results, but have a big difference from the experiments result. Result from Ab-initio MD confirms that this difference is not from the potential used in classical MD. (in Catalano's analysis, this error might caused by the potential used in classical MD simulation).

The first layer water absorbed to hydrated surface by forming Hydrogen bond with surface hydroxide group. From picture, hydroxide group can either stand or lay on the surface. The first layer waters can attach with H atoms in standing hydroxide which forms H-bond as acceptor (0.630 per water molecule) or attached with O atoms in lying hydroxide group which forms H-bond as donor (0.352 per water molecule). The absorbed water can also form H-bond with other water molecules including water molecules also in the absorbed layer. Every absorbed water molecule forms 1.722 H-Bonds as acceptor which is higher than average bulk water. Lying hydroxides are also H-bonded with standing hydroxides acting as donor. While each surface oxygen atom only forms 0.445 H-bonds as acceptor in total. This number is obviously smaller than oxygen atom in bulk water. The reason is lone pair electrons of surface oxygen can interact

with empty d orbital of Fe atoms (half filled for Fe<sup>3+</sup>). This leads a dramatic decrease of lone pair electrons that can interact with H empty s orbital which forms Hydrogen bond.

The oxygen-oxygen distance is also with great interests. The average H-bond length between absorbed water layer and surface oxygen is 2.83 which is very close to H-bond length in bulk water. Similar to H-bond length, from O-O Radial distribution function (RDF) in which surface oxygen are set as the center, the first peak occurs at 2.85 Å. This O-O separation distance agrees with the H-bond length in bulk water which is typically 2.8 Å. (Head Gordon and Hura, 2002). Experiments studies are shown much shorter O-O distance, 2.3 Å (Tanwar 2009) and 1.9 Å (Trainor 2004) which are not physically plausible. The reason might be the incorrect model assumption working with X-ray scattering data.

#### 5.4.2 Hematite (012) aqueous interface

We found two separate peaks which represents two absorbed layers in the electron density height distribution. Hematite (012) has two layers while 001 (only) has one layer, this is consistent with Catalano's work. Some clues can be found in H-bond analysis for this difference in the number of water layers absorbed. Comparing to (001), O<sub>i</sub> (from first layer water) above (012) surface has stronger ability forming a hydrogen bond with water molecules out of the first absorbed layer, (1.188:1.019 per O atom) especially as acceptor (0.645:0.435 per O atom).

There are two types of surface oxygen  $O^I$  and  $O^{II}$ . Our H-bond analysis shows there are H-bonding between  $O^I$  and  $O^{II}$  in which  $O^{II}$  acts as donor. Our simulation shows  $O^{II}$  has little ability forming H-bond with water as donor (0.026 per  $O^{II}$  atom), also it can't form any H-bond with water molecules as acceptor. The possible reason is  $O^{II}$  atom is tripely bonded to surface iron atoms, the lone pair electrons from  $O^{II}$  all interacts with empty Fe d orbital, so  $O^{II}$  can't H-bonded to any water molecule as acceptor. This is inconsistent with recent study by Catlaono (2007). Our simulations are for perfect o-terminated hydrated (012) surface, in the real system, if

that  $O^{II}$  is de-hydrated or less bonded to Fe atoms, it is possible that it can attract water molecule forming H-bonds. Similar to hydroxide group on (001) surface, hydroxide group containing  $O^I$  can stand or lay on the surface. They form H-bonds with first layer water and also other hydroxide groups. Due to singly Fe-bonded, oxygen is far from saturated, it forms 1.609 H-bonds as acceptor.

Seen from table 5.3, the hydrogen bonds between hydroxyl groups on the 012 surface ( $O^I$ -H--- $O^I$ ) are strong bonds whose average bond length is 2.70 Å. Contrastively,  $O^I$ -H--- $O^I$  hydrogen bonds on 001 surface are obvious weaker than Hydrogen bonds in bulk water whose average bond length is 2.90 Å. This again can be illustrated by the difference of the saturation of the oxygen atoms on two surfaces in our hydrated models.

Power spectrum has also been employed to study the properties of surface water and OH group in hematite (012)-water interface region. Power spectrum could be calculated by taking fourier transform of the velocity autocorrelation functions. (Huang et al., 2014b; Kohanoff, 1994; Thomas et al., 2013)

$$P(\omega) = m \int \langle \dot{r}(\tau) \dot{r}(t + \tau) \rangle_{\tau} e^{-i\omega t} dt$$

$\langle \dot{r}(\tau) \dot{r}(t + \tau) \rangle$  denotes the velocity autocorrelation of the velocity  $\dot{r}$ . Hydrogen atoms postions from those OD groups (all hydrogen atoms have been replaced by deuterium) and water molecules in the trajectory of hematite(012)-water interface are used to calculate power spectrum. The results are shown in Fig 5.8.

The peaks located in the range from 0-800 ( $\text{cm}^{-1}$ ) for both Fig 5.8.A and Fig 5.8.B are corresopnding to the intermolecular librational and translational motion which are hard to interperit. In Fig 5.8.B, there are peaks around 1185 ( $\text{cm}^{-1}$ ) which are not shown in Fig 5.8. A. That peak is due to the bending motion of water molecules, so that's not observed in OD groups spectrum. The value 1185 ( $\text{cm}^{-1}$ ) agrees with the experimental value 1209 ( $\text{cm}^{-1}$ ) in liquid

water. The peaks in the range from 1800-2500 ( $\text{cm}^{-1}$ ) are the contribution of OD stretching motion modes. In Fig 5.8.A,  $\text{O}^{\text{I}}\text{D}$  has a blueshift comparing to  $\text{O}^{\text{II}}\text{D}$ , this shows  $\text{O}^{\text{II}}\text{D}$  forms a relatively stronger hydrogen bond with  $\text{O}^{\text{I}}$ , while  $\text{O}^{\text{I}}\text{D}$  likely has a weakening or sometimes no Hydrogen bonds in the interfacial region. In Fig 5.8.B, in higher frequency region, there is one peak 2180 ( $\text{cm}^{-1}$ ) which is closer to experimental bulk ice frequency 2190 ( $\text{cm}^{-1}$ ) and another peak 2287 ( $\text{cm}^{-1}$ ) which is closer to experimental bulk liquid frequency 2260 ( $\text{cm}^{-1}$ ). This indicates water molecules in interfacial region have both liquid-like water and ice-like vibrational properties.

#### 5.4.3 Fe(II) absorption on hematite (001) aqueous interface

Fe ion is put randomly in the aqueous near surface at the beginning of our simulation. After equilibrium, Fe ion absorbed on the (001) surface becomes six-coordinated. It is triply bonded to the surface hydroxyl groups and also bonded to three water molecules. The absorbed Fe ion corresponds to Fe site in crystal while the Oxygen atoms of three bonded water molecules take the O sites in crystal. Proton transfer on the surface has been observed in the adsorption process. One of the hydroxyl bonded to the absorbed Fe ion loses its proton which has been attracted by another hydroxyl group that is not bonded to the absorbed Fe ion. This dehydration is an indication of the crystal growth which happens on (001) surface. The absorbed Fe ion can saturate the surface hydroxyl group which promotes the dehydration of the hydroxyl group. The surface oxygen atoms have been doubly bonded to the Fe layers below in c direction (picture), if absorbed Fe layer is full, each surface oxygen atoms will form two Fe-O bonds with the Fe ions in absorbed layer. (Only one absorbed ion in the simulation, so only one Fe-O bond is formed.) Our simulation agrees with the model “Fe adsorption on the O-layer termination” proposed by Tanwar (Tanwar et al., 2009).

The differences between different Iron states are shown in Iron-oxygen RDF. Fe ion which absorbed on the oxygen-terminated hematite (001) surface has a Fe-O bond length 2.17 Å, this is in good agreement to Fe(II)-O bond length in experiments (2.14 Å -2.18 Å needed to find the references), while Fe atom on surface and Fe atom inside the slab have Fe-O bond length 2.02 Å and 2.00 Å respectively, which agrees with average bond length in bulk hematite 2.03 Å (Blake RL, 1966; Maslen et al., 1994). This structure difference confirms that in our simulation time scale, the absorbed Fe ion is Fe(II). In the density of states analysis later, we can clearly see that in this study, the absorbed Fe ion keep Fe(II) an oxidation state in our simulation.

#### 5.4.4 Fe(II) absorption on hematite (012) aqueous interface

After randomly put the Fe(II) ion near (012) surface, Fe(II) doubly bonded to  $O^I$  atom on surface after equilibrium. Since  $O^{II}$  atoms are saturated by three Fe-O bonds and H atom, at the starting stage of the adsorption, Fe ions bond to  $O^I$  atoms on surface. Absorbed Fe ion is six-coordinated including two bonds with hydroxyl group on surface and four bonds with water. This differs from (001) surface adsorption in which Fe ion has three bonds with surface oxygen atom. Shown in the picture, the  $O^I$  atom distribution is sparse on (012) surface while surface Oxygen atoms are more dense on 001 surface. In 012 surface,  $O^I$  has two nearest  $O^I$  neighbors, the distances are around 3.0 Å.  $O^I$  atom and its two nearest neighbors are nearly in a line. Geometrically, Fe ion can't form three bonds with  $O^I$  atoms without extensive relaxation on surface. Contrastively, in (001) surface, surface oxygen atom  $O^I$  has 6 nearest  $O^I$  neighbors with a distance near 3.0 Å while those six oxygen atoms form hexagon centered in  $O^I$ . In this  $O^I$  distribution, it is possible for Fe ion absorbed three  $O^I$  atoms in a triangle.

Similar to adsorption on 001 surface, average Fe-O average bond length on (012) surface is 2.19 Å while Fe atom on surface and Fe atom inside the slab have Fe-O bond length 2.01 Å and

1.99 Å respectively. In our simulation time scale, the absorbed Fe ion is still Fe(II) while other Fe atoms are all Fe (III).

## 5.5 Electronic structural properties of ion absorption in interface

### 5.5.1 Projected density of states analysis

Our simulations show that when Fe<sup>2+</sup> ion absorbed on hematite (012) and hematite (001) surface, the extra electron will adhere to the ion. It has been clearly shown in the HOMOs pictures (Fig. 5.9) of the system. The shape of HOMO indicates the HOMO is mainly t<sub>2g</sub> electron on the Fe ion. In the Fe ion projected dos pictures (black lines in Fig. 5.10.A), the spin down curve has an occupied steep peak. This is the contribution of the extra electron (we set the ion net spin up, so this extra electron has to be spin down). Surface iron and bulk iron have very similar pdos curves since they are both Fe(III) and their bonding conditions are nearly same in the hydrated oxygen terminated hematite surface.

Interestingly, Fe(II) and Fe(III) show very different pdos properties in DFT+U framework. In high spin Fe(III) (bulk Fe and surface Fe), d bands in majority spin have been filled and bands in minority spin are unfilled. By using DFT+U model in the simulation, the spin up and spin down bands have been separated by energy because of the added U term. Bands in majority spin have been moved down and bands in minority spin have been moved up. As a result, DFT+U method predicts a greater band gap than DFT method which agrees better with experiments for Iron oxide materials containing Fe(III). Comparing to Fe(III), the t<sub>2g</sub> of majority spin of absorbed Fe(II) has been shifted right by a wide margin. The reason is the existence of the t<sub>2g</sub> electron in minority spin which introduces the column repulsion between spin up and spin down d electrons on the same site. As a result, O-p and Fe-d bands have more overlaps which would lead a more intensive Fe d-Op hybridization.

Sometimes, terminations of the crystal change the chemical environments for surface atoms. This can be displayed in the pdos distribution. Surface oxygen atoms on (001) (Fig. 5.10) surfaces is analogical to bulk oxygen atom in the pdos distribution. Type 2 (O2) surface oxygen atoms on (012) (Fig. 5.11) surface are similar to bulk oxygen, while type1 (O1) atoms differ from bulk oxygen atoms for they have more electron states at the top of conduction bands. This may indicate O1 atoms have more free lone pair electrons which mean they have stronger abilities interacting with H ion near surface to form H-bond as acceptors. Our H-bond analysis confirms this conclusion, as acceptor, each O1 atom forms 1.609 H-bonds which is much more than O2 atom (0.0) as well as oxygen atom (0.445) on (001) surface.

#### 5.5.2 The mechanism of electron transfer

The mechanism of electron transfer from absorbed Fe(II) to hematite bulk is of great interest. The injected electron have three possibilities, first, it can be trapped in Fe(II)defects near the surface. Second, it migrates to the bulk. Third, it will result in reduction of Fe(III) to Fe(II) at the edge. In our ab-initio Molecular Dynamics, the simulated system is without any defect, and the real electron transfer process would take much longer time than our simulation time scale  $\sim 10$  ps. So our simulation may only show the initial stage of the electron transfer. In our simulation, the extra electron mostly localized on the Iron ion absorbed. But we can still find difference between absorptions happen in (001)and (012)surfaces. In the (001) HOMOs picture (Fig. 5.9), it clearly show there are some fractions of the HOMO electron density migrate to the structural Fe(III), while in (012) surface HOMO, no structural Fe atoms have any electron density of the extra electron. In density of states picture, we found in (001) surface (Fig. 5.10 B), the ion-connected surface oxygen atom has spin down virtual PDOS near Fermi level while in (012) surface (Fig. 5.11 C), this spin down PDOS hasn't been shown in the energy scale. This indicates it's easier for HOMO (spin down) transferring to surface oxygen atoms on (001) surface



comparing to (012) surface. This will result in (001) surface, the localized orbital This difference implies it's easier for extra electron injection happens in (001) surface comparing to (012) surface. This is consistent with the recent study which shows electron injection occur on (001) surface while dissolutions of Fe(III) happen on (012).

Table 5.1: Energy difference between different magnetic states configurations

for (012) surface (meV/Fe atom)

+-+-	0
+--+	35.4
++--	37.9
++++	102.2

for (001) surface (meV/Fe atom)

++--++--	0
++----++	90.6
+--+---+	114.0
+--+---+	143.1
+++++++	336.0

Table 5.2: Interlayer spacing ( $\text{\AA}$ ) at the oxygen termination hydrated surface.

For (001) surface slab

	Oi-O1	O1-Fe2	Fe2-Fe3	Fe3-O4	O4-Fe5	Fe5-Fe6	Fe6-O7	O7-Fe8
This work	2.51	0.98	0.34	1.04	0.93	0.58	0.90	0.92
Exp a		1.04	0.32	0.95	0.86	0.57	0.89	0.84
Exp b	1.9 $\pm$ 0.6	1.13	0.50	0.90	0.85	0.47	0.90	0.90
MD model1	2.7	0.7	0.6	0.9	0.7	0.7	0.8	0.8
MD model4	2.8	0.9	0.3	1.0	0.90	0.5	0.9	0.9

For (012) surface slab

	Oii-Oi	Oi- $O^I$	Oi'- $O^I$	$O^I$ - $O^{II}$	$O^{II}$ -Fe1	Fe1-O3	O3-Fe2	Fe2-O4
This work	1.74	2.15	N/A	1.53	0.26	0.94	0.98	0.30
Exp a	2.0	2.60	0.9	1.40	0.37	0.93	0.65	0.35

Table 5.3: Surface hydrogen bonds statistics on hematite (001) and (012) aqueous interfaces (Bond length: Å, Degree: °)

Surface hydrogen bond								
Hematite 0001								
	bond Length Ave.	Bond length Var.	Bond length Most Prob.	Degree Ave.	Degree Var.	Degree Most Prob.	No. of H-bond Per O1 atom	No. of H-bond Per Oi Atom
O1-H---Oi	2.85	0.18	2.79	157.0	10.9	161.0	0.422	0.630
Oi-H---O1	2.81	0.17	2.79	157.0	11.0	163.5	0.236	0.352
O1-H---O1	2.90	0.14	2.83	147.1	9.0	138.6	0.209	
Oi-H---Oi	2.81	0.17	2.82	157.1	10.8	161.5		0.657
Oi-H---Oii	2.81	0.17	2.80	157.5	10.8	161.1		0.584
Oii-H---Oi	2.81	0.18	2.79	156.8	11.1	160.0		0.435
Hematite 012								
	bond Length Ave.	Bond length Var.	Bond length Most Prob.	Degree Ave.	Degree Var.	Degree Most Prob.	No. of H-bond Per O1/O2 atom	No. of H-bond Per Oi atom
$O^I$ -H---Oi	2.84	0.18	2.75	158.0	10.9	163.9	0.317	0.321
Oi-H--- $O^I$	2.81	0.17	2.71	159.0	10.4	162.6	0.472	0.477
$O^{II}$ -H---Oi	2.96	0.16	3.14	151.7	11.3	135.2	0.026	0.026
Oi-H--- $O^{II}$							0.0	0.0
$O^I$ -H--- $O^I$	2.70	0.15	2.65	154.4	10.3	155.3	0.473	
$O^{II}$ -H--- $O^I$	2.80	0.19	2.76	152.3	9.14	150.8	0.664	
Oi-H---Oi	2.83	0.17	2.78	157.6	10.9	165.5		0.456
Oi-H---Oii	2.83	0.16	2.74	158.1	10.7	164.0		0.543
Oii-H---Oi	2.83	0.18	2.79	159.2	10.8	167.0		0.645
Bulk water								
	2.83	0.16		160.6	9.42			

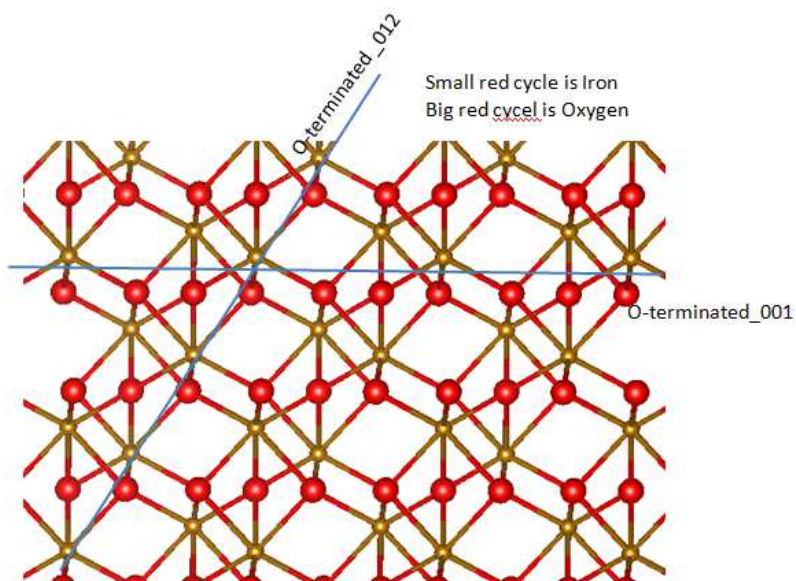


Figure 5.1: Hematite (001) and (012) surfaces terminations used in this chapter

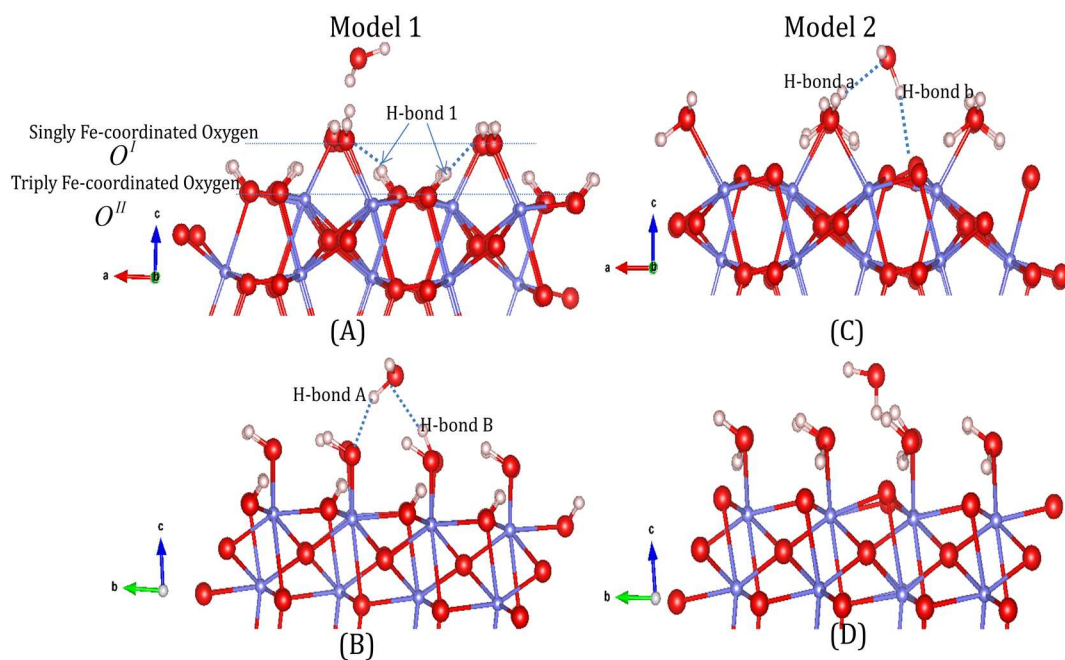


Figure 5.2: Water molecule absorbed on different hydration models for hematite (012) surface. (A) and (B) are side-views of Model 1, (C) and (D) are side-views of Model 2.

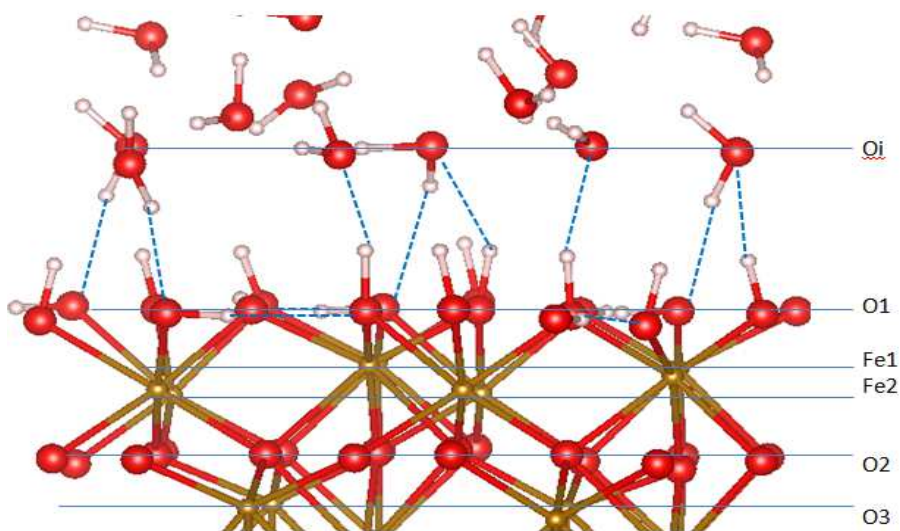


Figure 5.3: Structure of Hematite(001)–water interface

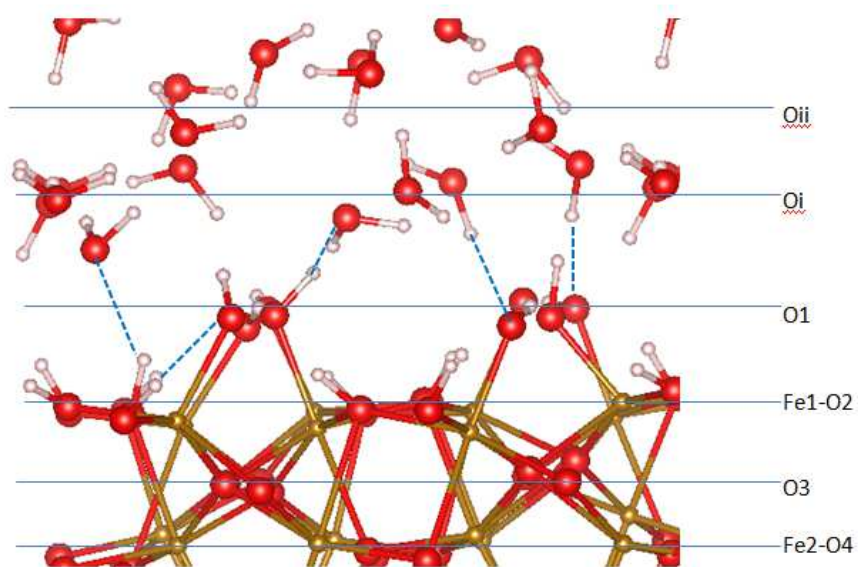
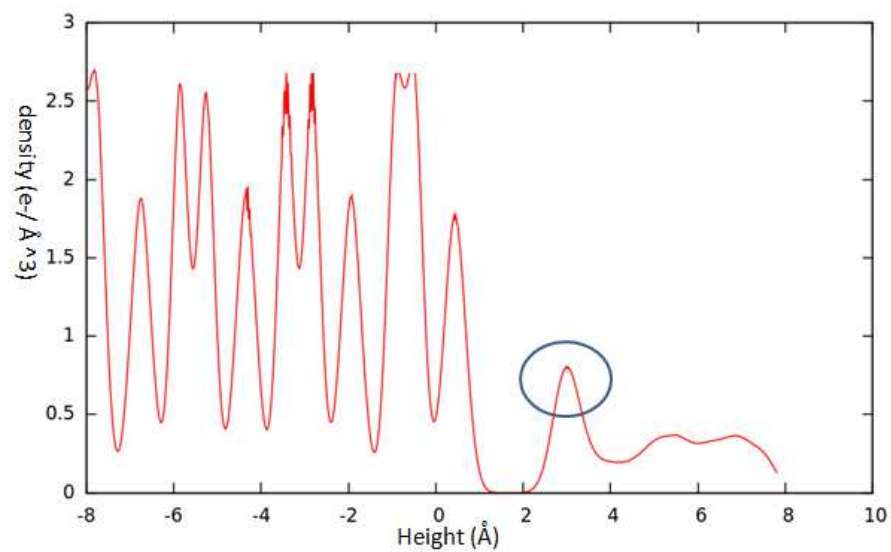
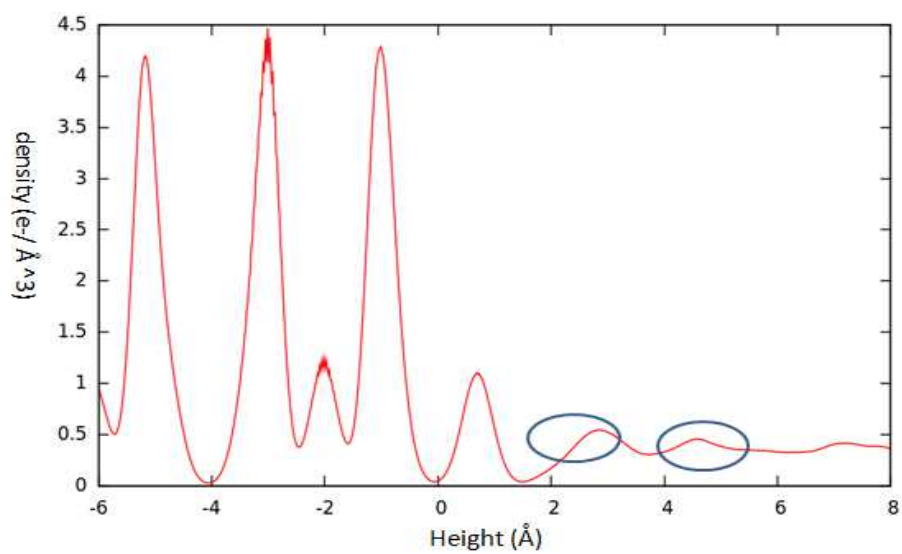


Figure 5.4: Structure of Hematite (012) –water interface

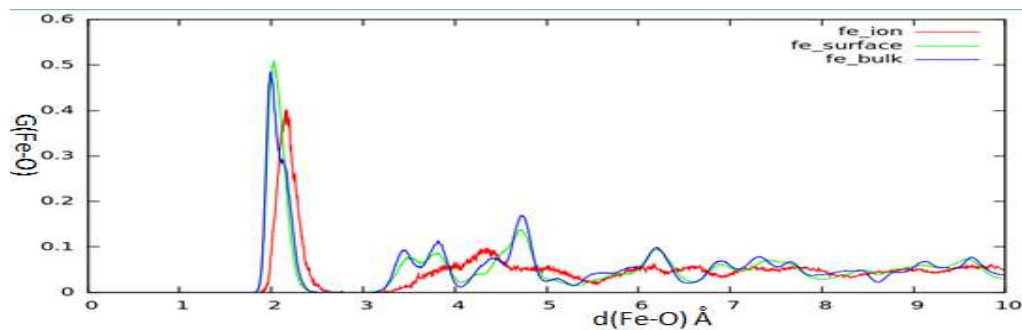


(A) Hematite (001) –water interface

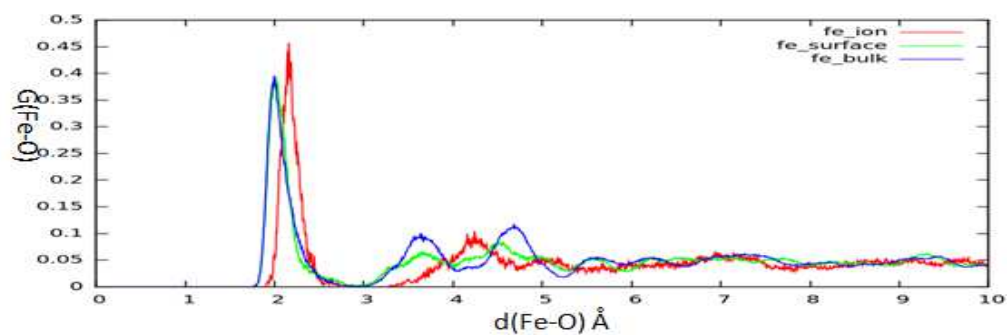


(B) Hematite (012) –water interface

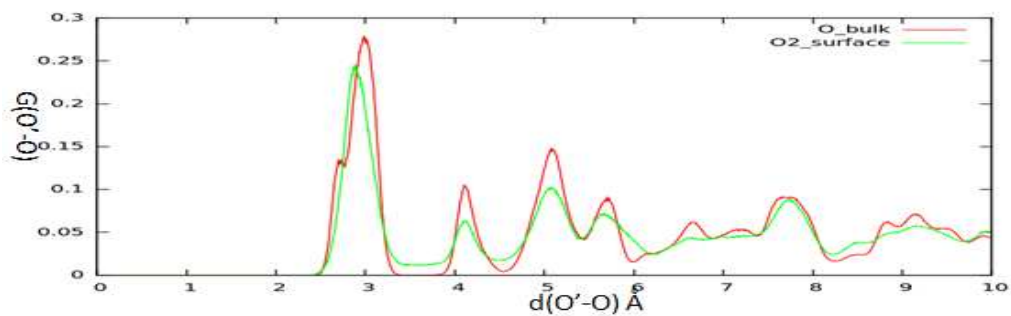
Figure 5.5: Electron density profiles for hematite-water interfaces



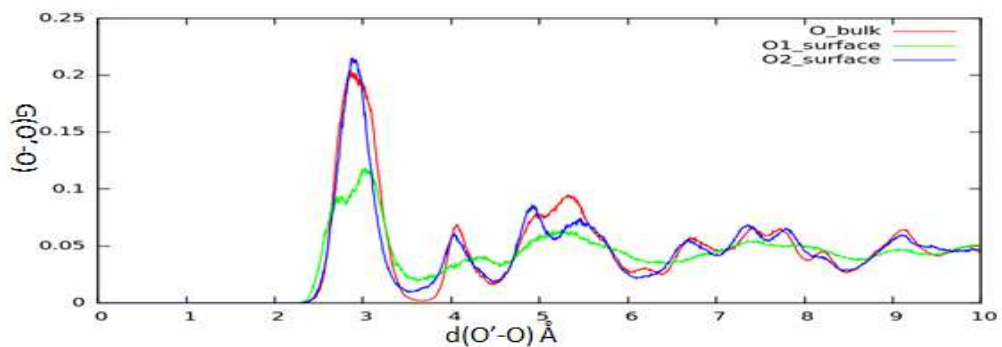
(A) Rdf of Fe-O on hematite (001)-water interface



(B) Rdf of Fe-O on hematite (012)-water interface



(C) Rdf of O'-O on hematite (001)-water interface (O' shown in legend)



(D) Rdf of O'-O on hematite (012)-water interface (O' shown in legend)

Figure 5.6: Radial distribution functions (RDFs) of Fe-O and O-O for hematite (001) and (012) water interfaces

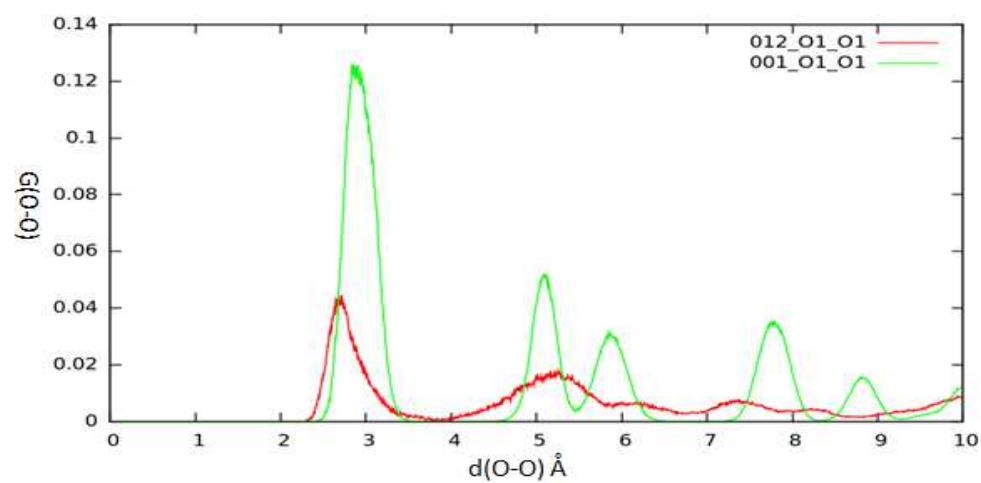
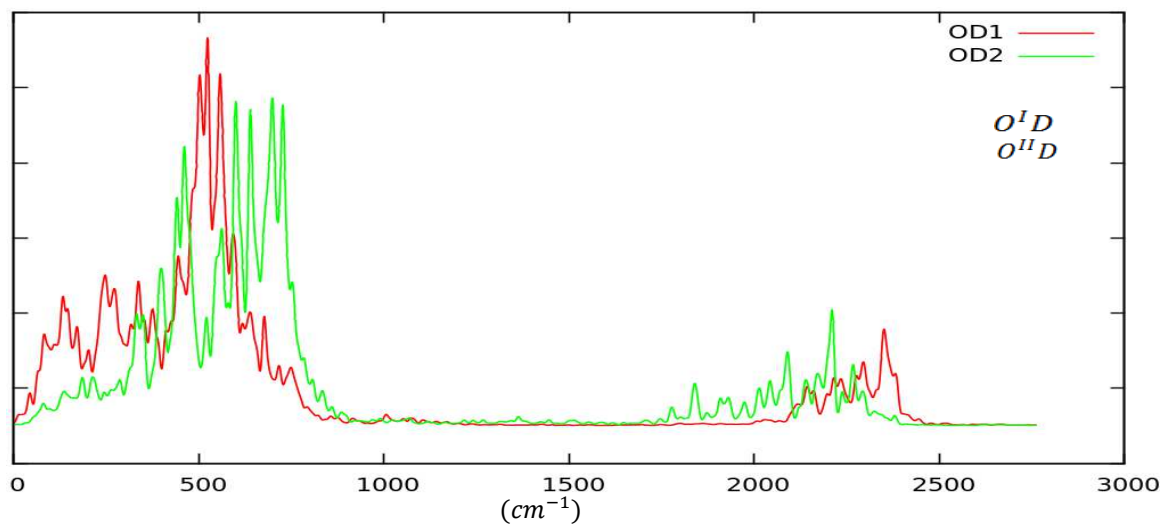
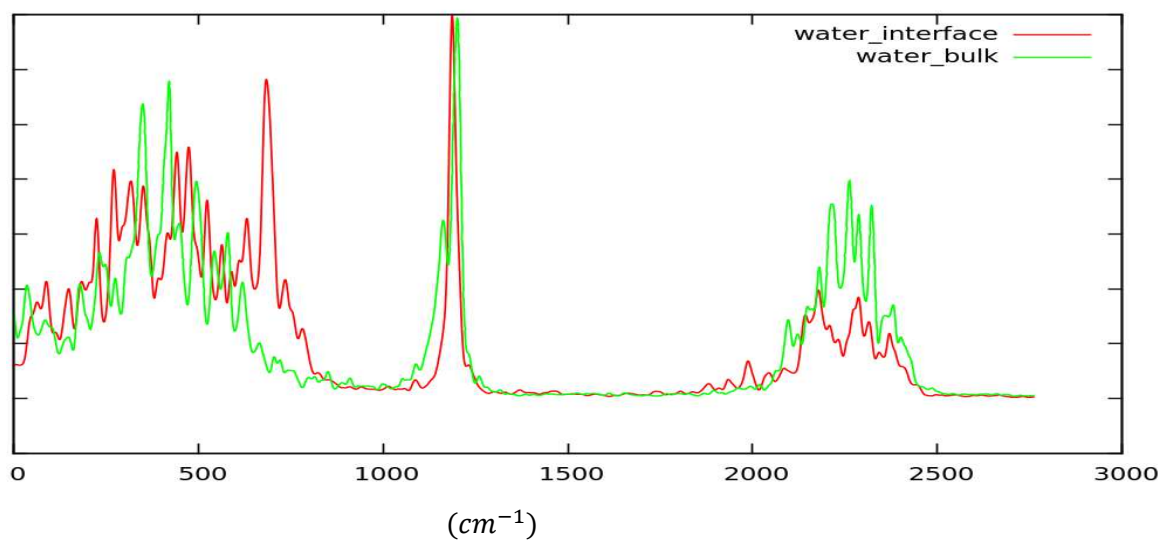


Figure 5.7: RDF of oxygen atoms on hematite (001) and (012) surfaces in aqueous interfaces ( $\text{O}'$ - $\text{O}''$ :  $\text{O}'$  and  $\text{O}''$  are both surface oxygen atoms)





(A)  $O^I D$  and  $O^{II} D$  group on surface



(B) Water molecules in simulation

Figure 5.8: Computed power spectrum of two types of OD groups on hematite (012) surface, water on interfacial region and bulk region.

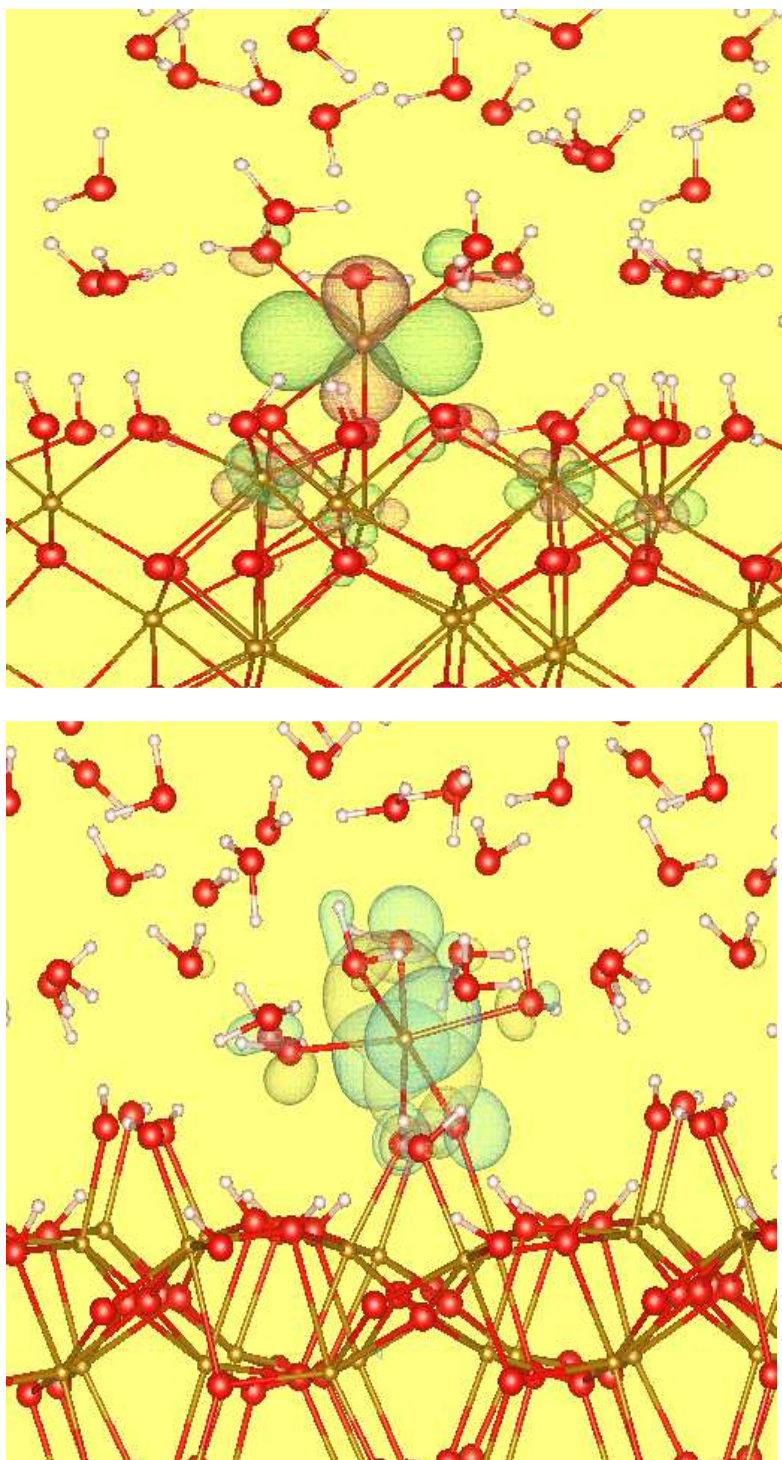
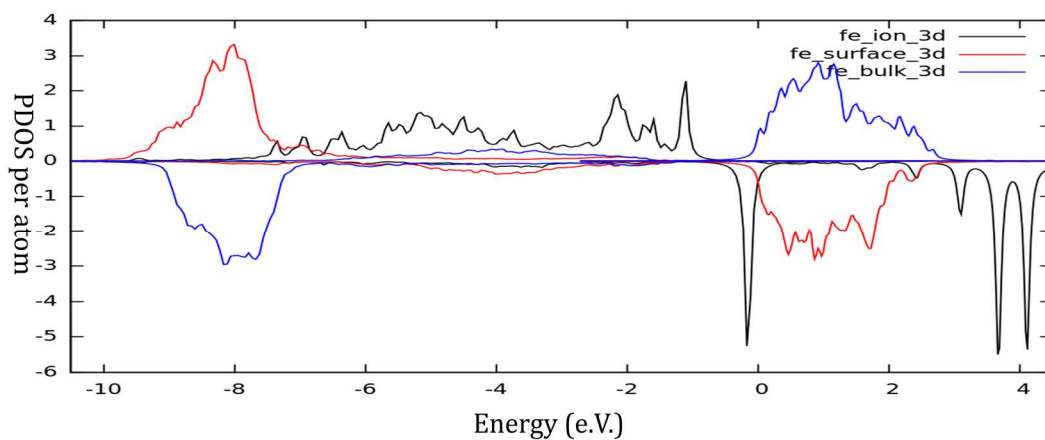
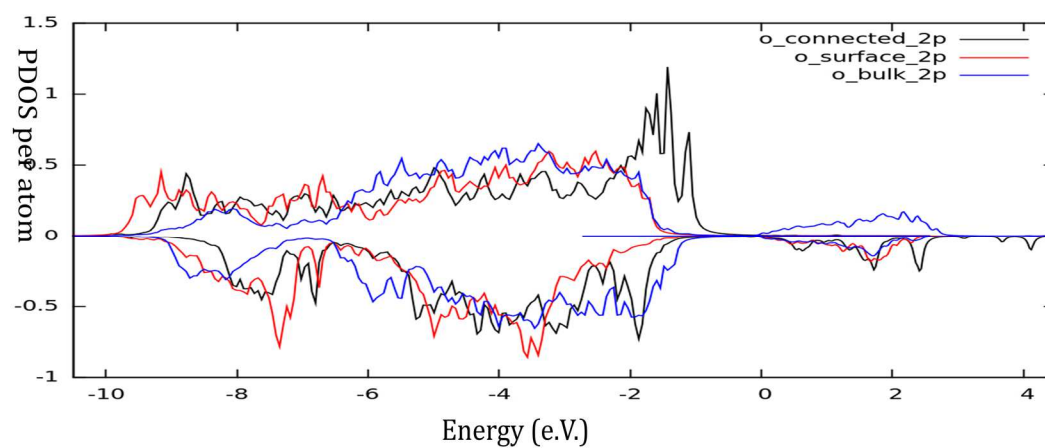


Figure 5.9: HOMOs of Fe(II) ions absorbed on hematite (001) and (012) surfaces in aqueous interfaces (upper: (001), lower: (012))

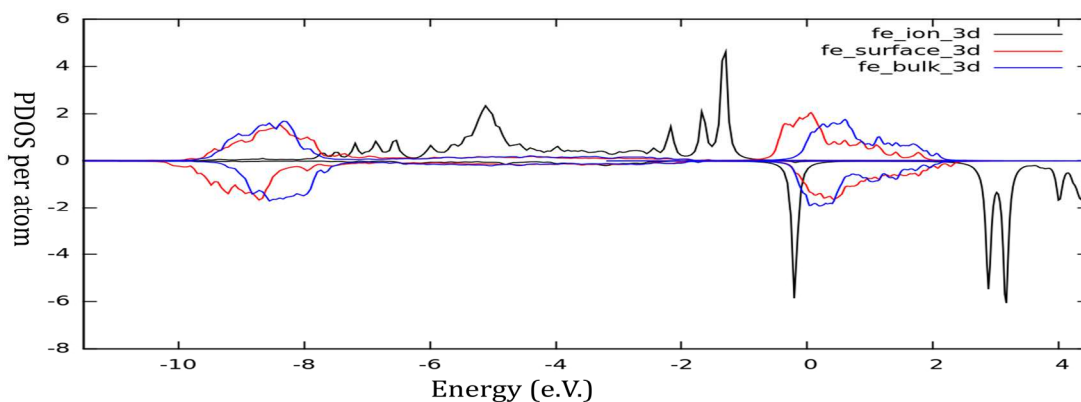


A. PDOS on different Fe atoms in the system

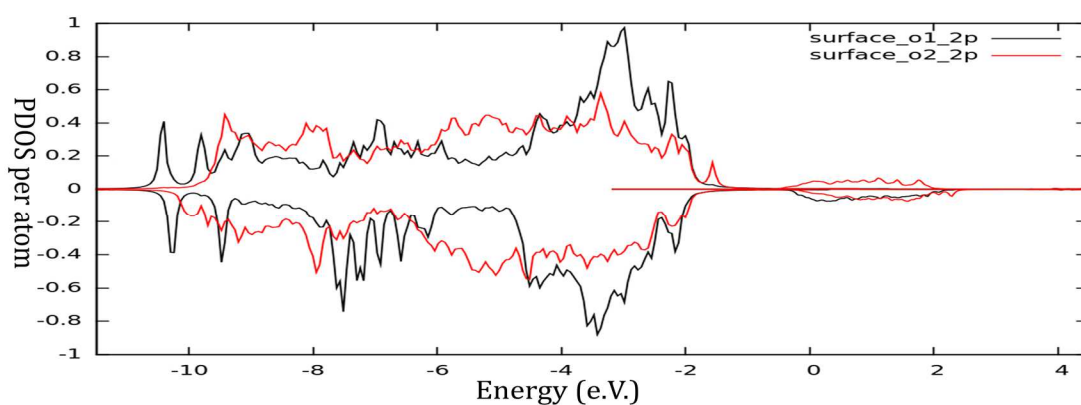


B. PDOS on different Oxygen atoms in the system

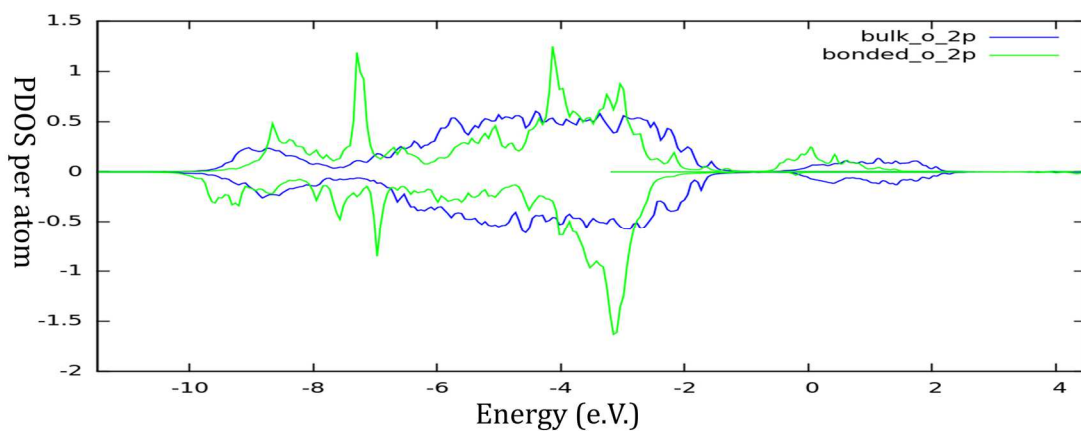
Figure 5.10: Projected density of states of different atoms in the system which has Fe(II) ion absorbed on hematite (001) in its aqueous interface (Fermi level: 0 eV)



(A) PDOS on different Fe atoms in the system



(B) PDOS on different surface oxygen atoms in the system



(C) PDOS on bulk and surface bonded oxygen atoms in the system

Figure 5.11: Projected density of states of different atoms in the system which has Fe(II) ion absorbed on hematite (012) in its aqueous interface (Fermi level: 0 eV)

## 6 STUDY OF CORUNDUM (001) SURFACE AND AQUEOUS INTERFACE

### 6.1 Introduction

Corundum is a crystalline form of aluminium oxide ( $\text{Al}_2\text{O}_3$ ) which is isostructural to hematite, and the structure of its surface is similar to many important clay minerals. It also possesses more favorable optical properties than hematite, so corundum and its surfaces especially corundum (001) surface has been studied extensively by experiments including laser spectroscopic methods such as sum frequency and optical fluorescence spectroscopy. Al-terminated and O-terminated Corundum (001) have both been investigated. Other than the excellent properties in application, O-terminated surface is with great interest also due to its structural stability. It only has doubly coordinated hydroxyls which is very stable (no protonation/dissociation) in a wide PH range (Janeček et al., 2014; Yong and Van Riemsdijk, 1999).

OH stretching mode was observed on corundum (001) surface by High-resolution electron-energy-loss spectroscopy (Coustet and Jupille, 1994). Weak ordered water layer has been found in aqueous interface with O-terminated corundum (001) surface. CTR with x-ray reflectivity (Catalano, 2010; Catalano, 2011; Catalano et al., 2006) has been used to determine the electron density profiles which show clear evidences of ordered water layers in corundum (001) aqueous interface, also (012) aqueous interface. The application of high-resolution X-ray scattering techniques can provide substantial new insights into the molecular-scale structure of the mineral–water interface. (Fenter and Sturchio, 2004) Additionally, OH stretching mod has been studied using by sum-frequency vibrational spectroscopy which can indicate the water interfacial structures. (Richmond, 2002; Shen, 1989; Shen and Ostroverkhov, 2006; Sung et al., 2012; Sung et al., 2011; Zhang et al., 2008)

Hydrogen bond can play an important role in ordered water structure in the interfaces, but hydrogen atoms can't be directly probed in any of measurements mentioned above. Using computational tools, hydrogen bond and ordering water layers could be investigated directly in atomic-scale. First principle optimizations based on density functional theory (DFT) have been employed extensively in this surface and water interface. Local basis to cluster models which represent the surface simulations have been taken (Polly et al., 2009; Wittbrodt et al., 1998). Plane-wave basis optimization to periodic computational cells is also used in investigating hydroxyls group, ion and water adsorption on corundum (001) surface (Ranea et al., 2009; Ranea et al., 2008; Roques et al., 2009; Thissen et al., 2009). Molecular dynamics (Argyris et al., 2011a; Argyris et al., 2011b; Sun et al., 2007) using classical potentials is another way in analyzing this system which contain thousands of atoms.

Ab-initio Molecular Dynamics (AIMD) simulations have recently been taken which consider quantum effects using hybrid functional (tens of atoms) (Zhang et al., 2011) and DFT functional (Huang et al., 2014b; Janeček et al., 2014) in Born Oppenheimer Molecular Dynamics (BOMD) (Barnett and Landman, 1993) framework. As discussed in chapter 3, DFT functional is much computationally cheaper than hybrid functional without losing any accuracy in bulk corundum. Considering there are no transition metals (d electrons) in the corundum (001) aqueous interface, it is a proper way employing DFT in AIMD to study this system within reasonable accuracy. Similar to other chapters, work in this chapter is also under plane-wave optimization and Car Parrinello Molecular Dynamics (CPMD) framework. For CPMD, we have simulated this corundum (001) aqueous interface in three different simulation cells. In the biggest simulation of our three CPMD simulations, the computational cell includes a (3\*3) surface slab with 100 water molecules. It contains 2312 electrons and 651 atoms. This simulation has been run on 768 CPUs in new generation supercomputer "Cascade". The computing speed is 20 s/step and 44 hours/ps in simulation.



corundum slab) in z direction, 100 water molecules ( $\sim 35$  Å, thick water slab) have been placed between two surfaces. We collect 12 ps trajectories for both the first and third simulations, and 8 ps trajectory for the second simulation since this big simulation is very time consuming.

### 6.3 Structure and electronic structure of corundum (001) surface

#### 6.3.1 Surface relaxations of corundum (001)

The changes of atom positions on cleavage can be calculated with our methods. Because of the loss of three dimensional symmetry, the calculations are quite expensive. Usually (2\*2), (2\*3) or even (3\*3) surfaces are required (at least around  $10$  Å \*  $10$  Å). Also considering the slab thickness (at least  $10$ - $15$  Å ) to represent bulk/surface region, at least few hundreds of atoms are needed to model the surface structure in a slab geometry. Because of the cost of simulating individual structures, it is not feasible to search all possible configurations. Usually, unreconstructed surfaces cut from the bulk structures are taken to be the starting structure, then the system gets optimized. Ab-initio calculations haven't been applied directly to more complicated models (such as roughness, steps) which have been considered in experiments but may need many more atoms.

Considerably surface relaxation has been observed for metal terminated surface models. Because the metal atoms on top layer are unsaturated, the top metal layer moves into the surface to form shorter bonds with the surface oxygen atoms. For corundum (001) surface, by using DFT+GGA(PBE96), in Al-terminated surface of corundum (001) (Fig. 6.1.a), our locally optimized calculations show the top Al layer has been moved down by 84.8%, this is in qualitative agreement with experimental estimates of 51.0% (Renaud, 1998). Al atoms in the top layer are triply bonded while bulk Al atoms are six coordinated. In calculation, the Al-O bond length with the first layer Al is  $1.678$  Å comparing to  $1.853$  Å and  $1.980$  Å (two types of bonds) in the bulk.



The reconstruction in an oxygen-terminated surface depends strongly on its protonation condition. Since the Metal layer hasn't been exposed to the environment (solution or vacuum), their chemical bonding conditions haven't been changed. Meanwhile the top layer oxygen atoms can be saturated by hydrogen atoms. Therefore, the layer spacing and bond length won't change too much comparing to the bulk condition. For example, in the calculated oxygen-terminated hydrated surface of corundum (001), the oxygen layer only moves up by 3.5%, and the two types of bond lengths of Al-O are 1.87 Å and 2.01 Å respectively which are only slightly longer than the bulk bond length 1.85 Å and 1.98 Å.

### 6.3.2 PDOS for Al-terminated corundum (001) surface

Projected density of states for surface atoms on Al-terminated Corundum (001) and atoms in Corundum bulk has been plotted in Fig 6.2. While valences bands looks similar from PDOS, the biggest difference between bulk and surface corundum is the existence of surface states in the edge of conduction bands which narrow the band gap from 7.0 eV to 4.0 eV. This decrease is corresponding to the Al coordination number change on the surface. Since the cleavage breaks the symmetry, top-layer Al only connects to three oxygen atoms (six-coordinated in bulk) on the surface, so less Al-p components will contribute to the valence states, those states will mix with the conduction bands (mostly Al-p) and shift the those bands left substantially.

### 6.4 Comparison of AIMD and experiments by electron density profiles

After the trajectories of AIMD simulation have been collected, the atomic positions from every frame are used to generate an electron density profile to be compared with experimental "best-fit" model. The electron density profiles are computed from the average atomic densities, each of which was multiplied by the corresponding atomic number.

In the upper panel of Fig. 6.3, electron density profiles have been plotted for three simulations described in Chapter 6.2. No significant differences have been observed in these three curves. The peaks positions for the layers in surface slab and the first absorbed water layer are all consistent in three profiles. However, the peaks for the second water layer are shown in two simulations which contain thin water slab ( $\sim 15$  Å), but not in the simulation which contains thick water slab ( $\sim 35$  Å). From the middle panel in Fig. 6.3, it is found the “best-fit” model from X-ray reflectivity only has one water layer which agrees with the simulation with thick water layer. This indicates containing a thick water slab between two surfaces of the mineral slab in the computational supercell is necessary to produce the correct absorbed water layer structure. Additionally, the width of surface oxygen layer from simulation which contains (3\*3) surface slab is very similar to the simulation which contains (2\*2) slab. Since (3\*3) surface model contains many more atoms (200 atoms) than (2\*2) model, this observation indicates (2\*2) surface could be used to model the surface relaxation in this system without losing accuracy.

In Fig. 6.4, the vertical displacement of peak positions of different layer in surface slab and absorbed water from computational model (2by2 thick corundum slab with thick water layer used here) to experimental fit model has been shown. The difference is within 0.05 Å. Fig. 6.5 is plotted to show the comparison of peak width (root mean square, RMS) from AIMD to fit model of X-ray reflectivity. RMS width from AIMD computation is  $\sim 0.09$  Å larger than rms widths in experimental fit model for the peak in the surface slab, similar absolute increase in rms width has also been identified in the absorbed water layer ( $\sim 0.052$  Å for XR and 0.065 Å for AIMD). In the experimental model-fit procedure, only the width of 1st surface oxygen layer and absorbed water layer are allowed to vary. Interestingly, exponential decay in RMS widths of layers has been found and this might be used in the model fitting procedure in future work.

## 6.5 Direct comparison of AIMD with experiments

It is not perfect to use best-fit model to produce the experimental density and compare AIMD and experimental results directly by employing electron density profile. Best-fit model from experimental data is often derived after taking some assumptions (either explicit or implicit) which may bias the interpretation of the experimental data. Each model is essentially determined by a set of parameters after taking those assumptions, and the best-fit model is the model with a set of parameters which give the best agreement with XR data. Numerical optimization tool can be applied to in the procedure to analyze X-ray data. However, this method can be blind to whether we can get another model which might lead to better agreement with the data. It is always possible that there are two or more distinct structures are all fully consistent with the X-ray experimental data. A new approach to evaluate the accuracy of simulation predicted structure to reproduce the properties of interface has been proposed and used in analysis of classical molecular dynamics simulation (Fenter et al., 2013; Fenter et al., 2011). The overall procedure is summarized here.

The X-ray reflectivity (XR) signal  $R(Q)$  is proportional to the magnitude squared of the structure factor.

$$R(Q) = (4\pi r_e/A_{uc}Q)^2|F(Q)|^2 \quad (1)$$

Here,  $A_{uc}$  is the surface unit cell area,  $r_e = 2.818 \times 10^{-5} \text{ \AA}$  is the classical electron radius. The structure factor can be calculated summing contributions from different components in the interfacial system.

$$F(Q) = F_{\text{mineral-bulk}} + F_{\text{mineral-int}} + F_{\text{water-int}} + F_{\text{water-bulk}} \quad (2)$$

$F_i(Q)$ , which in turn is the Fourier transform (FT) of the interfacial density profile  $\rho_{MD,i}(z)$ , where  $z$  is the vertical position in space.

$$F_i(Q) = \sum f_i(Q) \text{ FT } [\rho_{MD,i}(z)] \quad (3)$$

where  $f_i(Q) = \int \rho_{\text{atom},i}(z) \exp(iQ_z z) dz$  is atomic scattering factor for each atom,  $i$ .

The direct comparison between computational model and X-ray reflectivity measurement can be quantified through the parameter  $\chi^2$  which assesses the mean-square errors between the measured and calculated reflectivity normalized to the data uncertainty (Fenter et al., 2013; Fenter et al., 2011).

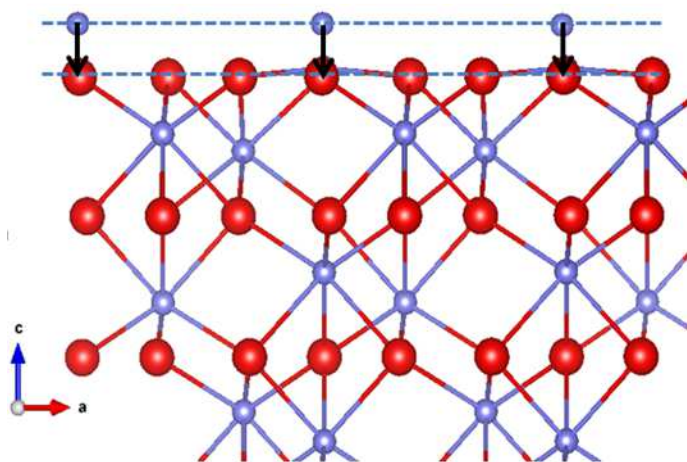
$$\chi^2 = (1/N_p) \sum_i [(R_i - R_c)/\sigma_i]^2 \quad (4)$$

$\sigma_i$  and  $R_c$  are the measured reflectivity, its uncertainty and the calculated reflectivity, the sum is over all data points. ( $i = 1 \dots N_p$ )

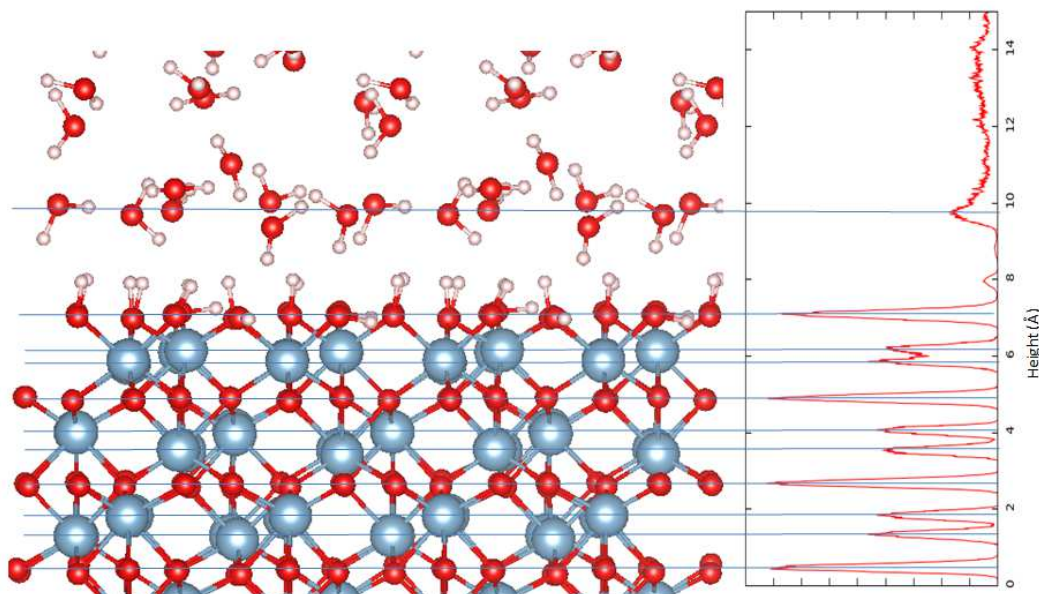
Direct comparison of AIMD simulations to X-ray reflectivity data has been carried out in the corundum (001) /aqueous fluid interface systems. The numerical values of  $\chi^2$  for those three simulations and “best-fit” model are recorded in Table 6.1. Values of electron density profiles from full AIMD trajectories are listed in the left column. It is not surprised the agreement of simulations to the experimental reflectivity data is worse than best-fit model to experimental data. However, the comparison of simulation data to X-ray reflectivity already shows a semi-quantitative agreement. Additionally, the combination of water electron density profiles generated from AIMD and surface slab profiles from best-fit model (Fig. 6.3, lower panel) has been used to compare with experimental x-ray reflectivity data. The quantitative measures of agreement for this result are listed in right column which is visibly better than the full AIMD electron density profiles.

Table 6.1: Calculated parameters  $\chi^2$  of three simulations and model-dependent fit

	Full AIMD	Water only
Simulation1: (2*2) thin surface slab/thin water slab	23.2	6.5
Simulation2: (3*3) thick surface slab/thin water slab	33.7	12.6
Simulation 3: (2*2) thick surface slab/thick water slab	63.2	36.9
Model-dependent fit	1.54	



(A) Al-terminated corundum (001) surface (Top Al layer moves down to O layer)



(B) Hydrated O-terminated corundum (001) with aqueous fluid interface

Figure 6.1: Two terminations of  $\text{Al}_2\text{O}_3$  (001) surfaces

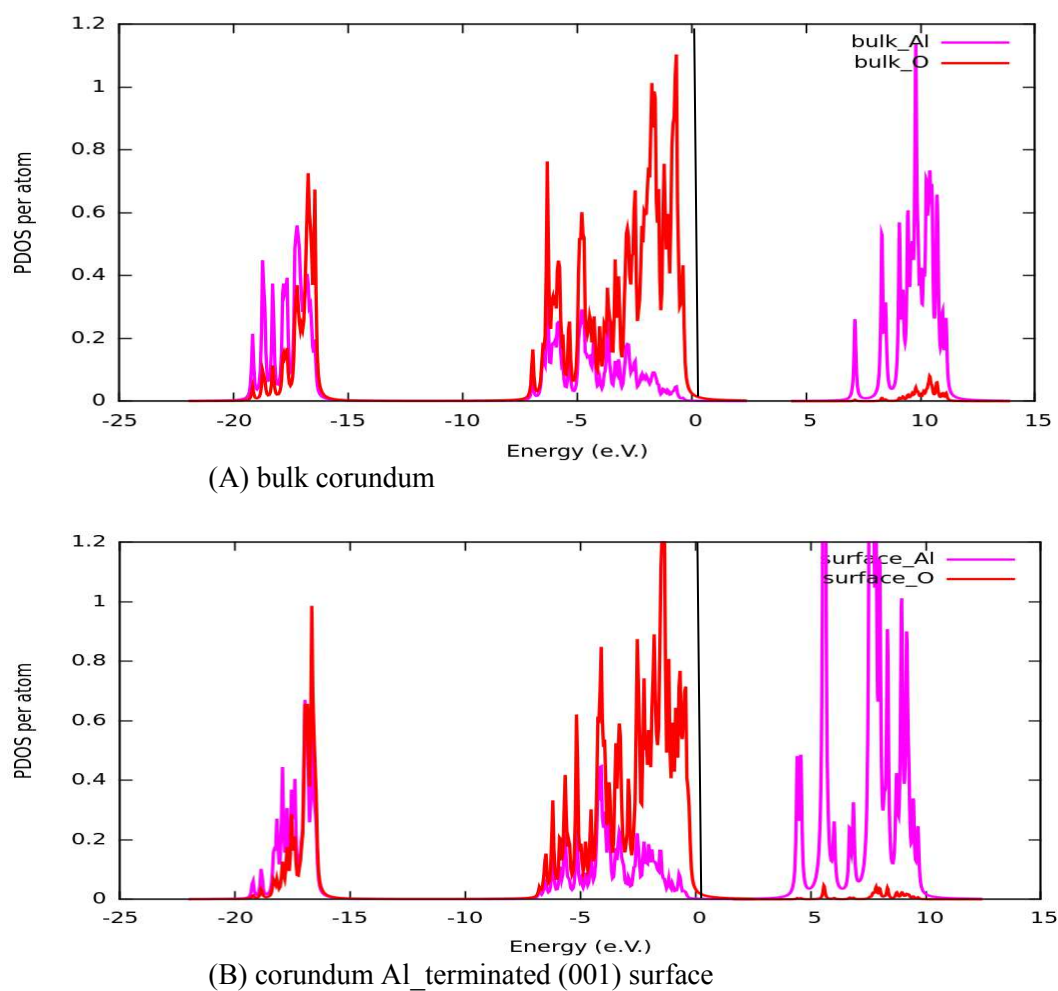


Figure 6.2: Projected density of states for atoms in surface and bulk region of Al-terminated corundum (001) using DFT

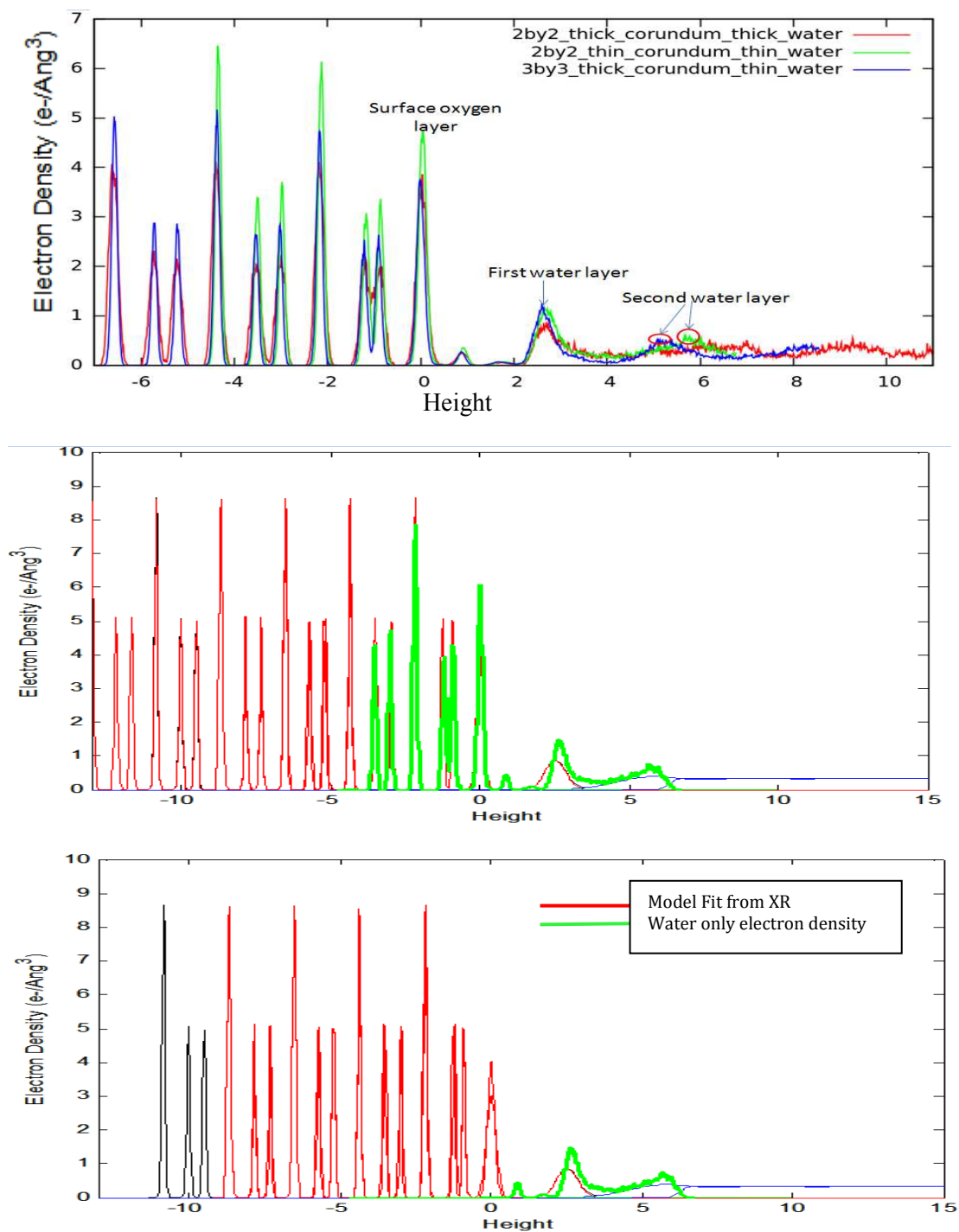


Figure 6.3: Electron density profiles of three simulations and best XR fit model for corundum (001) aqueous fluid interface. (upper: three simulations comparison; middle: best XR fit model and profile from 2by2\_thin\_corundum\_thin\_water full simulation; lower: best XR fit model and water only density from simulation)

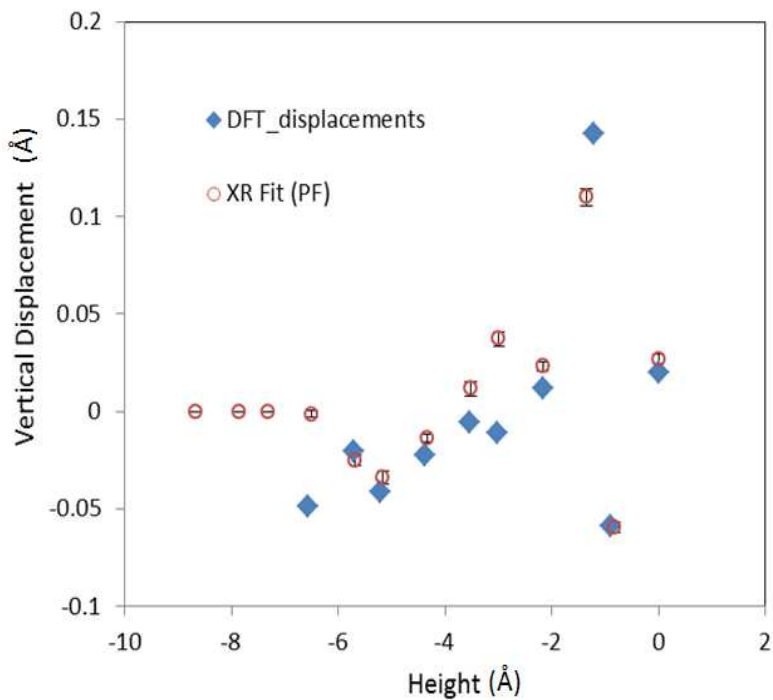


Figure 6.4: Comparison of heights of different layers from AIMD to X-Ray (vertical offset chosen to maximize overall agreement)

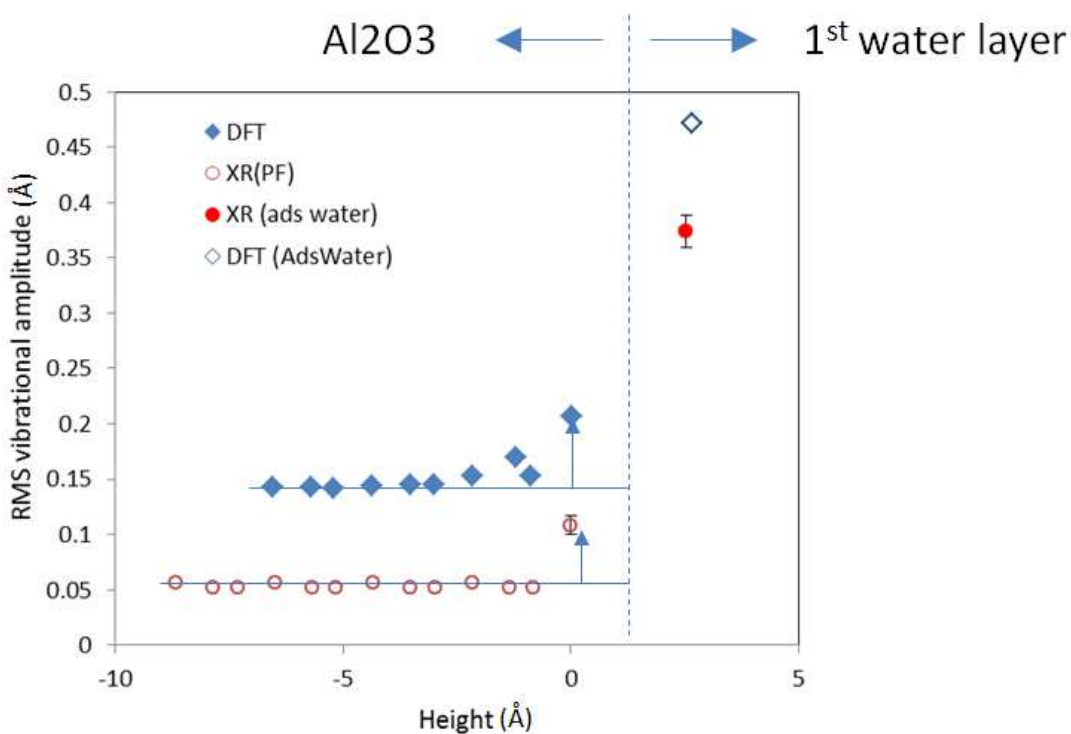


Figure 6.5: Comparison of different layers' root mean square widths from AIMD to X-Ray



## 7 SUMMARY AND FUTURE WORK

### 7.1 Summary

In this research, ab-initio methods have been employed to study bulk, surface, aqueous fluid interface regions of important mineral materials. It is observed DFT provides good predictions to corundum both in structure and electronic structure. Additional correlation needs to be added to DFT when calculating transition metal oxides/oxyhydroxides. Although DFT prediction in structure (including lattice parameters and bond lengths) is within similar accuracy comparing to DFT+U/hybrid DFT to these materials, DFT+U and hybrid DFT lead to correct physics while DFT fails to predict band gap and other properties in electronic structure.

The calculations of surface and aqueous interface of Goethite (100), Hematite (001) and (012) as well as corundum (001) have been carried out in chapter 4, 5, 6, respectively. In Chapter 4 for goethite (001), Fe-bonded water layer and one additional hydrogen bonded water layer have been observed in AIMD simulation to the goethite (100)-water interface system. Surface Fe-O bond and hydrogen bonds in interfacial region have been carefully analyzed and bond valance theory could be applied to explain changes and relations of different bond lengths. In Chapter 5 for hematite (001) and (012), ordered water layers and hydrogen bonds in interface regions from the simulations have been reported and compared to experiments. Fe (II) adsorption in interfacial region has also been simulated by AIMD, although electron transfer doesn't happen spontaneously in the 15s ps simulations, our electronic structure analysis provide some insights in understanding the electron transfer mechanism. In chapter 6 for corundum (001), surface relaxation and electronic structure of Al-terminated surface have been studied. AIMD simulations of O-terminated surface with aqueous fluid interface have been taken in different sizes of computational cells. Direct comparisons of multiple ab initio molecular dynamics (AIMD) simulations with high-resolution specular X-ray reflectivity (XR) data have been carried out.

## 7.2 Future work

Considering the difficulty and complexity in AIMD, there are two key factors in simulations which need to be improved in future work, simulation time scale and the speed of force evaluation tool. Currently, the realistic path to the time scale problem is using free energy tools (sampling methods) to avoid long time simulation. QM/MM is an efficient way to make our force evaluation faster if we are dealing with large system in which different levels' description could be applied to different regions.

In electronic structure side, one interesting question studying transition metal oxides is whether we can describe the transition metal oxides with higher level of accuracy. DMFT (Dynamics mean field theory) is developed and could be applied to bulk and surface mineral materials in future.

### 7.2.1 Sampling methods in interface simulation

Due to the limit of the modeling size of mineral/aqueous fluid interface simulation as discussed in chapter 1 and 2, only 10s ps (up to 100 ps) simulation using AIMD is feasible in the research currently. Many orders of magnitude speed up is required to study processes on mineral/aqueous fluid interfacial region such as chemical reactions or ion adsorption, which typically involve time scales of seconds to minutes. This means that if we have to explore all of phase space to see the event of interest it will take impractically long clock times using a standard MD simulation. A number of methods have been suggested to address this problem (Dellago and Bolhuis, 2009). Most of these methods attempt to sample phase space along a very efficient path between the reactant state and the product state (ideally this would be the minimum energy reaction path).

Metadynamics (Laio and Parrinello, 2002) is one popular sampling tool in studying complex system. The most significant challenge utilizing Metadynamics is the identification of

the important slowly changing variable (collective variable). For ion in solution simulations, smart collective variables have been chosen to study some specified systems effectively (Atta-Fynn et al., 2013; Atta-Fynn et al., 2012). To study complex process in interfacial region, it is possible that we can find out some smart collective variables which can help us to understand more difficult reactions computationally. Besides Metadynamics, other free energy simulation tool, such as constrained Molecular dynamics (Cauët et al., 2012), umbrella sampling or new developed sampling methods can also be employed to study properties and reactions in interfacial regions.

### 7.2.2 QM/MM method in interface simulation

The simulation of complex chemical systems often requires a multi-level description, in which a region of special interest is treated using a computationally expensive quantum mechanical (QM) model while its environment is described by a faster, simpler molecular mechanical (MM) model (Field et al., 1990; Lyne et al., 1999). The correctness and efficiency of this method has been proved from biological systems (Riccardi et al., 2006; Senn and Thiel, 2007) to physical systems (Cauët et al., 2010). In AIMD of mineral/aqueous fluid interface, the thickness of liquid water slab in the simulation can significantly influence the properties of interfacial region. But we are not focusing in the bulk water properties or process in bulk water region in interface simulations. So MM could be applied to bulk water region in which way much more bulk water molecules (or thicker water slabs) could be included without too much increase of computational cost, while QM (usually DFT or DF+U) can be applied to interfacial region which we focus on.

### 7.2.3 DMFT (dynamics mean field theory)

It has been pointed out that all the efficient methods of calculation (DFT, hybrid DFT and DFT+U) can lead to different physics in chapter 2 and chapter 3. To have an accurate view of the electronic structure for the important iron oxide materials, developing higher level calculations based on dynamic mean field theory (DMFT) is one possible solution. (Georges et al., 1996; Kotliar et al., 2006; Lechermann et al., 2006; Zgid and Chan, 2011). In this approach the intractable DFT+U problem is replaced by an impurity problem in an effective field. (It can be shown that this replacement is exact in very high dimension (Georges and Kotliar, 1992)). The impurity problem is much easier to solve than the original problem but still is a difficult numerical problem. We have made some efforts solving this problem as a full configuration interaction (CI) problem, future work is needed to improve the solver. Meanwhile, the electronic structures from DFT or DFT+U would give an approximation can be used as the starting point of real DMFT loop which could accelerate the convergence of the DMFT calculation. The implementation of interface from DFT to DMFT is needed so DMFT can be applied to transition metal oxides systems.

## Appendix

In the following sections we discuss very briefly some of the details of the approximations that are necessary to define plane wave DFT. This discussion supports the discussions of accuracy that we report in chapter 1-3 in the main text.

### A.1 Short introduction to pseudopotentials

The variation/strength of the atom center electron potential,  $V_{ext}$ , must be reduced in order for KS wave functions to be expanded in a reasonable number of terms. In order to do this pseudo potentials have been developed(Pickett, 1989). These are widely used nevertheless it is typical to have to modify these functions to obtain the accuracy required for a particular calculation (see section 3). A significant advance in the development of the pseudopotential method was made by Hamann, Schluter and Chiang (HSC)(Hamann et al., 1979) with the introduction of norm conserving psuedopotentials. While there are differences between various approaches, all popular pseudopotential adopt the basic prescription of HSC. These methods have been highly developed in the condensed matter community and are well explained and reviewed (see for example the detailed review of Pickett(Pickett, 1989) and the original papers cited therein). The basic idea of pseudopotential is that the core region of the atomic potential is replaced by a much slower varying function designed to specifically reproduce the behavior of the valence wave functions in regions outside the core (presumed to be the bonding region). The smoothed potential has a nodeless solution that can be expanded by a smaller plane-wave basis. It can be shown that with proper care, replacing the atomic potential with a pseudopotential will produce the same solutions beyond the region of replacement, while also maintaining the normalization of the orbital function.

Pseudopotentials are derived from 1<sup>st</sup> principle single atom DFT calculations at the same level of approximation (GGA or hybrid exchange) as used in the full many-atom condensed system simulation. These potentials are precomputed before use in the condensed matter calculation so the simulation remains parameter free (no parameters adjusted in the simulation). On the other hand there are issues such as the contribution of the atomic valence structure to the bonding that must be decided before the development of the pseudopotential. These choices will determine the transferability of the pseudopotential from the atomic to the condensed environment. Such issues are carefully discussed in the Picket review. In the calculations reported in the next section the affects of various assumptions will be tested by comparison of calculations to bulk structural observations.

In the HSC approach given the selection of valence orbitals (corresponding to various  $l$  to be included in the active space) a pseudopotential for each total angular momentum is found from the direct inversion of the Schrödinger equation (with a selected DFT functional) (Hamann, 1989). This produces a non-local pseudopotential of the form, equation reference goes here

$$V^{pseu} = V_M^{val}(\mathbf{r}) + \hat{V}_{ps}(\mathbf{r}, \mathbf{r}') = V_M^{val}(\mathbf{r}) + \sum_{l,m} Y_{lm}(\hat{\mathbf{r}}) V_l(r) \delta(r - r') Y_{lm}^*(\hat{\mathbf{r}}') \quad (\text{A.1})$$

where  $V_M^{val}$  is the Coulomb and exchange potential due to the (non active) valence electrons,  $Y_{lm}(\hat{\mathbf{r}})$  is the spherical harmonic defined by the angular momentum,  $l$ , and magnetic quantum,  $m$ , numbers,  $\hat{\mathbf{r}}'$  is a unit vector in the  $\mathbf{r}'$  direction, and  $V_l(r)$  is the radial potential found from the inversion of the DFT solution to the radial Schrödinger equation for the equivalent atomic problem (see HSC). The potential  $\hat{V}_{ps}$  acts on function  $\psi_1$  of  $\mathbf{r}$  as,

$$\hat{V}_{ps} \psi_l(\vec{r}) = \int \sum_{l,m} Y_{lm} V_l(\vec{r}) \delta(r - r') Y_{lm}(r') \psi_l(\vec{r}') d\vec{r}' \quad (\text{A.2})$$

The potential Eq. (A.2) has a semi-local form, neither just local (radial) or fully separable (Bylander and Kleinman, 1984). In this semi-local form, the pseudopotential is computationally

difficult to calculate with a plane-wave basis set, since the kernel integration is not separable in  $\mathbf{r}$  and  $\mathbf{r}'$  (Bylander and Kleinman, 1984). To produce a more efficient calculation while retaining as much of the atomic form as possible Kleinman and Bylander approximated the form by,

$$\hat{V}_{ps}^{KB} = V_{local}(\vec{r}) + \sum_{l,m} P_{lm}(\vec{r}) h_l P_{lm}^*(\vec{r}') \quad (\text{A.3})$$

where the atom-centered projectors  $P_{lm}(\vec{r})$  are of the form

$$P_{lm}(\vec{r}) = [V_l(r) - V_{local}(r)] \tilde{\varphi}(r) Y_{lm}(\hat{r}). \quad (\text{A.4})$$

and the coefficient  $h_l$  is

$$h_l = \left\{ 4\pi \int_0^\infty \tilde{\varphi}_l(r) [V_l(r) - V_{local}(r)] \tilde{\varphi}(r) dr \right\}^{-1} \quad (\text{A.5})$$

where  $\tilde{\varphi}_l(r)$  are the zero radial node pseudowavefunctions of the potentials,  $V_l(r)$  calculated in the atomic environment. Note that  $\hat{V}_{ps}^{KB} |\tilde{\varphi}_l Y_{lm}\rangle = V_l |\tilde{\varphi}_l Y_{lm}\rangle$ , i.e., that the fully non-local KB form preserves the form of the potential in the atomic problem. The choice of the local potential  $V_{local}(r)$  is somewhat arbitrary, but for transition metals it is often chosen to be the  $V_{l=0}(r)$  potential. A larger series expansion in pseudowavefunctions can be used to improve the fully local description of the semilocal form. This leads to the general form

$$\hat{V}_{ps}(\vec{r}, \vec{r}') = V_{local}(\vec{r}) + \sum_{l,m} \sum_{n,n'} P_{nlm}(\vec{r}) h_l^{n,n'} P_{n'lm}^*(\vec{r}') \quad (\text{A.6})$$

There is a large body of literature describing pseudopotential methods and illustrating the accuracy and efficiency of this approach. (Pickett, 1989) For use in the structural the pseudopotentials are developed entirely from fitting atomic calculations and, therefore, should not be considered as part of the data fitting process. Nevertheless, there are questions about accuracy of the representation given by Eq. (A.3), e.g. how many  $\tilde{\varphi}_{nl}(r)$  are required in the sum to accurately represent the valence structure of the condensed system and how much of the

unscreened atomic potential is assigned as the core region (roughly speaking the region removed). This is a function of the atomic structure of the particular element (e.g., separation of the highest filled lowest excited states, highest valence states etc.). In this work, for hematite and goethite calculations, we found that including the 3s and 3p functions in the active space of the pseudopotential of the  $\text{Fe}^{3+}$  ions can't considerably improved the agreement with the scattering data. The default pseudopotential included only the 3d orbitals has been used. Additional issues that have to be considered in the pseudopotential representation include: The functional form for the  $V_l(r)$  potentials selected, the evaluation of the parameters in these potentials by comparison to atomic calculations at the same level of electronic structure calculation.

The radius of the region of replacement of the external with the pseudopotential form determines to a large extent the smoothness of the pseudopotential (the larger the region the smoother the pseudopotential). However, if this region is too large the bond formation will be effected and the pseudopotential representation will produce incorrect bonding results. An example of the derived smooth pseudopotential and nodeless pseudo wavefunctions is given Figure A.1 for the  $\text{Fe}^{3+}$  ion.

$$E_{psp} = \sum_{\sigma=\uparrow,\downarrow} \sum_{i=1}^{n_{elc}^{\sigma}} \sum_{l=1}^{n_{ions}^{\sigma}} \left( \langle \psi_i^{\sigma} | V_{local}^l | \psi_i^{\sigma} \rangle + \sum_{l=0}^{l_{max}^l} \sum_{m=-1}^l \sum_{n=1}^{n_{max}^l} \sum_{n'=1}^{n_{max}^l} \langle \psi_i^{\sigma} | P_{nlm}^l \rangle h_{l,n,n'}^l \langle P_{n'lm}^l | \psi_i^{\sigma} \rangle \right) \quad (\text{A.7})$$

In the chapter 3, we will illustrate the accuracy of the various choices discussed above by direct application to the calculation of observed bulk properties of three minerals goethite ( $\text{FeOOH}$ ), hematite ( $\text{Fe}_2\text{O}_3$ ) and corundum ( $\text{Al}_2\text{O}_3$ ).

#### *The spin penalty pseudopotential*

As discussed in the text in order to reliable calculate spin ordered systems in DFT is often necessary to develop a spin order initial state prior to full optimization or dynamical simulation. In fact there may be a number of competing spin orderings in the unit cell. A convenient way to



generate these states is to introduce terms in the external potential that will stabilize the electronic wave function at a selected set of sites (*ionlist* below), i.e., add a spin penalty function to for the spin penalty pseudopotential,  $V_{psp,pen}$ . This will break the symmetry of the wave function and create spin localization. If the state is an approximation to the DFT spin Eigen functions, further optimization with the spin penalty turned off will lead to a spin ordered DFT solution. The expectation of the spin penalty energy  $E_{psp,pen}$  is,

$$E_{psp,pen} = \sum_{\sigma=\uparrow,\downarrow} \sum_{i=1}^{n_{el}^{\sigma}} \sum_{l=1}^{n_{ion}^{\sigma}} \left( \langle \psi_i^{\sigma} | V_{local}^l | \psi_i^{\sigma} \rangle + \sum_{l=0}^{l_{max}^l} \sum_{m=-1}^l \sum_{n=1}^{n_{max}^l} \sum_{n'=1}^{n_{max}^l} \left( 1 - \delta_{l,\sigma} \delta_{l,ionlist} (\xi^{\sigma} - 1) \right) \langle \psi_i^{\sigma} | P_{nlm}^l \rangle h_{l,n,n'}^l \langle P_{n'lm} | \psi_i^{\sigma} \rangle \right) \quad (A.8)$$

#### *Projected density of states from pseudo atomic orbitals*

The projected density of states (PDOS) are calculated from

$$\rho_i(\epsilon) = \sum_{n,n'} |\langle \tilde{\phi}_{i,n'} | \psi_n \rangle|^2 \delta(\epsilon - \epsilon_n) \quad (9)$$

$i$  is the atom index for the PDOS,  $n$  is the index of valence states in the system.  $\tilde{\phi}_{i,n'}$  is the  $n'$ th pseudo atomic orbital centered in the  $i$ th atom. Pseudo atomic orbital is generated by solving Kohn-Sham equation (2.3) using pseudopotential approach to single atoms.

#### A.2. Exchange correlation functions

##### *Hubbard like Coulomb and exchange (DFT+U)*

In DFT framework, most exchange correlation functionals are generated from expansions around homogenous electron gas limit. So when DFT is used to the systems which have localized electrons, the predicted electronic states can be significantly away from the localization.

DFT+U is inspired by Hubbard model which can be used to strong correlated system. It adds Hubbard term (on-site Coulomb and exchange) to DFT functional for strong correlated electrons (d, f electrons...), and use regular DFT functional to other valence electrons. The Hubbard term is expressed using Slater integrals and local occupation matrix.

$$E_{Hub} = \frac{1}{2} \sum_{t,\sigma} \sum_{m,n,x,y} \rho_{mn}^{t\sigma} \rho_{xy}^{t-\sigma} \langle \chi_m^t, \chi_x^t | V_{ee} | \chi_n^t, \chi_y^t \rangle + \frac{1}{2} \sum_{t,\sigma} \sum_{m,n,x,y} \rho_{mn}^{t\sigma} \rho_{xy}^{t\sigma} (\langle \chi_m^t, \chi_x^t | V_{ee} | \chi_n^t, \chi_y^t \rangle - \langle \chi_m^t, \chi_n^t | V_{ee} | \chi_x^t, \chi_y^t \rangle) \quad (10)$$

$$\rho_{mn}^{t\sigma} = \sum_k f_k \langle \chi_m^t | \varphi_k^\sigma \rangle \langle \varphi_k^\sigma | \chi_n^t \rangle \quad (11)$$

But the double-counting problem raised, because the Hartree term and exchange-correlation term in DFT functional both include some fragments of Column interactions. The double counting term has been derived and been deducted from the total energy functional.

$$E_{DFT+u}[\rho(r)] = E_{DFT}[\rho(r)] + E_{Hub}[\{\rho_{mm}^{t\sigma}\}] - E_{dc}[\{\rho^{t\sigma}\}] \quad (12)$$

$$E_{dc} = \frac{1}{2} \bar{U} \sum_t N_\sigma^t N_{-\sigma}^t + \frac{1}{2} (\bar{U} - \bar{J}) \sum_t \sum_\sigma N_\sigma^t (N_{-\sigma}^t - 1) \quad (13)$$

N is the trace of local occupation matrix.  $\bar{U}$  and  $\bar{J}$  is average Coulomb and exchange parameters. There are different approaches to calculate those two numbers. Dudarev used those two average parameters to replace Slater integrals in equation, and DFT+U functionals have been simplified. In this approach, only  $(\bar{U} - \bar{J})$  is meaningful.

$$E_{total} = E_{DFT} + \frac{1}{2} (\bar{U} - \bar{J}) \sum_{t\sigma} (\sum_j \rho_{jj}^{t\sigma} - \sum_{jl} \rho_{jl}^{t\sigma} \rho_{lj}^{t\sigma}) \quad (14)$$

There are different choices of projectors  $\chi_m^t$  which can be used in the calculation. (.ie. projectors from Pseudopotential or PAW), and the number of projectors for each calculation is

limited, so the cost of DFT+U method is approximately equivalent to DFT methods which is much cheaper than adding exact exchange.

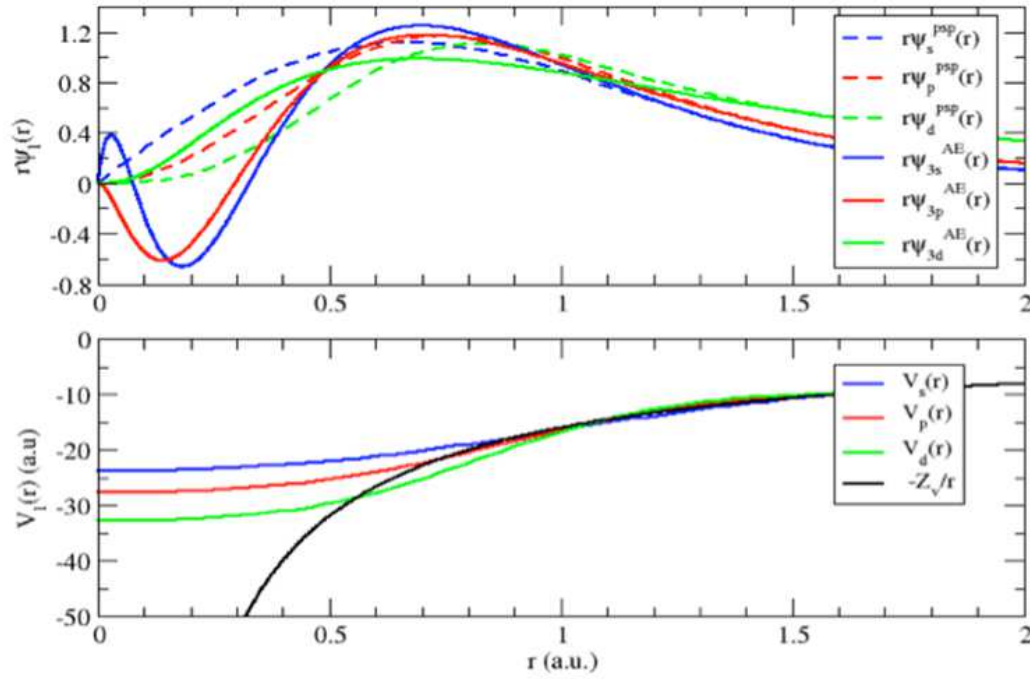


Figure A.1: Comparison of the pseudowavefunctions (dashed lines) with the full-core atomic valence wavefunctions (solid lines) for  $\text{Fe}^{3+}$ . The lower panel shows the corresponding pseudopotentials.

## References

- Adamo, C. and Barone, V. (1999) Toward reliable density functional methods without adjustable parameters: The PBE0 model. *Journal of Chemical Physics* 110, 6158-6170.
- Alvarez, M., Sileo, E.E. and Rueda, E.H. (2008) Structure and reactivity of synthetic Co-substituted goethites. *American Mineralogist* 93, 584-590.
- Anisimov, V.I., Solovyev, I.V., Korotin, M.A., Czyżyk, M.T. and Sawatzky, G.A. (1993) Density-functional theory and NiO photoemission spectra. *Physical Review B* 48, 16929-16934.
- Anovitz, L.M., Cole, D.R., Rother, G., Valley, J.W. and Jackson, A. (2010) Analysis of nanoporosity in the St. Peter Sandstone Using (Ultra) Small Angle Neutron Scattering. *Geochimica Et Cosmochimica Acta* 74, A26-A26.
- Anovitz, L.M., Lynn, G.W., Cole, D.R., Rother, G., Allard, L.F., Hamilton, W.A., Porcar, L. and Kim, M.H. (2009) A new approach to quantification of metamorphism using ultra-small and small angle neutron scattering. *Geochimica Et Cosmochimica Acta* 73, 7303-7324.
- Aquino, A.J.A., Tunega, D., Haberhauer, G., Gerzabek, M.H. and Lischka, H. (2006) Quantum Chemical Adsorption Studies on the (110) Surface of the Mineral Goethite. *The Journal of Physical Chemistry C* 111, 877-885.
- Argyris, D., Ashby, P.D. and Striolo, A. (2011a) Structure and Orientation of Interfacial Water Determine Atomic Force Microscopy Results: Insights from Molecular Dynamics Simulations. *ACS Nano* 5, 2215-2223.
- Argyris, D., Ho, T.A., Cole, D.R. and Striolo, A. (2011b) Molecular Dynamics Studies of Interfacial Water at the Alumina Surface. *J. Phys. Chem. C* 115, 2038-2046.
- Ashcroft, N.W. and Mermin, N.D. (1976) *Solid state physics*. Holt, New York,.
- Atta-Fynn, R., Bylaska, E.J. and De Jong, W.A. (2013) Importance of Counteranions on the Hydration Structure of the Curium Ion. *The Journal of Physical Chemistry Letters* 4, 2166-2170.
- Atta-Fynn, R., Johnson, D.F., Bylaska, E.J., Ilton, E.S., Schenter, G.K. and de Jong, W.A. (2012) Structure and Hydrolysis of the U (IV), U (V), and U (VI) Aqua Ions from Ab Initio Molecular Simulations. *Inorganic Chemistry*.
- Barnett, R.N. and Landman, U. (1993) Born-Oppenheimer molecular-dynamics simulations of finite systems: Structure and dynamics of (H<sub>2</sub>O)<sub>2</sub>. *Physical review B* 48, 2081.
- Becke, A.D. (2014) Perspective: Fifty years of density-functional theory in chemical physics. *Journal of Chemical Physics* 140.

Becker, U., Hochella, M.F. and Apra, E. (1996) The electronic structure of hematite{001} surfaces: Applications to the interpretation of STM images and heterogeneous surface reactions. *American Mineralogist* 81, 1301-1314.

Blake RL, H.R., Zoltai T, Finger LW (1966) Refinement of the hematite structure. *American Mineralogist* 51, 123-129.

Bocquet, S. and Kennedy, S.J. (1992) The Néel temperature of fine particle goethite. *Journal of Magnetism and Magnetic Materials* 109, 260-264.

Bogatko, S.A., Bylaska, E.J. and Weare, J.H. (2010) First Principles Simulation of the Bonding, Vibrational, and Electronic Properties of the Hydration Shells of the High-Spin Fe<sup>3+</sup> Ion in Aqueous Solutions. *The Journal of Physical Chemistry A* 114, 2189-2200.

Boily, J.-F. (2012) Water Structure and Hydrogen Bonding at Goethite/Water Interfaces: Implications for Proton Affinities. *The Journal of Physical Chemistry C* 116, 4714-4724.

Brown, G.E. (2001) Surface science - How minerals react with water. *Science* 294, 67-+.

Brown, G.E., Henrich, V.E., Casey, W.H., Clark, D.L., Eggleston, C., Felmy, A., Goodman, D.W., Grätzel, M., Maciel, G., McCarthy, M.I., Nealson, K.H., Sverjensky, D.A., Toney, M.F. and Zachara, J.M. (1999) Metal oxide surfaces and their interactions with aqueous solutions and microbial organisms. *Chem Rev* 99, 77-174.

Brown, G.E., Henrich, V.E., Casey, W.H., Clark, D.L., Eggleston, C., Felmy, A., Goodman, D.W., Grätzel, M., Maciel, G., McCarthy, M.I., Nealson, K.H., Sverjensky, D.A., Toney, M.F. and Zachara, J.M. (1998) Metal Oxide Surfaces and Their Interactions with Aqueous Solutions and Microbial Organisms. *Chem Rev* 99, 77-174.

Brown, G.E. and Sturchio, N.C. (2002) An overview of synchrotron radiation applications to low temperature geochemistry and environmental science. *Applications of Synchrotron Radiation in Low-Temperature Geochemistry and Environmental Sciences* 49, 1-115.

Brown, I.D. (1987) Recent developments in the bond valence model of inorganic bonding. *Phys Chem Minerals* 15, 30-34.

Burke, K. (2012) Perspective on density functional theory. *Journal of Chemical Physics* 136.

Bylander, D.M. and Kleinman, L. (1984) Outer-Core Electron and Valence Electron Pseudopotential. *Physical Review B* 29, 2274-2276.

Bylaska, E.J., Tsemekhman, K., Baden, S.B., Weare, J.H. and Jonsson, H. (2011) Parallel implementation of  $\gamma$ -point pseudopotential plane-wave DFT with exact exchange. *Journal of Computational Chemistry* 32, 54-69.

Bylaska, E.J., Valiev, M., Rustad, J.R. and Weare, J.H. (2007) Structure and dynamics of the hydration shells of the Al<sup>3+</sup> ion. *The Journal of Chemical Physics* 126, 104505-104508.

Car, R. and Parrinello, M. (1985a) Unified Approach for Molecular-Dynamics and Density-Functional Theory. *Physical Review Letters* 55, 2471-2474.

Car, R. and Parrinello, M. (1985b) Unified Approach for Molecular Dynamics and Density-Functional Theory. *Physical Review Letters* 55, 2471-2474.

Catalano, J.G. (2010) Relaxations and interfacial water ordering at the corundum (110) surface. *The Journal of Physical Chemistry C* 114, 6624-6630.

Catalano, J.G. (2011) Weak interfacial water ordering on isostructural hematite and corundum (001) surfaces. *Geochimica Et Cosmochimica Acta* 75, 2062-2071.

Catalano, J.G., Fenter, P. and Park, C. (2007) Interfacial water structure on the (012) surface of hematite: Ordering and reactivity in comparison with corundum. *Geochimica Et Cosmochimica Acta* 71, 5313-5324.

Catalano, J.G., Fenter, P., Park, C., Rosso, K.M., Friedrich, A.J. and Otemuyiwa, B.T. (2010a) Fe(II)-induced structural transformations of hematite surfaces and their impact on contaminants. *Geochimica Et Cosmochimica Acta* 74, A150-A150.

Catalano, J.G., Fenter, P., Park, C., Zhang, Z. and Rosso, K.M. (2010b) Structure and oxidation state of hematite surfaces reacted with aqueous Fe(II) at acidic and neutral pH. *Geochimica Et Cosmochimica Acta* 74, 1498-1512.

Catalano, J.G., Park, C., Zhang, Z. and Fenter, P. (2006) Termination and water adsorption at the  $\alpha$ -Al<sub>2</sub>O<sub>3</sub> (012)-aqueous solution interface. *Langmuir* 22, 4668-4673.

Cauët, E., Bogatko, S., Weare, J.H., Fulton, J.L., Schenter, G.K. and Bylaska, E.J. (2010) Structure and dynamics of the hydration shells of the Zn ion from ab initio molecular dynamics and combined ab initio and classical molecular dynamics simulations. *The Journal of chemical physics* 132, 194502.

Cauët, E., Bogatko, S.A., Bylaska, E.J. and Weare, J.H. (2012) Ion Association in AlCl<sub>3</sub> Aqueous Solutions from Constrained First-Principles Molecular Dynamics. *Inorganic chemistry* 51, 10856-10869.

Cheng, L., Fenter, P., Nagy, K.L., Schlegel, M.L. and Sturchio, N.C. (2001) Molecular-Scale Density Oscillations in Water Adjacent to a Mica Surface. *Physical Review Letters* 87, 156103.

Ciccacci, F., Braicovich, L., Puppini, E. and Vescovo, E. (1991) Empty electron states in Fe<sub>2</sub>O<sub>3</sub> by ultraviolet inverse-photoemission spectroscopy. *Physical Review B* 44, 10444-10448.

Coey, J.M.D. and Sawatzky, G.A. (1971) A study of hyperfine interactions in the system (Fe 1-x Rh x ) 2 O 3 using the Mossbauer effect (Bonding parameters). *Journal of Physics C: Solid State Physics* 4, 2386.

Condon, N.G., Leibsle, F.M., Lennie, A.R., Murray, P.W., Parker, T.M., Vaughan, D.J. and Thornton, G. (1998) Scanning tunnelling microscopy studies of  $\alpha$ -Fe<sub>2</sub>O<sub>3</sub>(0001). *Surface Science* 397, 278-287.

Cornell, R.M. and Schwertmann, U. (2006) The iron oxides: structure, properties, reactions, occurrences and uses. John Wiley & Sons.

Cornell, R.M.S.U. (2003) The iron oxides : structure, properties, reactions, occurrences, and uses. Wiley-VCH, Weinheim.

Coustet, V. and Jupille, J. (1994) High-resolution electron-energy-loss spectroscopy of isolated hydroxyl groups on  $\alpha$ -Al<sub>2</sub>O<sub>3</sub>(0001). *Surface Science* 307–309, Part B, 1161-1165.

Cox, P.A. (1992) Transition Metal Oxides. Oxford.

de Leeuw, N.H. and Cooper, T.G. (2007) Surface simulation studies of the hydration of white rust Fe(OH)(2), goethite  $\alpha$ -FeO(OH) and hematite  $\alpha$ -Fe(2)O(3). *Geochimica Et Cosmochimica Acta* 71, 1655-1673.

Dellago, C. and Bolhuis, P.G. (2009) Transition path sampling and other advanced simulation techniques for rare events, *Advanced Computer Simulation Approaches for Soft Matter Sciences III*. Springer, pp. 167-233.

Dräger, G., Czolbe, W. and Leiro, J.A. (1992) High-energy-spectroscopy studies of a charge-transfer insulator: X-ray spectra of  $\alpha$ -Fe<sub>2</sub>O<sub>3</sub>. *Physical Review B* 45, 8283-8287.

Dudarev, S.L., Botton, G.A., Savrasov, S.Y., Humphreys, C.J. and Sutton, A.P. (1998) Electron-energy-loss spectra and the structural stability of nickel oxide: An LSDA+U study. *Physical Review B* 57, 1505-1509.

Eng, P.J., Trainor, T.P., Brown Jr., G.E., Waychunas, G.A., Newville, M., Sutton, S.R. and Rivers, M.L. (2000) Structure of the Hydrated  $\alpha$ -Al<sub>2</sub>O<sub>3</sub> (0001) Surface. *Science* 288, 1029-1033.

Fenter, P., Kerisit, S., Raiteri, P. and Gale, J.D. (2013) Is the Calcite–Water Interface Understood? Direct Comparisons of Molecular Dynamics Simulations with Specular X-ray Reflectivity Data. *The Journal of Physical Chemistry C* 117, 5028-5042.

Fenter, P., Lee, S.S., Park, C., Catalano, J., Zhang, Z. and Sturchio, N.C. (2010a) Imaging interfacial topography and reactivity with X-rays. *Geochimica Et Cosmochimica Acta* 74, A287-A287.

Fenter, P., Lee, S.S., Park, C., Catalano, J.G., Zhang, Z. and Sturchio, N.C. (2010b) Probing interfacial reactions with X-ray reflectivity and X-ray reflection interface microscopy: Influence of NaCl on the dissolution of orthoclase at pOH 2 and 85 degrees C. *Geochimica Et Cosmochimica Acta* 74, 3396-3411.

Fenter, P., Lee, S.S., Skelton, A.A. and Cummings, P.T. (2011) Direct and quantitative comparison of pixelated density profiles with high-resolution X-ray reflectivity data. *Journal of Synchrotron Radiation* 18, 257-265.

Fenter, P. and Sturchio, N.C. (2004) Mineral-water interfacial structures revealed by synchrotron X-ray scattering. *Progress in Surface Science* 77, 171-258.

Fenter, P.A. (2002) X-ray reflectivity as a probe of mineral-fluid interfaces: A user guide. *Applications of Synchrotron Radiation in Low-Temperature Geochemistry and Environmental Sciences* 49, 149-220.

Field, M.J., Bash, P.A. and Karplus, M. (1990) A combined quantum mechanical and molecular mechanical potential for molecular dynamics simulations. *Journal of Computational Chemistry* 11, 700-733.

Finger, L.W. and Hazen, R.M. (1980) Crystal structure and isothermal compression of Fe<sub>2</sub>O<sub>3</sub>, Cr<sub>2</sub>O<sub>3</sub>, and V<sub>2</sub>O<sub>3</sub> to 50 kbars. *Journal of Applied Physics* 51, 5362-5367.

Fitts, J.P., Machesky, M.L., Wesolowski, D.J., Shang, X., Kubicki, J.D., Flynn, G.W., Heinz, T.F. and Eissenthal, K.B. (2005) Second-harmonic generation and theoretical studies of protonation at the water/ $\alpha$ -TiO<sub>2</sub> (110) interface. *Chemical Physics Letters* 411, 399-403.

Fujimori, A., Saeki, M., Kimizuka, N., Taniguchi, M. and Suga, S. (1986) Photoemission satellites and electronic structure of Fe<sub>2</sub>O<sub>3</sub>. *Physical Review B* 34, 7318-7328.

Fulton, J.L., Bylaska, E.J., Bogatko, S., Balasubramanian, M., Cauet, E., Schenter, G.K. and Weare, J.H. (2012) Near-Quantitative Agreement of Model-Free DFT-MD Predictions with XAFS Observations of the Hydration Structure of Highly Charged Transition-Metal Ions. *Journal of Physical Chemistry Letters* 3, 2588-2593.

Fulton, J.L., Kathmann, S.M., Schenter, G.K., Bylaska, E.J., Bogatko, S.A. and Weare, J.H. (2010) XAFS spectroscopy and molecular dynamics: Aqueous ions and ion pairs under non-ideal conditions. *Geochimica Et Cosmochimica Acta* 74, A311-A311.

Georges, A. and Kotliar, G. (1992) Hubbard-Model in Infinite Dimensions. *Phys Rev B* 45, 6479-6483.

Georges, A., Kotliar, G., Krauth, W. and Rozenberg, M.J. (1996) Dynamical mean-field theory of strongly correlated fermion systems and the limit of infinite dimensions. *Rev Mod Phys* 68, 13-125.

Ghose, S.K., Waychunas, G.A., Trainor, T.P. and Eng, P.J. (2010) Hydrated goethite ( $\alpha$ -FeOOH) (100) interface structure: Ordered water and surface functional groups. *Geochimica Et Cosmochimica Acta* 74, 1943-1953.

Hamann, D.R. (1989) Generalized Norm-Conserving Pseudopotentials. *Physical Review B* 40, 2980-2987.

Hamann, D.R., Schluter, M. and Chiang, C. (1979) Norm-Conserving Pseudopotentials. *Physical Review Letters* 43, 1494-1497.

Herbstein, F.H. (2000) How precise are measurements of unit-cell -dimensions from single crystals? *Acta Crystallographica Section B* 56, 547-557.

Hiemstra, T. and Van Riemsdijk, W.H. (1996) A surface structural approach to ion adsorption: the charge distribution (CD) model. *Journal of Colloid and Interface Science* 179, 488-508.



- Hochella, M.F. (1990) Atomic-Structure, Microtopography, Composition, and Reactivity of Mineral Surfaces. *Reviews in Mineralogy* 23, 87-132.
- Hochella, M.F., Lower, S.K., Maurice, P.A., Penn, R.L., Sahai, N., Sparks, D.L. and Twining, B.S. (2008) Nanominerals, mineral nanoparticles, and Earth systems. *Science* 319, 1631-1635.
- Hohenberg, P. and Kohn, W. (1964) Inhomogeneous Electron Gas. *Physical Review B* 136, B864-+.
- Huang, P., Pham, T.A., Galli, G. and Schwegler, E. (2014a) Alumina(0001)/Water Interface: Structural Properties and Infrared Spectra from First-Principles Molecular Dynamics Simulations. *J Phys Chem C* 118, 8944-8951.
- Huang, P., Pham, T.A., Galli, G. and Schwegler, E. (2014b) Alumina(0001)/Water Interface: Structural Properties and Infrared Spectra from First-Principles Molecular Dynamics Simulations. *The Journal of Physical Chemistry C* 118, 8944-8951.
- Huda, M.N., Walsh, A., Yan, Y.F., Wei, S.H. and Al-Jassim, M.M. (2010) Electronic, structural, and magnetic effects of 3d transition metals in hematite. *Journal of Applied Physics* 107.
- Janeček, J., Netz, R.R., Flörsheimer, M., Klenze, R., Schimmelpfennig, B. and Polly, R. (2014) Influence of Hydrogen Bonding on the Structure of the (001) Corundum–Water Interface. Density Functional Theory Calculations and Monte Carlo Simulations. *Langmuir* 30, 2722-2728.
- Jones, F., Rohl, A.L., Farrow, J.B. and van Bronswijk, W. (2000) Molecular modeling of water adsorption on hematite. *Phys Chem Chem Phys* 2, 3209-3216.
- Kappler, A. and Newman, D.K. (2004) Formation of Fe(III)-minerals by Fe(II)-oxidizing photoautotrophic bacteria 1. *Geochimica et Cosmochimica Acta* 68, 1217-1226.
- Kawai, R. and Weare, J.H. (1990) From Vanderwaals to Metallic Bonding - the Growth of Be Clusters. *Physical Review Letters* 65, 80-83.
- Kerisit, S. (2011) Water structure at hematite-water interfaces. *Geochimica Et Cosmochimica Acta* 75, 2043-2061.
- Kerisit, S. and Rosso, K.M. (2006) Computer simulation of electron transfer at hematite surfaces. *Geochimica Et Cosmochimica Acta* 70, 1888-1903.
- Kerisit, S., Weare, J.H. and Felmy, A.R. (2012) Structure and dynamics of forsterite-scCO(2)/H<sub>2</sub>O interfaces as a function of water content. *Geochimica Et Cosmochimica Acta* 84, 137-151.
- Kirfel, A. and Eichhorn, K. (1990) Accurate structure analysis with synchrotron radiation. The electron density in Al<sub>2</sub>O<sub>3</sub> and Cu<sub>2</sub>O. *Acta Crystallographica Section A* 46, 271-284.
- Kohanoff, J. (1994) Phonon spectra from short non-thermally equilibrated molecular dynamics simulations. *Computational Materials Science* 2, 221-232.

Kohn, W. and Sham, L.J. (1965a) Self-Consistent Equations Including Exchange and Correlation Effects. *Phys Rev* 140, A1133-A1138.

Kohn, W. and Sham, L.J. (1965b) Self-Consistent Equations Including Exchange and Correlation Effects. *Physical Review* 140, 1133-&.

Kotliar, G., Savrasov, S.Y., Haule, K., Oudovenko, V.S., Parcollet, O. and Marianetti, C.A. (2006) Electronic structure calculations with dynamical mean-field theory. *Rev Mod Phys* 78, 865.

Kotliar, G. and Vollhardt, D. (2004) Strongly correlated materials: Insights from dynamical mean-field theory. *Physics Today* 57, 53-59.

Kubicki, J., Paul, K. and Sparks, D. (2008a) Periodic density functional theory calculations of bulk and the (010) surface of goethite. *Geochemical Transactions* 9, 4.

Kubicki, J.D., Paul, K.W. and Sparks, D.L. (2008b) Periodic density functional theory calculations of bulk and the (010) surface of goethite. *Geochemical Transactions* 9.

Lad, R.J. and Henrich, V.E. (1989) Photoemission study of the valence-band electronic structure in  $\text{Fe}_x\text{O}$ ,  $\text{Fe}_3\text{O}_4$ , and  $\alpha\text{-Fe}_2\text{O}_3$  single crystals. *Physical Review B* 39, 13478-13485.

Laio, A. and Parrinello, M. (2002) Escaping free-energy minima. *Proceedings of the National Academy of Sciences of the United States of America* 99, 12562-12566.

Lechermann, F., Georges, A., Poteryaev, A., Biermann, S., Posternak, M., Yamasaki, A. and Andersen, O.K. (2006) Dynamical mean-field theory using Wannier functions: A flexible route to electronic structure calculations of strongly correlated materials. *Physical Review B* 74.

Liao, P., Keith, J.A. and Carter, E.A. (2012) Water Oxidation on Pure and Doped Hematite (0001) Surfaces: Prediction of Co and Ni as Effective Dopants for Electrocatalysis. *Journal of the American Chemical Society* 134, 13296-13309.

Liechtenstein, A.I., Anisimov, V.I. and Zaanen, J. (1995) Density-functional theory and strong interactions: Orbital ordering in Mott-Hubbard insulators. *Physical Review B* 52, R5467-R5470.

Liu, P., Kendelewicz, T., Brown Jr, G.E., Nelson, E.J. and Chambers, S.A. (1998) Reaction of water vapor with  $\alpha\text{-Al}_2\text{O}_3(0001)$  and  $\alpha\text{-Fe}_2\text{O}_3(0001)$  surfaces: synchrotron X-ray photoemission studies and thermodynamic calculations. *Surface Science* 417, 53-65.

Lo, C.S., Tanwar, K.S., Chaka, A.M. and Trainor, T.P. (2007) Density functional theory study of clean, hydrated, and defective alumina ( $11\bar{0}2$ ) surfaces. *Physical Review B* 75.

Luo, S.J., Averkiev, B., Yang, K.R., Xu, X.F. and Truhlar, D.G. (2014) Density Functional Theory of Open-Shell Systems. The 3d-Series Transition-Metal Atoms and Their Cations. *Journal of Chemical Theory and Computation* 10, 102-121.

Lyne, P.D., Hodoscek, M. and Karplus, M. (1999) A Hybrid QM-MM Potential Employing Hartree-Fock or Density Functional Methods in the Quantum Region. *The Journal of Physical Chemistry A* 103, 3462-3471.

- Marx, D. and Hutter, J.r. (2012) Ab initio molecular dynamics : basic theory and advanced methods. Cambridge University Press, Cambridge.
- Marzari, N., Mostofi, A.A., Yates, J.R., Souza, I. and Vanderbilt, D. (2012) Maximally localized Wannier functions: Theory and applications. *Reviews of Modern Physics* 84, 1419-1475.
- Maslen, E.N., Streltsov, V.A., Streltsova, N.R. and Ishizawa, N. (1994) Synchrotron X-ray study of the electron density in  $[\alpha]\text{-Fe}_2\text{O}_3$ . *Acta Crystallographica Section B* 50, 435-441.
- Mochizuki, S. (1977) Electrical conductivity of  $\alpha\text{-Fe}_2\text{O}_3$ . *physica status solidi (a)* 41, 591-594.
- Monkhorst, H.J. and Pack, J.D. (1976) Special points for Brillouin-zone integrations. *Physical Review B* 13, 5188-5192.
- Navrotsky, A., Mazeina, L. and Majzlan, J. (2008) Size-driven structural and thermodynamic complexity in iron oxides. *Geochimica Et Cosmochimica Acta* 72, A673-A673.
- Newman, D.K. (2010) Feasting on Minerals. *Science* 327, 793-794.
- Nose, S. (1984) A unified formulation of the constant temperature molecular dynamics methods. *The Journal of Chemical Physics* 81, 511-519.
- Park, C., Fenter, P., Catalano, J.G., Lee, S.S., Nagy, K.L. and Sturchio, N.C. (2010) Aqueous-mineral interfaces toward extreme conditions: The potential experimental approaches with synchrotron X-ray probe. *Geochimica Et Cosmochimica Acta* 74, A794-A794.
- Park, C., Fenter, P.A., Sturchio, N.C. and Regalbuto, J.R. (2005) Probing outer-sphere adsorption of aqueous metal complexes at the oxide-water interface with resonant anomalous X-ray reflectivity. *Physical Review Letters* 94.
- Parr, R.G. and Yang, W.T. (1995) Density-Functional Theory of the Electronic-Structure of Molecules. *Annual Review of Physical Chemistry* 46, 701-728.
- Perdew, J.P., Burke, K. and Ernzerhof, M. (1996) Generalized Gradient Approximation Made Simple. *Physical Review Letters* 77, 3865-3868.
- Perevalov, T.V., Shaposhnikov, A.V., Gritsenko, V.A., Wong, H., Han, J.H. and Kim, C.W. (2007) Electronic structure of  $\alpha\text{-Al}_2\text{O}_3$ : Ab initio simulations and comparison with experiment. *Jetp Lett.* 85, 165-168.
- Pickett, W.E. (1989) Pseudopotential Methods in Condensed Matter Applications. *Computer Physics Reports* 9, 115-197.
- Polly, R., Schimmelpfennig, B., Flörsheimer, M., Kruse, K., AbdelMonem, A., Klenze, R., Rauhut, G. and Fanghänel, T. (2009) Theoretical investigation of the water/corundum (0001) interface. *The Journal of Chemical Physics* 130, 064702.
- Pozun, Z.D. and Henkelman, G. (2011) Hybrid density functional theory band structure engineering in hematite. *Journal of Chemical Physics* 134.

Ranea, V.A., Carmichael, I. and Schneider, W.F. (2009) DFT Investigation of Intermediate Steps in the Hydrolysis of  $\alpha$ -Al<sub>2</sub>O<sub>3</sub>(0001)<sup>†</sup>. *The Journal of Physical Chemistry C* 113, 2149-2158.

Ranea, V.A., Schneider, W.F. and Carmichael, I. (2008) DFT characterization of coverage dependent molecular water adsorption modes on  $\alpha$ -Al<sub>2</sub>O<sub>3</sub>(0001). *Surface Science* 602, 268-275.

Remler, D.K. and Madden, P.A. (1990) Molecular-Dynamics without Effective Potentials Via the Car-Parrinello Approach. *Molecular Physics* 70, 921-966.

Renaud, G. (1998) Oxide surfaces and metal/oxide interfaces studied by grazing incidence X-ray scattering. *Surface Science Reports* 32, 1-+.

Riccardi, D., Schaefer, P., Yang, Yu, H., Ghosh, N., Prat-Resina, X., König, P., Li, G., Xu, D., Guo, H., Elstner, M. and Cui, Q. (2006) Development of Effective Quantum Mechanical/Molecular Mechanical (QM/MM) Methods for Complex Biological Processes. *The Journal of Physical Chemistry B* 110, 6458-6469.

Richmond, G.L. (2002) Molecular Bonding and Interactions at Aqueous Surfaces as Probed by Vibrational Sum Frequency Spectroscopy. *Chemical Reviews* 102, 2693-2724.

Rochester, C. and Topham, S. (1979) Infrared Study of Surface Hydroxyl-Groups on Goethite. *Journal of the Chemical Society - Faraday Transactions I* 75, 591 - 602.

Roden, E.E. (2006) Geochemical and microbiological controls on dissimilatory iron reduction. *Comptes Rendus Geoscience* 338, 456-467.

Rohrbach, A., Hafner, J. and Kresse, G. (2004) Ab initio study of the (0001) surfaces of hematite and chromia: Influence of strong electronic correlations. *Physical Review B* 70, 125426.

Rollmann, G., Rohrbach, A., Entel, P. and Hafner, J. (2004) First-principles calculation of the structure and magnetic phases of hematite. *Physical Review B* 69, 165107.

Roques, J., Veilly, E. and Simoni, E. (2009) Periodic Density Functional Theory Investigation of the Uranyl Ion Sorption on Three Mineral Surfaces: A Comparative Study. *International Journal of Molecular Sciences* 10, 2633-2661.

Rosso, K.M. and Rustad, J.R. (2001) Structures and energies of AlOOH and FeOOH polymorphs from plane wave pseudopotential calculations. *American Mineralogist* 86, 312-317.

Rustad, J.R., Felmy, A.R. and Bylaska, E.J. (2003) Molecular simulation of the magnetite-water interface. *Geochimica Et Cosmochimica Acta* 67, 1001-1016.

Rustad, J.R., Felmy, A.R. and Hay, B.P. (1996) Molecular statics calculations for iron oxide and oxyhydroxide minerals: Toward a flexible model of the reactive mineral-water interface. *Geochimica Et Cosmochimica Acta* 60, 1553-1562.

Senn, H. and Thiel, W. (2007) QM/MM Methods for Biological Systems, in: Reiher, M. (Ed.), *Atomistic Approaches in Modern Biology*. Springer Berlin Heidelberg, pp. 173-290.

Shen, Y.R. (1989) Surface properties probed by second-harmonic and sum-frequency generation. *Nature* 337, 519-525.

Shen, Y.R. and Ostroverkhov, V. (2006) Sum-Frequency Vibrational Spectroscopy on Water Interfaces: Polar Orientation of Water Molecules at Interfaces. *Chemical Reviews* 106, 1140-1154.

Shick, A.B., Liechtenstein, A.I. and Pickett, W.E. (1999) Implementation of the LDA+U method using the full-potential linearized augmented plane-wave basis. *Physical Review B* 60, 10763-10769.

Shroll, R.M. and Straatsma, T.P. (2003) Molecular Dynamics Simulations of the Goethite-water Interface. *Mol Simulat* 29, 1-11.

Stumm, W. and Sulzberger, B. (1992) The cycling of iron in natural environments: Considerations based on laboratory studies of heterogeneous redox processes. *Geochimica Et Cosmochimica Acta* 56, 3233-3257.

Sun, J.Z., Stirner, T. and Matthews, A. (2007) Molecular dynamics simulation of the (0001) $\alpha$ -Al<sub>2</sub>O<sub>3</sub> and  $\alpha$ -Cr<sub>2</sub>O<sub>3</sub> surfaces. *Surface Science* 601, 1358-1364.

Sung, J., Shen, Y.R. and Waychunas, G.A. (2012) The interfacial structure of water/protonated  $\alpha$ -Al<sub>2</sub>O<sub>3</sub> (11 $\bar{2}$ 0) as a function of pH. *Journal of Physics: Condensed Matter* 24, 124101.

Sung, J., Zhang, L., Tian, C., Shen, Y.R. and Waychunas, G.A. (2011) Effect of pH on the Water/ $\alpha$ -Al<sub>2</sub>O<sub>3</sub> (1 $\bar{1}$ 02) Interface Structure Studied by Sum-Frequency Vibrational Spectroscopy. *The Journal of Physical Chemistry C* 115, 13887-13893.

Szabo, A. and Ostlund, N.S. (1996) Modern quantum chemistry : introduction to advanced electronic structure theory. Dover Publications, Mineola, N.Y.

Tanwar, K.S., Lo, C.S., Eng, P.J., Catalano, J.G., Walko, D.A., Brown, G.E., Waychunas, G.A., Chaka, A.M. and Trainor, T.P. (2007a) Surface diffraction study of the hydrated hematite (1 $\bar{1}$ 02) surface. *Surface Science* 601, 460-474.

Tanwar, K.S., Petitto, S.C., Ghose, S.K., Eng, P.J. and Trainor, T.P. (2008) Structural study of Fe(II) adsorption on hematite. *Geochimica Et Cosmochimica Acta* 72, 3311-3325.

Tanwar, K.S., Petitto, S.C., Ghose, S.K., Eng, P.J. and Trainor, T.P. (2009) Fe(II) adsorption on hematite (0 0 0 1). *Geochimica Et Cosmochimica Acta* 73, 4346-4365.

Teter, M. (1993) Additional condition for transferability in pseudopotentials. *Physical Review B* 48, 5031-5041.

Tews, W. and Gründler, R. (1982) Electron-Energy-Loss Spectroscopy of Different Al<sub>2</sub>O<sub>3</sub> Modifications. I. Energy Loss Function, Dielectric Function, Oscillator Strength Sum Rule and the Quantity  $\epsilon_2 E$ . *physica status solidi (b)* 109, 255-264.

Thissen, P., Grundmeier, G., Wippermann, S. and Schmidt, W.G. (2009) Water adsorption on the  $\alpha$ -Al<sub>2</sub>O<sub>3</sub>(0001) surface. *Physical Review B* 80, 245403.

Thomas, M., Brehm, M., Fligg, R., Vöhringer, P. and Kirchner, B. (2013) Computing vibrational spectra from ab initio molecular dynamics. *Physical Chemistry Chemical Physics* 15, 6608-6622.

Trainor, T.P., Chaka, A.M., Eng, P.J., Newville, M., Waychunas, G.A., Catalano, J.G. and Brown Jr, G.E. (2004) Structure and reactivity of the hydrated hematite (0001) surface. *Surface Science* 573, 204-224.

Tunega, D. (2012) Theoretical Study of Properties of Goethite ( $\alpha$ -FeOOH) at Ambient and High-Pressure Conditions. *The Journal of Physical Chemistry C* 116, 6703-6713.

Valdes, A., Brillet, J., Gratzel, M., Gudmundsdottir, H., Hansen, H.A., Jonsson, H., Klupfel, P.,

Kroes, G.J., Le Formal, F., Man, I.C., Martins, R.S., Norskov, J.K., Rossmeisl, J., Sivula, K., Vojvodic, A. and Zach, M. (2012) Solar hydrogen production with semiconductor metal oxides: new directions in experiment and theory. *Physical Chemistry Chemical Physics* 14, 49-70.

Valiev, M., Bylaska, E.J., Govind, N., Kowalski, K., Straatsma, T.P., Van Dam, H.J., Wang, D., Nieplocha, J., Apra, E. and Windus, T.L. (2010) NWChem: a comprehensive and scalable open-source solution for large scale molecular simulations. *Computer Physics Communications* 181, 1477-1489.

van der Zee, C., Roberts, D.R., Rancourt, D.G. and Slomp, C.P. (2003) Nanogoethite is the dominant reactive oxyhydroxide phase in lake and marine sediments. *Geology* 31, 993-996.

Wang, H.W., DelloStritto, M.J., Kumar, N., Kolesnikov, A.I., Kent, P.R.C., Kubicki, J.D., Wesolowski, D.J. and Sofo, J.O. (2014) Vibrational Density of States of Strongly H-Bonded Interfacial Water: Insights from Inelastic Neutron Scattering and Theory. *J Phys Chem C* 118, 10805-10813.

Wang, L., Maxisch, T. and Ceder, G. (2006) Oxidation energies of transition metal oxides within the GGA+U framework. *Physical Review B* 73, 195107.

Weber, K.A., Achenbach, L.A. and Coates, J.D. (2006) Microorganisms pumping iron: anaerobic microbial iron oxidation and reduction. *Nat Rev Micro* 4, 752-764.

Wittbrodt, J.M., Hase, W.L. and Schlegel, H.B. (1998) Ab Initio Study of the Interaction of Water with Cluster Models of the Aluminum Terminated (0001)  $\alpha$ -Aluminum Oxide Surface. *The Journal of Physical Chemistry B* 102, 6539-6548.

Yanina, S.V. and Rosso, K.M. (2008) Linked reactivity at mineral-water interfaces through bulk crystal conduction. *Science* 320, 218-222.

Yin, S. and Ellis, D.E. (2008) H<sub>2</sub>O adsorption and dissociation on defective hematite (0001) surfaces: A DFT study. *Surface Science* 602, 2047-2054.

Yin, S. and Ellis, D.E. (2009) DFT studies of Cr(VI) complex adsorption on hydroxylated hematite (012) surfaces. *Surface Science* 603, 736-746.

Yin, S., Ma, X. and Ellis, D.E. (2007) Initial stages of H<sub>2</sub>O adsorption and hydroxylation of Fe-terminated  $\alpha$ -Fe<sub>2</sub>O<sub>3</sub>(0001) surface. *Surface Science* 601, 2426-2437.

Ying Chen, E.J.b., John H Weare (2015) 1St Principle Estimation of Geochemically Important Transition Metal Oxide Properties: Structure and Dynamics of the Bulk, Surface and Mineral/Aqueous Fluid Interface (to be submitted).

Yong, H. and Van Riemsdijk, W.H. (1999) Interfacial Charging Phenomena of Aluminum (Hydr)oxides. *Langmuir* 15, 5942-5955.

Zgid, D. and Chan, G.K.L. (2011) Dynamical mean-field theory from a quantum chemical perspective. *J Chem Phys* 134.

Zhang, C., Donadio, D., Gygi, F. and Galli, G. (2011) First Principles Simulations of the Infrared Spectrum of Liquid Water Using Hybrid Density Functionals. *Journal of Chemical Theory and Computation* 7, 1443-1449.

Zhang, L., Tian, C., Waychunas, G.A. and Shen, Y.R. (2008) Structures and Charging of  $\alpha$ -Alumina (0001)/Water Interfaces Studied by Sum-Frequency Vibrational Spectroscopy. *Journal of the American Chemical Society* 130, 7686-7694.

Zhao, Y. and Truhlar, D.G. (2008) Density functionals with broad applicability in chemistry. *Accounts of Chemical Research* 41, 157-167.

Zhou, F., Cococcioni, M., Marianetti, C.A., Morgan, D. and Ceder, G. (2004) First-principles prediction of redox potentials in transition-metal compounds with LDA+U. *Physical Review B* 70, 235121.

Ziman, J.M. (1972) *Principles of the theory of solids*, 2d ed. University Press, Cambridge Eng.